Internal lee waves in the abyssal ocean : diapycnal mixing and interactions with inertial oscillations.

Pierre Labreuche

▶ **To cite this version:**

Pierre Labreuche. Internal lee waves in the abyssal ocean : diapycnal mixing and interactions with inertial oscillations.. Earth Sciences. Université Grenoble Alpes, 2015. English. NNT : 2015GREAU035 . tel-01684248

HAL Id: tel-01684248
https://theses.hal.science/tel-01684248

Submitted on 15 Jan 2018

HAL is a multi-disciplinary open access archive for the deposit and dissemination of scientific research documents, whether they are published or not. The documents may come from teaching and research institutions in France or abroad, or from public or private research centers.

L'archive ouverte pluridisciplinaire **HAL**, est destinée au dépôt et à la diffusion de documents scientifiques de niveau recherche, publiés ou non, émanant des établissements d'enseignement et de recherche français ou étrangers, des laboratoires publics ou privés.

UNIVERSITÉ DE GRENOBLE

THÈSE

Pour obtenir le grade de

DOCTEUR DE L'UNIVERSITÉ DE GRENOBLE

Spécialité : **Océanographie**

Arrêté ministériel : 7 août 2006

Présentée par

Pierre Labreuche

Thèse codirigée par **Chantal Staquet** et **Julien Le Sommer**

préparée au sein des **Laboratoire d'Écoulements Géophysiques et Industriels** et **Laboratoire de Glaciologie et Géophysique de l'Environnement**

Ondes de relief dans l'océan profond: mélange diapycnal et interactions avec les oscillations inertielles.

Thèse soutenue publiquement le **Fin Mars-Début Avril 2015**,
devant le jury composé de :

Achim Wirth
LEGI Grenoble, Président

François Lott
LMD Paris, Examinateur

Gurvan Madec
LOCEAN Paris, Examinateur

George Nurser
NOC Southampton, Rapporteur

Riwal Plougonven
LMD Paris, Rapporteur

Julien Le Sommer
LGGE Grenoble, Co-Directeur de thèse

Chantal Staquet
LEGI Grenoble, Co-Directeur de thèse

Thanks

Merci

'Twas brillig, and the slithy toves
Did gyre and gimble in the wabe:
All mimsy were the borogoves,
And the mome raths outgrabe.

"Beware the Jabberwock, my son!
The jaws that bite, the claws that catch!
Beware the Jubjub bird, and shun
The frumious Bandersnatch!"

He took his vorpal sword in hand:
Long time the manxome foe he sought –
So rested he by the Tumtum tree,
And stood awhile in thought.

And, as in uffish thought he stood,
The Jabberwock, with eyes of flame,
Came whiffling through the tulgey wood,
And burbled as it came!

One, two! One, two! And through and through
The vorpal blade went snicker-snack!
He left it dead, and with its head
He went galumphing back.

"And, has thou slain the Jabberwock?
Come to my arms, my beamish boy!
O frabjous day! Callooh! Callay!'
He chortled in his joy.

'Twas brillig, and the slithy toves
Did gyre and gimble in the wabe;
All mimsy were the borogoves,
And the mome raths outgrabe.

*Jabberwocky by **Lewis Carroll**,*
Through the Looking-Glass and What Alice Found There, 1872

Table 1 – *List of the acronyms later used in the manuscript*

Acronym	*Definition*
AABW	AntArctic Bottom Water
ACC	Antarctic Circumpolar Current
CFL	Courant–Friedrichs–Lewy
E-P	Eliassen-Palm
IDW	Indian Deep Water
ILW	Internal Lee Wave
IO	Inertial oscillation
NADW	North Atlantic Deep Water
PDW	Pacific Deep Water
QG	Quasi-Geostrophic
RBE	Radiation Balance Equations
RIT	Resonant Interaction Theory
SOFine	Southern Ocean FINEstructure
TEM	Transformed Eulerian Mean
TKE	Turbulent Kinetic Energy
VMP	Vertical Microstructure Profiler
WOCE	World Ocean Circulation Experiment

Contents

Introduction 3

1 Diapycnal mixing in the ocean: from ocean sampling to ocean modelling 17

1.1 From Turbulent Kinetic Energy dissipation rates to diapycnal mixing: energy conservation . . . 17

1.2 Micro-structure: a local measure . . . 18

1.3 The fine-scale parameterization: inferring mixing from shear and stress . . . 19

1.4 Ocean recipes: from topography and stratification to mixing estimates . . . 22

1.4.1 Getting the bottom energy conversion . . . 23

1.4.2 The nonlinear propagation model . . . 24

1.4.3 Caveats . . . 25

1.5 Towards global estimates . . . 26

1.5.1 Getting a global coverage of TKE dissipation . . . 26

1.6 Summary of the diapycnal mixing parameterizations . . . 28

2 A first look at the phenomenology: numerical simulations 33

2.1 Introduction of the numerical case study . . . 33

2.1.1 Physical configuration . . . 33

2.1.2 Numerical set-up . . . 34

2.1.3 Off the hat behavior . . . 37

2.2 Description of the Turbulent Kinetic Energy dissipation rate . . . 40

2.3 Description of inertial oscillations 43
2.4 On the link between IO amplitude and TKE dissipation rate 44

3 Attempting to predict inertial oscillation amplitude: an approach following Nikurashin and Ferrari 2010 55
3.1 The asymptotic theory 55
3.1.1 Assumptions of the theory 55
3.1.2 Keeping the vertical coordinate 56
3.2 Comparison with the simulations 61
3.2.1 Growth rate of the inertial oscillations 61
3.2.2 Vertical extent of the inertial oscillations 63

4 Attempting to predict inertial oscillation amplitude: on the importance of resonant triad interactions 73
4.1 The resonant interaction theory 73
4.1.1 Pros and cons of the underlying hypotheses 73
4.1.2 Derivation 74
4.2 Analyzing the numerical experiments in light of the resonant interaction theory 78
4.2.1 Applying the RIT to the interaction involving inertial oscillations and internal lee waves 79
4.2.2 Comparison with the simulations 81
4.3 The computation of $\partial_z \overline{u'w'}$ in the RIT 84

5 Towards a three dimensional description 93
5.1 Possible implications of three-dimensional dynamics 93
5.1.1 Specificities of two and three-dimensional studies 93
5.1.2 Implications of momentum deposition on large scale circulation 95
5.2 Design of the numerical experiment 97
5.2.1 A new numerical code 97

5.2.2 Defining the experimental setup . . . 101
5.2.3 Practical implementation . . . 104
5.3 Analysis of the simulations . . . 105
5.3.1 Overview of the analysis . . . 105
5.3.2 Energy reservoirs and fluxes . . . 106
5.3.3 The Transformed-Eulerian Mean (TEM) framework . . . 107
5.3.4 Preliminary results . . . 108
5.4 Conclusion . . . 111

Conclusions and perspectives **117**

A Annexes **125**
A.1 Resonant interaction theory . . . 127
A.1.1 Deriving the resonant interaction theory . . . 127
A.1.2 Calculation of the growth rate . . . 131
A.2 Asymptotic theory, from Nikurashin and Ferrari (2010) and more . 133
A.2.1 Summary of Nikurashin and Ferrari (2010) . . . 133
A.2.2 Moving on from Nikurashin and Ferrari (2010) . . . 136
A.2.3 Vertical structure and propagation of inertial oscillations . . 137

Bibliography **138**
A.3 Submitted paper . . . 146

List of Tables

1 List of the acronyms later used in the manuscript 5

2.1 Summary of the different two-dimensional simulations. The simulations vary by the height or the wavelength of the topography, by the bottom boundary condition or by the value of the Coriolis frequency. 35

4.1 Wave characteristics of the triad involving the wave $*$ of frequency $U_G k_T - |f|$ 80

4.2 Wave characteristics of the triad involving the wave $*$ of frequency $U_G k_T + |f|$ 80

List of Figures

1 The Pacific Indian conveyor belt as viewed in early studies, adapted from Talley et al. (2011). 5

2 The two cell circulation as viewed in the early 2000's, adapted from Talley et al. (2011). 8

3 The three basin circulation as viewed in the early 2010s, adapted from Talley et al. (2011). 10

2.1 Physical setting used in the numerical simulations. The forcing consists in a uniform, constant flow U_G. The two-dimensional topography is sinusoidal, of wavenumber k_T, and peak to peak distance 2 h_T. Internal lee waves are thus generated and radiate away from the bottom. Their phase is sketched by the dotted lines. 34

2.2 Snapshots of the vertical velocity for experiment $H_{40}L_2$: (top) after one inertial period; (bottom) after 7 inertial periods. The same colorbar is used for the two panels, but the maximum value is about three times higher in (b) than in (a). The top frame shows a quasi-linear regime, where internal lee waves can clearly be seen to radiate from the topography upwards. The bottom frame shows a strongly non-linear regime, with turbulent behavior near the bottom. 46

2.3 Temporal evolution of the turbulent kinetic energy dissipation rate for all simulations, in inertial periods. The TKE dissipation is integrated over the bottom 2000 m. 47

2.4 Vertical structure of the turbulent kinetic energy dissipation rate for the L_2_fs simulations. TKE dissipation is computed by interpolating the $\sigma-$coordinate field to $z-$coordinates and then averaged from 12 to 15 inertial periods. Note the logarithmic scale on the x-axis. 47
2.5 Vertical structure of the turbulent kinetic energy dissipation rate. For all the simulations, the TKE dissipation rate is averaged from 12 to 15 inertial periods. 48
2.6 $\int_z^H \mathcal{E}\partial z$ normalized by the energy radiated at topography for all simulations in [m]. This represents the proportion of the energy converted from the mean flow to the internal wave field that is dissipated under a given height. 48
2.7 $\int_z^H \mathcal{E}\partial z$ normalized by $\int_0^{2000} \mathcal{E}\partial z$ for all simulations in [m]. This represents the proportion of the total TKE dissipation rate that is dissipated under a given height. 49
2.8 Variance preserving power spectrum of w for experiment $H_{20}L_2$, near 600 m above the topography, computed in a frame moving with the geostrophic velocity U_G. When the curve has a larger value than the dashed line, it departs significantly from red noise at 99% level. The inertial and Brunt Väisälä frequency are indicated with a dashed-dotted line. 49
2.9 Vertical structure of the amplitude of inertial oscillations for the L_2_fs simulations. Note the logarithmic scale on the x-axis. 50
2.10 Scatter plot of the IO kinetic energy versus the TKE dissipation integrated over the domain. TKE dissipation is scaled by the bottom conversion rate. IO kinetic energy is normalized by the bottom conversion rate divided by an inertial period. Cases with little IO growth are shown with empty markers, the other with grey or black markers. 51

3.1 Time-height diagram of the horizontal velocity of the inertial oscillations (colors) and of the momentum deposit of the internal lee wave (contours) for experiment $H_{20}L_{20\_}fs$. The contours are hatched when $-\partial_z\overline{u'w'} > 0$. 59
3.2 Temporal evolution of the amplitude of inertial oscillations at 100 m, in inertial periods. The IO signal was processed through a Lanczos low-pass filter at cutoff frequency f. The spin up of the simulation, during which the mean flow grows from 0 to U_G and IO are explicitly damped, is not shown. 62
3.3 Time evolution of the IOs, as in figure 3.2, except that time is normalized by the growth rate from the asymptotic theory. 63
3.4 Comparison of the IO growth rate between that diagnosed from the simulations and that predicted by the asymptotic theory. . . . 66
3.5 Vertical structure of the inertial oscillation amplitude. For all the simulations, the IOs are averaged from 12 to 15 inertial periods. . 67
3.6 Analytical and simulated profiles for the TKE dissipation rate (a) and IO amplitude (b). Example of the analytical (in dotted line) to simulated (in full line) profile comparison for simulation $H_{40}L_{20\_}fs$. The simulation profile is averaged from 12 to 15 inertial periods. 68
3.7 Comparison of the IO vertical extent between that diagnosed from the simulations and that predicted by the asymptotic theory using Eq. 3.11 69
3.8 Scatter-plot of the diagnosed *effective height* for the IO amplitude and TKE dissipation rate, diagnosed from the simulations. 70

4.1 Variance preserving power spectrum of w for experiment $H_{20}L_2$, near 600 m above the topography, computed in a frame moving with the geostrophic velocity U_G. When the curve is larger than the dashed line, it departs significantly from red noise at 99% level. The inertial and buoyancy frequencies are indicated in dashed-dotted line, as well as the frequencies predicted by the resonant interaction theory. 81
4.2 Time evolution of the IOs, as in figure 3.2, except that time is scaled by the growth rate from the resonant interaction theory. . . 82
4.3 Scatter-plot of the growth rate diagnosed from the simulations and that predicted by the RIT. 88
4.4 Time-height diagram of the horizontal velocity of the inertial oscillations for $H_{20}L_{2\_}fs$. The slope of the red line has the value of the vertical phase speed of the IOs f/m_{IO} with m_{IO} derived from the resonant interaction theory. Only the triad corresponding to a third wave of frequency $U_G k_t - |f|$ and negative vertical wavenumber is shown. 89

5.1 Comparison of the time-height diagrams of the IO field above the topography for setting $H_{40}L_{2\_}fs$ in NHOES (top) and SNH (bottom).The NHOES simulation has a resolution twice rougher than the SNH simulation The black lines correspond to a signal moving at the vertical phase speed of the IOs as predicted by the RIT. . . . 100
5.2 Topographic profile corresponding to Eq. 5.4 103
5.3 State of the flow at the end of the simulation (after 11 inertial periods) Top: vectors of **u**, the mean current flows to the right. Bottom: iso-contours of **u**, the mean current flows away from the reader into the paper. 112

5.4 Iso-levels of the zonally averaged density along the zonal (left) and meridional (right) directions. Dashed lines are the positions of the isopycnals at the beginning of the simulation. Full lines represent the isopycnal positions at the end of the computation. . 113

5.5 Time evolution of $\overline{\mathbf{u}}^x$ along a line 100 m above the top of the topography. Top frame encapsulates the meridional variation of $\overline{u}^x$, whereas the bottom frame represent the two horizontal components of $\overline{\mathbf{u}}^x$ computed along a line situated in the center of the domain in the meridional (y) direction. These fields should encapsulate the mean flow and inertial oscillations. 114

Introduction

Why study the ocean?

Systematic environmental monitoring has become widespread over the last decades, both for short term risk and weather forecasts and for long term climate monitoring. On daily time scales and as a first approximation, the ocean can be considered as a thermostat, a reservoir of heat and humidity, undergoing small or no changes. On the other hand, larger time scales have raised great interest, be it for understanding the history or the projections of the Earth climate, on time scales of hundreds of years or more (IPCC 2014). Evolution on such time scales is called climate, as opposition to the small time scale weather.

On climatic time scales, the role of the oceans is key. Their high heat capacity and the meridional transport of waters (the overturning circulation) make them reservoirs of heat and fundamental actors in redistributing heat from the equator to the poles. Through air-sea exchanges, the ocean are also key in studying transport and evolution of water, gases and mater. For instance, recent studies suggest that if the surface temperature is currently at a standstill although the anthropogenic CO_2 emissions have continued to rise, it might be due to the oceans absorbing more heat than previously (Chen and Tung 2014). Other concerns relate, for instance, to the acidification of the oceans due to carbon uptake.

Thus understanding the ocean behavior and the overturning circulation is an essential step to building correct representations and models of the global climate. Most studies focus on the ocean surface and its interaction with the atmosphere, as well as the downwelling of the water masses, building knowledge about the balance between intake and uptake of heat and matter by the ocean.

The return of the water masses to the surface is an equally important topic, and is the focus of many a study.

The overturning circulation

The global ocean is made of four major basins: the Atlantic ocean, the Indian ocean, the Pacific ocean and the Antarctic ocean. These four interconnected basins have complex interplays, and to study the transport of heat from the equatorial surface to the poles and the ocean interior oceanographers attempt to describe the large scale features of the ocean currents, the overturning circulation.

The meridional circulation and uniform mixing

In the last century, the North Atlantic was thought to be the main driver of the ocean circulation. North Atlantic Deep Water (NADW) would form through the interaction with the atmosphere at high latitudes. The NADW, pushed by this downwelling, would then coat the stably stratified ocean (the lightest waters sitting on top of the densest waters). Finally uniform mixing would blend together the dense, bottom waters with lighter waters lying on top, leading to a gradual upwelling of the water masses and their return to the warm, surface open ocean waters. This dynamic is quasi-two dimensional, which lead to considering the overturning circulation in the North-South axis under the name of meridional circulation.

Figure 1 is a schematic of this representation.

Munk (1966) expressed the above description by stating that a uniform mixing over the ocean would be balanced by uniform upwelling through the following advection/diffusion relation:

$$w\frac{\partial \rho}{\partial z} = K_v \frac{\partial^2 \rho}{\partial z^2} \tag{1}$$

where ρ is density, K_v is the uniform mixing and the vertical coordinate z has its origin at the bottom and increases upwards. Munk (1966) calculated that to

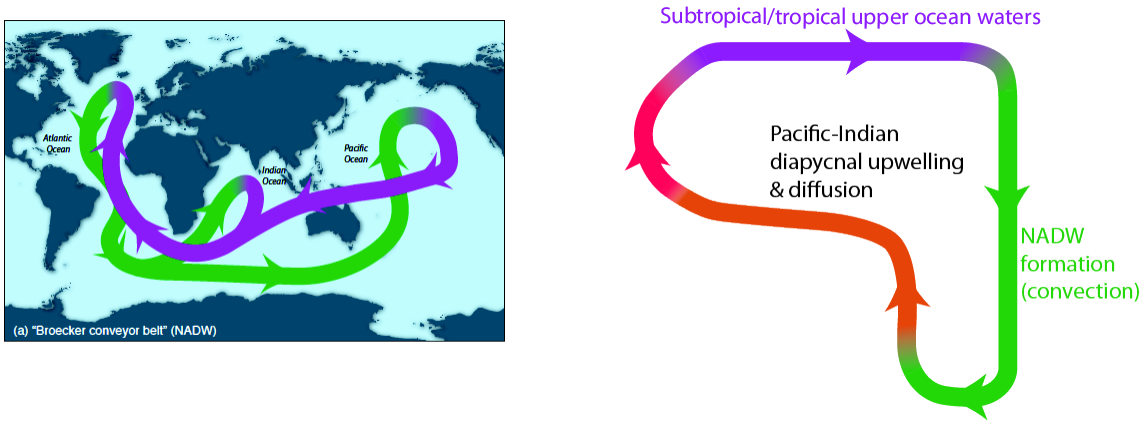

Figure 1 – *The Pacific Indian conveyor belt as viewed in early studies, adapted from Talley et al. (2011).*

sustain the thermohaline circulation, a uniform mixing across surfaces of the same density (isopycnals) of roughly 10^{-4} $m^2.s^{-1}$ was required. Note that we here refer to mixing in the interior of the ocean and omit surface mixing. Most mixing in the ocean occurs in the upper layer in contact with the atmosphere and cryosphere, but it refers to completely different mechanisms and will not further be discussed in this manuscript.

From energy sources to mixing estimates

To corroborate or disprove this estimate, field measurements were needed for comparison. Since widely measuring cross-density (or diapycnal) mixing with in-situ instruments was unfeasible, a proxy was needed. Thus, Osborn (1980) related the amount of diapycnal mixing to the rate of turbulent kinetic energy dissipation through:

$$K_v N^2 = \frac{R_f}{1 - R_f} \mathcal{E} \tag{2}$$

where R_f is the mixing efficiency, commonly taken at $1/6$ (details of this calculation can be found in the first chapter of this manuscript).

Turbulent kinetic energy comes from various sources, and is related to motions of scale of one kilometer or less. These motions, once generated, can have an eventful life, may undergo propagation, and finally dissipate. Directly esti-

mating the global dissipation rates of energy is extremely tricky, but the processes by which energy is injected at these scales are better known.

At these scales, the most important sources of turbulent kinetic energy lie in the internal wave field. Internal waves are oscillatory motions due to the restoring forces created by the planetary rotation and the local stratification of the fluid. They coat the entire ocean, propagate, interact together, with other classes of motion and with the interfaces, and eventually dissipate. Although investigating the final dissipation of the wave field is quite tricky and still the object of many speculations, the mechanisms and locations of the wave emission is now relatively well known (Ferrari and Wunsch 2009). At the bottom of the ocean, the sources of internal waves principally rely on the interaction of sub-inertial fluid motions with topography, and can be divided into two main candidates:

- **The internal tide:** the tide, generated by the gravitational attraction of the moon and the sun, is a horizontal oscillatory motion of relatively slow time scale (about 12 hours). When this vertically homogeneous motion flows above a mountainous area, internal waves of the same frequency as the tide are emitted, also called the internal tide, that amount to about 1 TW of converted power (Ferrari and Wunsch 2009).
- **The internal lee waves:** when a deep reaching, constant current flows over a mountain range, the water displacement can also emit internal waves, that are stationary with respect to the topography. The power available in the internal lee wave field is about 0.2 TW (Nikurashin and Ferrari 2011).

A question remains about the fate of the energy in geostrophic eddies, that has to be dissipated somewhere in the ocean.

Levels of mixing thus estimated and observed are extremely patchy and of greatly varying amplitude (mostly 10^{-6} $m^2.s^{-1}$, with peaks at 10^{-3} $m^2.s^{-1}$) (Polzin et al. 1997). What was even more unsettling was that the integrated diapycnal mixing estimate was much smaller than that predicted by Munk (1966). This lead to the search of what was called the *missing mixing*.

Is there a really missing mixing? The evolution of the representation of the meridional circulation

However, these concepts fell at the turn of the century, and the development of a large scale mapping of the ocean state: the World Ocean Circulation Experiment (WOCE). This global ocean survey revealed that about 60% of the NADW upwells in the Southern ocean in the Antarctic Circumpolar Current (ACC). Moreover, this upwelling is mainly be due to the strong divergent winds at the surface, roughly around 60°S (the Antarctic divergence). After upwelling, the waters would experience important transformations through intense exchange with the atmosphere, then take one of two branches. They would either flow back North, into the Indian, Pacific or Atlantic ocean, before once again undergoing downwelling and finally upwell North of the Antarctic divergence, in a cycle often called the great ocean conveyor belt. The other path goes South of the Antarctic divergence towards the Antarctic continent, where extremely dense waters would form, downwell at the Antarctic margin and coat the very bottom of the ocean. These very dense, deep waters called the Antarctic bottom waters (AABW) would then upwell through both Ekman pumping and local mixing, and emerge South of the Antarctic divergence. This representation revealed that the upper cell upwelling is adiabatic, the lightening of the NADW being accomplished by surface fluxes, whereas only the lower cell requires interior mixing to be sustained. Figure 2 explains the ocean circulation as represented in these days.

This change in understanding the leading upwelling mechanism lowered the amount of mixing required to consume dense water masses formed at high latitudes to levels observed in field studies (Webb and Suginohara 2001). The levels of mixing observed did not evolve much, but the amount of mixing needed over the ocean was substantially lowered: the *missing mixing* paradox was solved (Munk and Wunsch 1998). However, to further deepen our climate representation and models taking the interconnected basins into account is essential. We

Figure 2 – *The two cell circulation as viewed in the early 2000's, adapted from Talley et al. (2011).*

therefore need to further understand and represent the details in the horizontal and vertical distribution of the diapycnal mixing.

A three dimensional description

In the last few years it has become apparent that the three dimensional structure of the ocean circulation was key to understanding the mechanisms at play. As depicted above, the Southern Ocean keeps a fundamental role in the upwelling of interior waters, as well as the link between the three other major oceans. However, the two independent overturning cells are now obsolete, as it has become clear that waters from the fours basins are deeply interwoven. Let us follow the story of a fictional fluid parcel originating in the North Atlantic. Although this representation is inexact in many ways, it provides a scenario somewhat easier to understand.

At first, through air-sea exchanges and cooling, the parcel densifies and downwells with the NADW. It travels along this dense layer all the way to the Southern Ocean and adiabatically upwells in relatively dense waters in the same way as depicted above. Through surface exchanges with the atmosphere and the cryosphere the parcel becomes denser again and downwells along the continental shelf. As it flows down, mixing with ambient waters and non-linearities in the equation of state [1] increase density yet again (this phenomenon is called cabelling). The extremely dense parcel is part of the AABW, flows around the Antarctic continent and eventually northwards. As it circulates, through the Pacific Ocean for instance, it undergoes diapycnal mixing with overlying waters and becomes slightly lighter. The parcel then comes back south, in the form of Circumpolar Deep Waters (CDW), a water mass lighter than the AABW. It later flows back north, in the Indian Ocean for instance, and undergoes some more mixing and becomes lighter, for example when it flows through the Indonesian Throughflow, a shallow, narrow area with very intense mixing. This roundabout through the Antarctic, Pacific and Indian oceans can occur a few times before the parcel becomes light enough to upwell near the surface, and be further lightened by near-surface processes. The parcel is then exported through the PDW and Indian Deep Waters (IDW), in relatively light waters. Finally the NADW, the PDW and the IDW join together to form the subtropical and tropical upper ocean waters, and after crossing the warm water sphere the water parcel returns to the North Atlantic.

Figure 3 is a sketch of this later representation.

Of the two cells described above, the water mass transformations occurring in the upper diabatic cell are fairly well understood, whereas constraining the progressive lightening of the dense AABW waters through successive cycles still proves a challenge. One of the current major open questions regarding our understanding of the global ocean circulation concerns AABW consumption

1. The equation of state is the relation between density, salinity, potential temperature and pressure

(Lavergne et al. submitted), and thus the amplitude, horizontal distribution and vertical structure of diapycnal mixing and diffusion at these depths. Lavergne et al. (submitted) express the above description by stating that the transformation rate T of the AABW of a given density ρ is related to the cross-isopycnal (i.e. diapycnal) mixing K_v through:

$$T(\rho) = \int\int \frac{g}{N^2}\frac{d}{dz}\left(K_v\frac{\partial\rho}{\partial z}\right)dS \tag{3}$$

where S is the surface of the isopycnal considered, g is the gravity acceleration, N the Brunt Vaisala frequency, ρ is density [2] as a function of space and the vertical coordinate z has its origin at the bottom and increases upwards. For more clarity we omitted here the geothermal heating, that operate on the bottom-most layer of the AABW. Lavergne et al. (submitted) found that depending on the details of the horizontal distribution and vertical structure of K_v the amount of AABW consumption could vary of up to an order of magnitude.

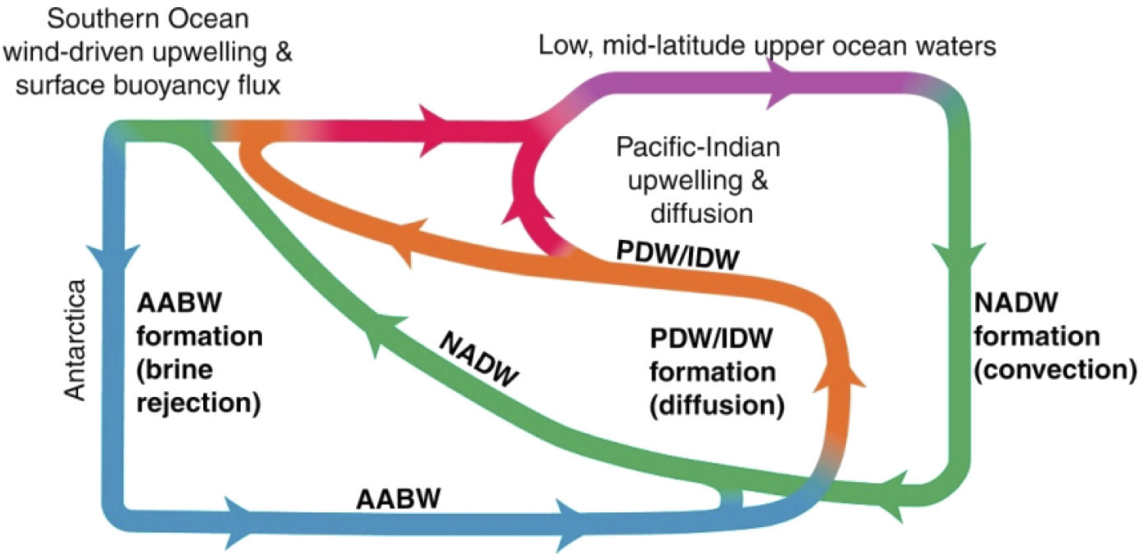

Figure 3 – *The three basin circulation as viewed in the early 2010s, adapted from Talley et al. (2011).*

2. For clarity, we confuse density with the neutral density

Role of internal lee waves

As we have seen in the previous section, the horizontal distribution and vertical structure of the diapycnal mixing, and through Eq. 1.3b turbulent kinetic energy dissipation rate, is more important than their integrated value. Indeed, mixing processes are key in the transformation of the AABW. The two main sources of mixing occur through the interaction of different ingredients, and occur in different places. Through the interaction of the barotropic tide and bottom topography, internal tides are mostly generated along the great ridges North of 50-60°S. Internal lee waves, on the other hand, require deep reaching jets above rough topography, which are mostly found along the Antarctic Circumpolar Current (ACC) South of 50-60°S (Ferrari and Wunsch 2009).

The AABW, during their journey northward, will therefore first encounter internal lee wave generation and dissipation before that of internal tides, giving the former waves a very special role. To date, little is known of internal lee wave (ILW) propagation and dissipation, all the more so concerning diapycnal mixing in the interior.

Energy pathways of internal lee waves

Although it is still lacking, knowledge of the energy pathways of ILW has grown in recent years. Polzin et al. (1997) observed large amplitude of diapycnal mixing in mountainous areas with strong deep reaching currents and suggested it was due to the presence of an intense internal lee wave field. The internal lee wave generation mechanisms at play and estimations of the energy they carry lead to further studies (Scott et al. 2011, Wright et al. 2014, Nikurashin and Ferrari 2011). Other studies were interested in the propagation and final dissipation of the waves through diverse interaction mechanisms, such as wave-mean flow interactions through critical layers for instance (Booker and Bretherton 1967). More recently, Nikurashin and Ferrari (2010) suggested from numerical simulations that a degenerate case of internal wave (the inertial oscillations,

or IO) could be key factors in the energy pathways and dissipation of internal lee waves.

Despite these numerous studies, the energy pathways of internal lee waves remain very intricate, and an accurate representation of the energy emission, transfers and dissipation is still missing. For instance, the energy conversion rate into internal lee waves is subject to much debate (Waterman et al. 2014, Wright et al. 2014), and several mechanisms that appear to be important are often lacking in interaction representations (such as the IOs suggested by Nikurashin and Ferrari (2010) or momentum deposition from breaking internal waves to the mean flow). As such, understanding and representing the dissipated energy responsible for diapycnal mixing seems complex and might require considering a number of energy pathways at once. This can only be achieved when the nature of these energy pathways is known, before tackling their implications on diapycnal mixing.

Outline of this manuscript

In this manuscript, we propose to investigate the *energy pathways* taken by internal lee waves in the deep ocean and describe the *implications* of this evolution on turbulent kinetic energy dissipation. As seen above, doing so raises quite a few questions, from the observations available from the real ocean, to the sources of the energy pathways, and the role of inertial oscillations and turbulent kinetic energy dissipation in these pathways. These questions can be organized into four different topics:

- To investigate TKE dissipation, the foremost step is to gather field measures of the energy dissipation rates in the ocean. Several techniques can be used, mainly depending on the spatial scale of interest. These techniques are differently done, rely on various hypotheses and different ranges of validity. This raises the questions of **how estimates of TKE dissipation are gathered, and under which conditions can these estimates be inferred.**

- The energy pathways in the ocean are intricate and complex, start from various sources and take different routes. There exist several major energy reservoirs available, which are not equivalent regarding to their impact on the ocean currents. Regarding the case of AABW consumption, there may exist an energy source and process particularly relevant for investigating the energy pathways. One may wonder **what processes and energy reservoirs should be taken into account** to shed light on AABW consumption.
- It has been suggested in previous studies that inertial oscillations might be key to understanding the energy pathways of internal lee waves. The kinetics of this interaction are of great interest, and could inform on the conditions when these two wave motions can interact. The specific role of the inertial oscillations in the energetic route of the lee waves deserves due consideration. This points to the need of investigating and quantifying the **role of inertial oscillations in the energy pathways of the internal lee waves.**
- Of the processes thought to impact on internal waves, some are fundamentally dependent on energy dissipation, some are not. Non-linear effects could be sufficient for creating strong interactions in the flow and for conditioning internal waves to ulterior energy dissipation. **The respective roles of dissipative and non-dissipative interactions in the energy pathways** must be clarified in order to fully understand the nature of the mechanisms at play.

We will attempt to answer these questions by allying literature reviews, numerical simulations and theoretical computations. Through these three aspects we aim at joining together as much as possible the three main ways of studying the ocean: field campaigns, computing and black-boarding.

- In chapter 1 we will investigate the existing approaches and methods of inferring diapycnal mixing. These evaluations are called parameterizations since they make use of diverse assumptions, depending on the available

data. We will review parameterizations of different scales, from the millimeter level to global estimates.

- In chapter 2 the simulations used to ground and evaluate the theory will be described. Two dimensional simulations were used for the rapidity of their calculation and for comparison with previous works. All the simulations are non-hydrostatic, meaning they permit the existence of full vertical pressure gradients, and the full resolution of internal waves.
- Chapter 3 describes an extension of the dissipative asymptotic theory of Nikurashin and Ferrari (2010) in the vertical direction. From so doing we will attempt to describe the temporal numerical evolution of inertial oscillations and TKE dissipation, as well as their vertical structure.
- In chapter 4 we will make use of a different non-linear theory that does not fundamentally rely on energy dissipation: the Resonant Interaction Theory (RIT). The RIT will be used to investigate the rate of growth of the inertial oscillations in the light of the numerical simulations. The comparison of two separate theories for the same phenomenon will shed light on the mechanisms at play in the energy pathway.
- Chapter 5 is a discussion on the implications of the two dimensional hypothesis and how to free the calculations from any unphysical dynamics. We will then attempt to build a three dimensional setting that would permit to fully explore the full panel of mechanisms present in the ocean. We will show that the Transformed-Eulerian Mean (TEM) framework may be an appropriate tool for finely investigating wave-mean flow interactions.

Diapycnal mixing in the ocean: from ocean sampling to ocean modelling

1

As discussed in introduction, the three dimensional distribution of diapycnal mixing is fundamental in setting the global overturning circulation. However, gathering information on diapycnal mixing rates in the ocean can prove to be tricky. This chapter describes the existing ways to estimate diapycnal mixing rates. We will present the assumptions made in each case, and attempt to have a critical view of which physical aspects are missing.

1.1 From Turbulent Kinetic Energy dissipation rates to diapycnal mixing: energy conservation

Insight can be gathered by writing basic energy conservation equations. Stating that the production rate of turbulent kinetic energy results from its creation by the turbulent buoyancy fluxes, its destruction through dissipation, and assuming that the medium is statistically steady, one gets (Osborn 1980):

$$\mathcal{P} \simeq -\rho\mathcal{E} + \mathcal{B} \,, \tag{1.1}$$

where $\mathcal{P}$ is the rate of production of turbulent kinetic energy, $\mathcal{E}$ is the rate of dissipation of turbulent kinetic energy, and $\mathcal{B} \sim \rho_0 N^2 K_v$ is the rate of work against gravity done by turbulent buoyancy fluxes.

Let us assume that the turbulent buoyancy fluxes vary in fixed proportions with the turbulent production:

$$\mathcal{B} = R_f \mathcal{P} \tag{1.2}$$

where R_f is a flux Richardson number. It then follows that:

$$\mathcal{P} = \frac{\rho}{R_f - 1}\mathcal{E} \text{ , and} \tag{1.3a}$$

$$K_v = \frac{R_f}{1 - R_f}\frac{\mathcal{E}}{N^2} \tag{1.3b}$$

This equation directly relates the diapycnal mixing with the turbulent kinetic energy dissipation rate and the local stratification. Since turbulent kinetic energy dissipation rate is much easier to measure than diapycnal mixing, oceanographers largely use this equation, a corner stone for most recent diapycnal mixing research. However, although straightforward to gather, direct measurements of the TKE dissipation rate are still very sparse, especially in the Southern Ocean were rough weather and ice cover hinder field campaigns.

There are several ways to tackle the lack of knowledge of turbulent kinetic energy dissipation rates, depending on the (vertical) scale considered. One can directly measure $\mathcal{E}$ on centimeter scale (hereafter noted micro-scales) through microstructure casts. Fieldwork can also be done by inferring TKE dissipation rate from scales of tens to hundreds of meters (hereafter noted fine-scales) through finescale parameterizations. Another way of getting insight on the diapycnal mixing distribution can be achieved through numerical models, and the numerical estimate of turbulent kinetic energy dissipation from precise knowledge of the topography and the flow characteristics. Finally, a yet more global approach that somewhat gets further from measuring diapycnal mixing, is to make an early estimate of K_ρ so as to be able to gather information on the response of the ocean to variations in the mixing distribution.

These four approaches will be described in the following chapter.

1.2 Micro-structure: a local measure

A seemingly basic step towards understanding the energetics of the ocean's interior is to measure in situ energetic variables. This requires deploying instruments such as Vertical Microstructure Profilers (VMP, Carter and Imberger 1986)

in the ocean interior, and tracking the flow characteristics on small scales. The field of interest for this study is the turbulent kinetic energy dissipation rate, a primary proxy towards diapycnal mixing rates (Eq. 1.3b).

Turbulent kinetic energy dissipation occurs on scales of centimeters (micro-scales). This makes measuring TKE dissipation rates quite a technical challenge, for several reasons. Since differences measured on centimeter scales are bound to have a large uncertainty compared to the absolute signal, the accuracy of the measures is critical to obtain precise data. Moreover, measuring micro-scales requires probes arranged as dipoles, each pole being distant from the other by about a centimeter. These probes are delicate and onerous. Finally, as movements of the ship would transmit motions to the instrument and disrupt the local measure and local dissipation rate, the profiler is required to be detached from the ship, free falling towards the bottom. A free falling device must be very finely tuned. If it comes back up too early, all the bottom dissipation would not be measured. But if it sinks too deep, it might touch the ocean floor, which would lead to the complete loss of the instrument. All of this contributes to difficult technical issues, high instrument cost and the need of large specific knowledge for its operation.

As such, micro-structure measurements are very accurate and provide great and insightful knowledge, however they are very sparse and do not cover the very bottom of the ocean, which is the main limitation in their applicability.

1.3 The fine-scale parameterization: inferring mixing from shear and stress

Since directly measuring TKE dissipation rate is so tricky, progress was made to infer less reliable dissipation rates from more easily obtained data. Most ocean datasets contain information on velocity and density structure on scales of tens to hundreds of meters (hereafter called fine-scales, Polzin et al. 2014). The aim of fine-scale parameterizations was to estimate rates of turbulent kinetic

energy dissipation from such datasets. They use density and/or velocity profiles obtained from standard CTD and ADCP measurements, far more extensive, easy to obtain and of resolution of tens to hundreds of meters. Since the leading order of the ocean's interior energy field is attributed to internal waves (Ferrari and Wunsch 2009), the fine-scale parameterizations make use of the wave properties (shear and strain) to infer the turbulent kinetic energy dissipation rate. The use of such parameterizations has greatly increased over the recent years, and although the results are extremely sensitive (to the scheme used as well as to the way the data is handled) and approximative (up to an order of magnitude different from the micro-structure data), some great insight into the turbulent kinetic energy dissipation rate was achieved.

The fine-scale parameterization considers that the rate of turbulent production $\mathcal{P}$ in the internal wave field is determined by the spectral energy transport in the vertical wave-number domain $F(m)$ (integrated over frequencies). Although a diversity of studies parameterise $\mathcal{P}$ depending on the fields available (Polzin 2004, Olbers and Eden 2013), we will focus on the study by Polzin (2004) for simplicity.

Through combining heuristic arguments and dimensional parameters, Polzin (2004) arrive at

$$\int F(m,\omega)d\omega \xrightarrow[m\to\infty]{} \mathcal{P} \quad , \tag{1.4}$$

the rate of turbulent production arises from the total energy transport.

Finally, using ray tracing theory, these authors find an analytic expression for the energy transport:

$$F(m,\omega) \simeq 2Am^4N^{-1}\phi(\omega)E(m,\omega)E_k(m) \tag{1.5}$$

where $\phi(\omega) = |\boldsymbol{k}_h|/m = \sqrt{(\omega^2 - f^2)/(N^2 - \omega^2)}$ is the tangent of the angle of the internal waves' wavenumber to the vertical, $A = 0.20$ is a non-dimensional constant, and E_k and E are the kinetic and total energy, respectively.

In the absence of detailed energy spectrum datasets, it is easier to use the

ratio of horizontal kinetic and potential energy, or shear to strain ratio:

$$R_\omega = \frac{E_k}{E_p} \tag{1.6}$$

The lack of resolution in the spectral energy transport can further be made for by estimating the average energy density by reference to the Garret-Munk shear spectrum:

$$\hat{E} = \frac{[\frac{1}{m_2 - m_1}\int_{m_1}^{m_2} 2m'^2 E_k(m')dm']}{[\frac{1}{m_c}\int_0^{m_c} 2m'^2 E_k^{GM}(m')dm']} \tag{1.7}$$

where m_1 and m_2 are the boundaries of the energy spectrum considered, and m_c is a high wavenumber representing a transition into wave breaking phenomena, that is not precisely defined but can nonetheless be expressed through different equalities (Polzin et al. 2014). The use of a non-dimensionalized energy density is usefull in narrowing down measure errors by using a regerence spectrum, heretaken as the Garret-Munk shear spectrum. However, issues of bias can become problematic as the spectrum departs significantly from that of the Garret-Munk prescription.

More calculations, approximations and physical arguments lead to the Radiation Balance Equation (RBE, Polzin et al. 2014:

$$\mathcal{P} = \mathcal{P}_0 \frac{f}{f_0} \frac{N^2 \cosh^{-1}(N/f)}{N_0^2 \cosh^{-1}(N_0/f_0)} \hat{E} \frac{3(R_\omega + 1)}{4R_\omega} \sqrt{\frac{2}{R_\omega - 1}} \tag{1.8}$$

where $\mathcal{P}_0 = 8 \times 10^{-10}$ W.kg^{-1}.

Throughout the calculations needed to obtain the final dissipation estimate, many assumptions were made, and have to be kept in mind:

- The finescale parameterizations are best employed at intermediate vertical scales.
- Small vertical scales ($m > m_c$) are here considered to be part of wave breaking, and as such define a limit to the spectral interval studied.
- Large vertical scales can also become problematic, with the growing effects of wave-mean interactions, and possibly other interactions not taken into account by the parameterization.

- A central condition is that the downward spectral energy propagation is set by wave-wave interactions. This condition is broken by any process that shortcuts the energy cascade, such as wave scattering, wave reflection, or resonant interactions (such as the Parametric Subharmonic Instability).

To top it off, many technical issues arise when dealing with in situ data, such as the definition of the cutoff wavenumber m_c, the definition of bottom stratification or the coarseness of the energy spectrum.

This parameterization, although it uses many assumptions, seems to perform rather well when compared with micro-structure datasets, although the dissipation is systematically overestimated (Waterman et al. 2012).

1.4 Ocean recipes: from topography and stratification to mixing estimates

We have seen that fine-scale parameterizations can provide turbulent kinetic energy dissipation rates from shear and strain ratios, using ray tracing theory. In short, knowing the velocity and buoyancy profile, as well as the energy spectrum, is enough to apply the fine-scale parameterization.

Current knowledge could allow one to predict the energy spectrum in the fluid column from information on the flow and the topography. Assembling both theories would enable one the predict the one-dimensional profile of the turbulent kinetic energy dissipation rate from precise knowledge of bottom topography and flow characteristics.

As discussed in the introduction, increasing interest has been taken in internal lee waves, especially in the Southern Ocean. Unfortunately, ocean recipes have been derived for internal tide dissipation (Polzin 2009), but have yet to be published for internal lee wave dissipation (work in progress, also by K. Polzin). We will here focus on the published internal tide problem, and add comments on how the internal lee wave problem can be adapted to it.

Such theories, named ocean recipes, have the advantage that they only re-

quire *external* variables of the problem, such as a buoyancy profile, a topographic spectrum and either geostrophic velocity profile (in the case of internal lee wave) or barotropic tide (in the case of internal tides). These variables have the advantage that they are nearly all available outputs of ocean models (apart from the ill-known topographic spectrum), and are readily available.

1.4.1 Getting the bottom energy conversion

As just said, the major step towards obtaining the energy dissipation rate is to compute the energy spectrum, before the fine-scale parameterizations can take over. To compute the energy spectrum, the energy sources and their spectral distribution have to be considered. Several energy sources for internal waves are available, and can mainly be divided into wind generation at the surface and generation by interaction with topography (at the bottom). The ocean recipes described here focus on the bottom generation. Polzin (2009) further asserts that additional energy sources would easily be taken into account in the recipe.

Internal tides

Polzin (2009) uses a quasi-linear spectral model of internal tide generation based on Bell (1975):

$$E_{flux}(k,l,z=0,t) = \sum_n E^n_{flux}(k,l,\omega_n,z=0,t) \tag{1.9}$$

$$E^n_{flux}(k,l,\omega_n,z=0,t) = \frac{\omega_n}{2\pi^2}\left[\left(N^2-\omega_n^2\right)\left(\omega_n^2-f^2\right)\right]^{1/2}[k^2+l^2]^{-1/2} \tag{1.10}$$

$$\times H(k,l)J_n^2\left(\left[(k^2U_0^2+l^2V_0^2)/\omega_1^2\right]^{1/2}\right) \tag{1.11}$$

where E_{flux} is the horizontal wavenumber-frequency spectrum for the vertical energy flux, J_n is a Bessel function of the first kind of order n and $H(k,l)$ is the topographic spectrum. ω_1 is the fundamental frequency of the barotropic tide, U_0 and V_0 are its amplitudes. $\omega_n = n\omega_1$ is the frequency of the n-th harmonic, where n is an integer such that $f^2 < \omega_n^2 < N^2$.

The topographic spectrum $H(k,l)$ is generally not detailed enough for practical calculations, but it can be fitted on theoretical estimations. Abyssal hills created by volcanism and faulting at mid-ocean ridge crests are a major source of sea floor roughness of horizontal scale 1-10 km. Considering the generation process of such topography, Goff and Jordan (1988) characterized abyssal hills as:

$$H(k,l) = \frac{4\pi\nu h_0^2}{l_0 k_0 \left(\frac{k^2}{k_0^2} + \frac{l^2}{l_0^2} + 1\right)^{(\nu+1)}} \tag{1.12}$$

where k_0, l_0 are roll-off wavenumbers, h_0 is the rms height, and ν is a non-dimensional parameter. Thus, after fitting the basin topography on 1.12, one gets the horizontal wavenumber-frequency spectrum energy flux generated at the bottom as a function of tidal properties for all harmonics.

Internal lee waves

The bottom energy emission for internal waves is comparable to that associated with internal tides, the difference being that $\omega_n = n\omega_1 - \boldsymbol{k}.\overline{\boldsymbol{u}}$, and ω_1 is the frequency of the oscillatory flow, and can be either M_2 or f.

Note that this computation relies on two-dimensional, linear dynamics, which are thought to greatly misestimate the bottom energy conversion (Nikurashin et al. 2014, Wright et al. 2014)

1.4.2 The nonlinear propagation model

As seen in the previous section, there are various ways of predicting the evolution of the internal wave spectrum knowing the ambient buoyancy and velocity profiles. Combining the energy spectrum of the waves generated at the bottom with a nonlinear propagation model (such the RBE used by Polzin 2004 or other ray-tracing theories as in Olbers and Eden 2013), it becomes possible to calculate the one-dimensional profile of internal wave energy dissipation in the water column (Polzin 2009). From this, using Eq. 1.3b, on gets diapycnal mixing estimates through the water depth.

To our knowledge, only two field campaigns have taken interest in the internal lee wave driven mixing in the Southern Ocean (Naveira Garabato 2009, Sheen et al. 2013). A collaboration with S. Waterman, A. Brearley and A. Naveira-Garabatto (NOC Southampton) was developed to compare energy dissipation rates inferred from an Ocean recipe to micro- and fine-structures captured during the SOFine cruise. An internal lee wave ocean recipe still under work was implemented and compared to VMP measurements, but remaining uncertainties (in the calculation of the bottom geostrophic velocity or stratification for instance) currently prevent concrete conclusions. This work is still in progress will not be presented in this document.

1.4.3 Caveats

Although such recipes are extremely promising for predicting buoyancy fluxes and diapycnal mixing both in field estimations and model parameterization, several limitations prevent their systematic use for now.

Let us first be reminded that the calculations are made in terms of buoyancy fluxes. Getting to diapycnal diffusivity requires further approximations that may bring errors in the final estimate.

The recipe consists in a one-dimensional (vertical) calculation, done on what can be considered as a grid cell, and does not consider any lateral fluxes. This can be a considerable drawback in high resolution cases where a lot of energy can propagate from one cell to another.

The bathymetry representation misses a lot of ocean topographic features, such as offset fractures or mud waves for instance. This can lead to an underestimate of the low vertical wavenumber internal wave field, and subsequently the energy flux. Polzin (2009) estimate the mismatch to be of order 20-40%.

Furthermore, setting the parameters of the bathymetry spectrum requires high resolution datasets, which are generally lacking.

Finally, a lot of processes are not taken into account in current recipes (the

same as those ignored in the fine-scale parameterizations, plus the waves not taken into account by the generation process). This could make the recipes useful only in specific cases, or for process oriented studies.

1.5 Towards global estimates

Despite the lack of knowledge on the three-dimensional distribution of diapycnal mixing, its representation in ocean models is the object of high concern (Ito and Marshall 2008, Jayne 2009, Marshall and Naveira Garabato 2008, Melet et al. 2013; 2014, Waterhouse et al. 2014). We will here sum up the main approaches that have been proposed to get a global pattern of the turbulent kinetic energy dissipation rate and diapycnal mixing. We will focus on bottom mixing, and will not address phenomena occurring in the upper ocean.

1.5.1 Getting a global coverage of TKE dissipation

As explained above, the diapycnal mixing is most commonly inferred from the turbulent kinetic energy dissipation rate. Moreover, the global distribution of TKE dissipation rate is generally represented as depending solely on its horizontal location. That is, the amplitude of the TKE dissipation rate is set at a given longitude and latitude, whereas its vertical distribution obeys the same scaling whatever the horizontal location (St. Laurent et al. 2002, Melet et al. 2013, Saenko et al. 2012):

$$\mathcal{E} = \frac{qE(x,y)F(z)}{\rho} \tag{1.13}$$

where $E(x,y)$ is the energy flux into internal waves, q is the fraction of this energy flux that is assumed to be dissipated in the water column and $F(z)$ describes the vertical structure of TKE dissipation.

Such a parameterization is poorly constrained and lacks most of the physics going on, but it has the advantage of being easily implemented into ocean models.

Horizontal variability: $E(x, y)$

The horizontal distribution of internal wave emission can take several components into account, depending upon the processes studied. We saw in the previous section how the bottom emitted waves (the internal tide or the internal lee waves) can be computed from bathymetry estimates. These are the main contributors to the internal wave field in the ocean, and do not take into account long range wave propagation or wave scattering. These energy source estimates are based on weakly non-linear, two-dimensional computations. A three-dimensional, fully turbulent computation is needed to fully represent the bottom energy conversion from the geostrophic flow into internal lee waves. Finally, large scale fields such as the bottom geostrophic velocity, bottom stratification or precise datasets such as the topographic spectrum are largely unknown and are responsible for large uncertainty in the final TKE dissipation rate estimated.

Vertical profile: $F(z)$

We saw in the previous section how precise, process based vertical profiles of TKE dissipation rate can be obtained in ocean recipes. However, these have not yet been implemented in ocean models due to computing costs, and more rudimentary, empirical parameterization have been used.

One vertical profile largely used in previous years accounts for the decrease in diapycnal mixing away from topography with an exponential decay (St. Laurent et al. 2002, Saenko and Merryfield 2005, Simmons et al. 2004, Jayne 2009). However, Polzin (2004) rather use a decreasing power law, that allows for a gentler decay of bottom mixing with height, and Melet et al. (2013) use a somewhat more complex profile. All these implementations have in common a very simple, horizontally homogeneous vertical distribution, poorly constrained, that is broadly based on observations but lacks physical principles. Lavergne et al. (submitted) conducted a comparative study of different descriptions of the ver-

tical profile, which indicate a strong dependency of the overturning strength on the parameterisation used.

Energy fraction locally dissipated: q

In early studies, only the energy locally dissipated was taken into account, the near-field mixing, which is commonly taken as 20% of the total emitted energy ($q = 0.20$, Osborn 1980). This is far from correctly representing the complex energy pathways that occur along the trajectory of an internal wave. Moreover, the energy dissipated away from the emission site (far-field) has rarely been taken into account for parameterisations (Oka and Niwa 2013), although it represents the major part $(1 - q)$ of the energy dissipation occurring in the ocean.

1.6 Summary of the diapycnal mixing parameterizations

As we have seen in this chapter, present diapycnal mixing parameterizations are plenty, and vary depending on the scale they are supposed to represent. They are not yet quite exhaustive, as they often lack dependency on the fluid properties, and more generally do not fully represent all the physics at play.

As for the diapycnal mixing distribution due to topographic interactions with a bottom reaching flow, the horizontal distribution of the oceanic internal lee wave conversion rate $E_{ILW}(x, y)$, although still incomplete, is better known than its vertical dependency (Nikurashin et al. 2012). It appears that most (roughly half) of the energy internal lee wave emission occurs in the Southern Ocean, which accounts for about 10% of the total internal wave energy emission around the globe (Nikurashin et al. 2012). This is explained by the rough topography and intense deep currents encountered in those parts. However, earth rotation then needs to be taken into account, and the parameterizations presented in this section only *extrapolate* results from a non rotating frame to the rotating case.

They lack the direct representation of rotation in the spectral exchanges, or the possible existence of strong inertial oscillations.

2 A first look at the phenomenology: numerical simulations

The previous chapter showed that the current parameterizations of TKE dissipation in the ocean lack physical insight, especially concerning the impact of rotation on the mechanisms at play. The present chapter focuses on the two-dimensional numerical simulations that were used to investigate the energy pathways from internal lee wave emission to TKE dissipation. For comparison purpose, we used the same setup, albeit a different model, as Nikurashin and Ferrari (2010).

2.1 Introduction of the numerical case study

2.1.1 Physical configuration

We study a simple case of a uniform flow of amplitude $U_G = 0.1$ m.s^{-1} over a topography as simple as possible. Thus the topography is chosen to be invariant along the y direction and sinusoidal in the x direction: $h(x, y) = h_T \cos(\frac{2\pi x}{l_T})$, where h_T varies in the range {20 m, 40 m, 80 m} and l_T is either 2 km or 1.2 km. The physical domain is 2 km high. The stratification is such that the Brunt-Väisälä frequency is $N = 10^{-3}$s^{-1}, and the Coriolis frequency is $f = 10^{-4}$s^{-1}

Figure 2.1 is a sketch of the two-dimensional physical configuration considered, the sloped lines representing the ILWs.

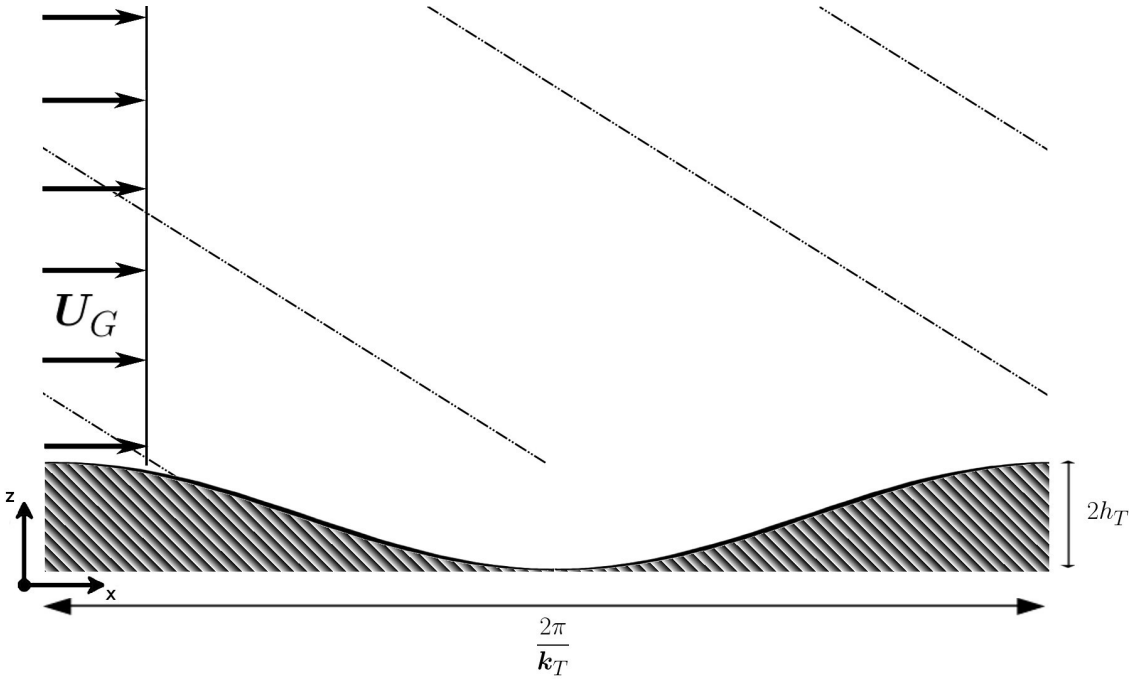

Figure 2.1 – *Physical setting used in the numerical simulations. The forcing consists in a uniform, constant flow U_G. The two-dimensional topography is sinusoidal, of wavenumber k_T, and peak to peak distance 2 h_T. Internal lee waves are thus generated and radiate away from the bottom. Their phase is sketched by the dotted lines.*

The different simulations and their corresponding names are listed in table 2.1.

2.1.2 Numerical set-up

Model description

The numerical simulations were carried out with Symphonie NH, a non hydrostatic regional ocean model (Auclair et al. 2011) developed by the Pôle d'Océanographie Côtière (POC, Toulouse, France). We shall now describe the equations and assumptions used in Symphonie NH.

$$\partial_t \boldsymbol{u} + [(\boldsymbol{u}.\boldsymbol{\nabla}) \cdot \boldsymbol{u}] - f\boldsymbol{e}_z \wedge \boldsymbol{u} = -\frac{1}{\rho}\boldsymbol{\nabla} p + \boldsymbol{g} + \nu\nabla^2\boldsymbol{u} \tag{2.1a}$$

$$\boldsymbol{\nabla} \cdot \boldsymbol{u} = 0 \tag{2.1b}$$

$$\partial_t \rho + (\boldsymbol{u}.\boldsymbol{\nabla})\rho = \kappa\nabla^2\rho \tag{2.1c}$$

Name	L	h_T	f	Bottom condition
$H_{20}L_2$	2 km	20 m	1.10^{-4} s^{-1}	Partial-slip
$H_{40}L_2$	2 km	40 m	1.10^{-4} s^{-1}	Partial-slip
$H_{80}L_2$	2 km	80 m	1.10^{-4} s^{-1}	Partial-slip
$H_{20}L_2\_fs$	2 km	20 m	1.10^{-4} s^{-1}	Free-slip
$H_{40}L_2\_fs$	2 km	40 m	1.10^{-4} s^{-1}	Free-slip
$H_{80}L_2\_fs$	2 km	80 m	1.10^{-4} s^{-1}	Free-slip
$H_{20}L_{1.2}$	1.2 km	20 m	1.10^{-4} s^{-1}	Partial-slip
$H_{40}L_{1.2}$	1.2 km	40 m	1.10^{-4} s^{-1}	Partial-slip
$H_{80}L_{1.2}$	1.2 km	80 m	1.10^{-4} s^{-1}	Partial-slip
$H_{40}L_2\_2f$	2 km	40 m	2.10^{-4} s^{-1}	Partial-slip
$H_{80}L_2\_2f$	2 km	80 m	2.10^{-4} s^{-1}	Partial-slip

Table 2.1 – *Summary of the different two-dimensional simulations. The simulations vary by the height or the wavelength of the topography, by the bottom boundary condition or by the value of the Coriolis frequency.*

where $\boldsymbol{u} = (u,v,w)$ is the three-dimensional velocity, ρ is the density, p is the pressure, $\boldsymbol{g}$ is the gravitational acceleration, ν is the kinematic viscosity and κ is the diffusivity of density.

The Boussinesq assumption relies on the statement that the density variations in the fluid around a reference value are small, so that these variations can be neglected in the acceleration term.

$$\rho = \rho_0 + \rho' \qquad , \rho' \ll \rho_0 \tag{2.2a}$$

$$p = p_0 + p' \qquad , p' \ll p_0 \tag{2.2b}$$

where $\rho_0 = 1026$ kg.m^{-3} is the reference density, and the hydrostatic pressure follows $\partial_z p_0 = \rho_0 g$.

Under the Boussinesq assumption, the equations of motion hold:

$$\partial_t \boldsymbol{u} + [(\boldsymbol{u}.\boldsymbol{\nabla}) \cdot \boldsymbol{u}] - f\boldsymbol{e}_z \wedge \boldsymbol{u} = -\frac{1}{\rho_0}\boldsymbol{\nabla} p' + \frac{\rho'}{\rho_0}\boldsymbol{g} + \nu\nabla^2\boldsymbol{u} \tag{2.3a}$$

$$\boldsymbol{\nabla} \cdot \boldsymbol{u} = \boldsymbol{0} \tag{2.3b}$$

$$\partial_t \rho' + (\boldsymbol{u}.\boldsymbol{\nabla})\rho' = \kappa\nabla^2\rho' \tag{2.3c}$$

Symphonie NH is a non-hydrostatic model. This means that the pressure at a given location is not only set by the weight of the fluid above it (the hydrostatic pressure), but also by the fluid motion itself, such as the vertical acceleration or friction. This is a necessary condition for accurately resolving internal waves at ten to hundred meter scales, which have strong vertical accelerations. The non hydrostatic pressure is computed by solving the three-dimensional Poisson equation:

$$\nabla^2(p') = f \tag{2.4}$$

where f is a function of the dynamic fields.

Since most computing and solving techniques can only work through finite iterations, the continuous time and space have to be divided into small entities, called time-steps and grid cells. This is called discretization. The larger the time step and grid cell, the further away the computed solution gets from the continuous solution, but a small decrease in discretization greatly increases the total length of the computation, so that a compromise has to be reached. The spatial grid of the model can either use $z-$ or $\sigma-$ coordinates (Bergh 2010), as will be explained below. The z-coordinates are the most straightforward vertical coordinates, as they are fixed in space and time, in a horizontal slicing of the vertical space. However, due to the step-like representation of bottom topography, accuracy decreases in the bottom layer. The σ-coordinates make up for this disadvantage by following both the bottom and the surface. Given a static depth H, and a free surface of height $\eta(x, y)$, the z-coordinates can be changed into σ-coordinates from the relation:

$$\sigma = \frac{z - \eta}{H + \eta} \tag{2.5}$$

where σ ranges from $\sigma = 0$ at the surface ($z = -H$) to $\sigma = -1$ at the bottom ($z = \eta$). This coordinate has the drawback that in cases of strong topographic slope, the grid may introduce errors in the representation of the pressure gradient.

Setting description

The numerical grid we used has a fixed spacing in the horizontal ($\Delta x = 12.5$ m) but topography-following (σ)-coordinates along the vertical, so as to have more accurate results near the topography. The physical configuration being initially made of a uniform flow over a y-invariant, x-periodic topography allows us to use 2D (along y) configurations with periodic boundaries along x. To avoid wave reflection from the upper boundary, we apply a damping layer from 2km to the upper boundary at 7km. In this layer, the vertical grid spacing is stretched from about 5m to about 300m to lower the computing cost of a simulation. Additionally, the viscosity and diffusivity are increased in proportion with the vertical grid spacing Δz. The domain size is $L = l_T$, $H = 7$ km. The viscosity and the diffusivity are respectively set to 10^{-2} and 10^{-3} $m^2.s^{-1}$. The bottom boundary conditions are set to either free slip or partial slip with a bottom rugosity of 1mm. The uniform flow is forced through an additional body force fU_G in the meridional momentum equation, after a transient period of 24 h.

The flow indeed started from rest. During the first 24 h the fields are relaxed to the desired values with a time-scale of 3 h, avoiding spurious spin-up effects. Afterwards, the relaxation is removed (but not the forcing), and the integration is carried on for 15 days, so as to reach statistical equilibrium.

2.1.3 Off the hat behavior

As a fluid parcel is moved from equilibrium in the vertical plane, a stable stratification attracts the parcel back to its initial position in an oscillatory fashion that is damped only in the presence of viscosity. As it is moved from its resting position in the horizontal plane, rotation deviates it horizontally, in another undamped oscillation. These two wave-like processes (vertical and horizontal) give birth to what are called internal waves. Since the particular waves studied

here are generated at the topography and can be seen on its lee side, they are called internal lee waves (Bell 1975).

Internal waves, as most waves in the ocean, can have quite the eventful life.

- In the most peaceful case, where the topographic height is much smaller than the vertical length scale of the internal waves radiated ($h_T m_{ILW} << 1$, where m_{ILW} is the vertical wave-number of the ILW), the waves have a small amplitude, and the wave field is described as linear, or quasi-linear in cases where this is marginally the case. Such cases are easily described theoretically, since the different waves of the total field hardly interact with each other.
- If the amplitude of the waves rises, the internal wave field becomes non-linear, and interaction between different waves can become of leading order. Linear and quasi-linear theories often fail to capture important aspects of such flows.
- Finally, when the amplitude of the waves becomes large enough so that overturning occurs, they become unstable through convective instability and dissipate into the ambient flow. This is called wave breaking.

Linear internal lee waves are stationary in the frame of reference attached to the topography: from the point of view of an observer in this reference frame, their frequency (or absolute frequency) is null, their spatial phase structure seems to be frozen in time. However, that is not the case in the frame of reference attached to the flow, due to the Doppler effect (the shift of frequency due to the difference of speed between two frames of reference).

Let us investigate the several spectral properties of the internal waves: their intrinsic frequency (in the moving frame) ω and their wavenumber $\boldsymbol{k} = (k, l, m)$. A relation between these variables can be inferred from the equations of motion linearised around a state of rest, and leads to the *dispersion relation*:

$$\omega^2 = \frac{(k^2 + l^2)N^2 + m^2 f^2}{\boldsymbol{k}^2} \tag{2.6}$$

From the observation that $f \leq N$ in the ocean, this entails that $f \leq \omega \leq N$.

By definition, the phase of the waves propagate at the phase speed $\boldsymbol{c}_\phi = \omega/\boldsymbol{k}$, but the energy of the waves propagates at the group velocity $\boldsymbol{c}_g = (\frac{\partial\omega}{\partial k}, \frac{\partial\omega}{\partial l}, \frac{\partial\omega}{\partial m})$. From the dispersion relation, this entails that $\boldsymbol{c}_g.\boldsymbol{k} = 0$, the energy of the waves propagates orthogonally to their wavenumber. Moreover, the vertical component of the phase speed $\frac{omega}{m}$ is of opposite sign to the vertical group velocity c_g^z. For instance, an internal wave propagating energy upwards has a negative vertical wavenumber if $\omega > 0$. Although the fluid motions do not set any particular constraints on (k, l, m), some more information can be gathered for the internal lee waves originally emitted from the topography. Supposing the fluid flows at horizontal speed $\boldsymbol{U}_G$ above a monochromatic topography of horizontal wavenumber $\boldsymbol{k}_T$, the spectral properties of the lee wave are

$$k = k_T \tag{2.7a}$$

$$l = l_T \tag{2.7b}$$

$$\omega = -\boldsymbol{U}_G.\boldsymbol{k}_T \tag{2.7c}$$

and m can be inferred from the dispersion equation ($m \geq 0$ since the energy of the wave must propagate upwards, due to the presence of topography at the bottom and $\omega < 0$).

Basic features of the flow behavior in general and internal lee waves in particular are illustrated in Fig. 2.2, at two successive times. After one inertial period (Fig. 2.2a), quasi-linear internal lee waves have been radiated and propagate upwards. The wavenumber and phase speed are perpendicular to the phase lines, whereas the group velocity is parallel to the phase lines. Over the range of parameters studied, the topography is sub-critical, namely the slope of wave propagation exceeds the slope of the topography, and the waves can propagate without encountering reflection or energy trapping. After seven inertial periods (Fig. 2.2b), wave breaking occurs at the bottom of the domain, below 1000 m.

In the following, we decompose the flow into three components following Nikurashin and Ferrari (2010), namely the geostrophic flow, the inertial oscillations and the internal waves. The geostrophic flow is set to the constant value

of $U_G = 0.1$ m.s^{-1}, along the x-direction. In the idealized case we are considering here, IOs are internal waves of frequency f; their horizontal scale is therefore infinite. Their vertical scale is finite although it is not defined by the dispersion relation. Hence the IO velocity field may be considered as depending upon height and time only. This motion is defined as the remaining motions: $\boldsymbol{U}_{IO}(t,z) = \overline{\boldsymbol{u}(x,z,t) - U_G}^x$, where $\overline{(.)}^x$ denotes a horizontal average. Finally, the internal waves are defined as $\boldsymbol{U}_{ILW}(x,z,t) = \boldsymbol{u}(x,z,t) - \boldsymbol{U}_G - \boldsymbol{U}_{IO}(t,z)$, or $\boldsymbol{U}_{ILW}(x,z,t) = \boldsymbol{u}'(x,z,t)$, where $\boldsymbol{u}'(x,z,t) = \boldsymbol{u}(x,z,t) - \overline{\boldsymbol{u}(x,z,t)}^x$. Hence the internal wave field has a zero horizontal average by definition, which is consistent with the periodic boundary conditions.

As discussed in the introduction to this manuscript and in chapter 1, the dissipation rate of turbulent kinetic energy $\mathcal{E}$ is central to the analysis of non linear wave dynamics. We recall the definition of $\mathcal{E}$ for a two-dimensional flow in a vertical plane (Lesieur 1990 p 267, eq (IX-3-6) , Koudella and Staquet 2006):

$$\mathcal{E} = 2\rho\nu(\partial_z u' - \partial_x w')^2 \tag{2.8}$$

We will now have a first look at the behavior of this field along with the IO field in our simulations.

2.2 Description of the Turbulent Kinetic Energy dissipation rate

Let us first look at the general behavior of the TKE dissipation rate through a few simple cases. The basic settings we will take as references consist in a 2 km wide topography of amplitude ranging from 20 to 80 m with free-slip bottom boundary conditions: the L_2_fs cases.

Figure 2.3 shows the evolution versus time of the TKE dissipation integrated over 2000 m for all the simulations. For near linear cases where $h_T = 20$ m, integrated TKE dissipation increases slowly with time, and does not reach any steady state within the time of integration. The other two simulations reach a

statistically steady state (hereafter named saturation) after a few inertial periods. These simulations then show a slow decay of TKE dissipation rate with time. We shall attempt to explain this behavior later in the manuscript. A difference between the lowest topographic amplitude case and the others can be expected for practically any observation, since the non-linearities greatly influence the flow as a whole.

Figure 2.4 displays the vertical profile of the TKE dissipation rate at the end of the simulations for the L_2_fs cases.

This figure shows that, in these three reference cases, the TKE dissipation rate is clearly enhanced near the topography. The bottom 1000 m show an elevation of up to an order of magnitude in turbulent dissipation. This means that the internal lee waves generated at the topography dissipate strongly shortly after their emission, before continuing their propagation upwards with a rather constant amplitude, without any TKE dissipation. The lowest amplitude case ($h_T = 20$ m) holds a low amount of TKE dissipation. This can be expected, since the waves are quasi-linear: the available energy carried by the waves is smallest, and little turbulence is observed.

Using Eq. (1.3*b*), $N = 10^{-3}$ s^{-1} and assuming $\gamma = 0.2$, the averaged rate of TKE dissipation over the lower 500 m in simulation $H_{80}L_2\_fs$ gives a vertical diffusivity of about $\sim 4.10^{-3}$ m^2.s^{-1}. This value is strong but only slightly above the range of TKE dissipation rate in the deep Southern Ocean inferred from vertical micro-structure profilers (Waterman et al. 2014).

Figure 2.5 shows profiles of the TKE dissipation above a given height for all simulations. The same observations as in Fig. 2.4 can be observed. The profiles show that for all the non-linear cases ($h_T \geq 40$ m), dissipation is clearly enhanced near topography, systematically under 1000 m. The quasi-linear cases do not show much signal in the TKE dissipation field, since wave-wave interactions is very small.

Since there is no interaction with the atmosphere or any initial disturbance

apart from the topography, the energy input results entirely from the conversion from the geostrophic flow to the internal lee wave field at the bottom. Subsequently, the TKE dissipation rate can be directly compared with the bottom energy conversion rate $P_{up} = \overline{p'w'}^{x}|_{z=0}$. Figure 2.6 shows profiles of the integrated TKE dissipation above a given height, z_0, and below $H = 2000$ m for different simulations, scaled by P_{up}. $\int_{z_0}^{H} \mathcal{E}\partial z$ is the energy dissipated in the domain comprised between the topography and height z_0. If all the energy were to be dissipated at a given height z_0, then we would have the equality $\int_0^{z_0} \mathcal{E}\partial z = P_{up}$, or $\int_{z_0}^{H} \mathcal{E}\partial z = 0$. This way, what is plotted on figure 2.6 is a measure of the relative importance between the sink and source terms (given that any motion that radiates above 2000 m is dissipated in the sponge layer).

In figure 2.7 $\int_{z_0}^{H} \mathcal{E}dz$ is scaled by the total TKE dissipation integrated over the bottom 2000 m, $\int_0^H \mathcal{E}dz$. The profile represented is identical to that of Fig. 2.6, except that the sink term is scaled by the total dissipation in the bottom 2000 m. Thus, it ranges from 0 to 1.

Figures 2.7 and 2.6 show that the vertical profile of kinetic energy dissipation is largely independent on the topographic features (h_T, k_T). From the two different normalizations, two types of conclusion can be made: either on the fraction of emitted energy that is dissipated, or on the proportion of the dissipation that occurs below (or above) a certain depth. For our range of parameters we observe on figure 2.6 that at most 20% of the internal lee wave energy produced at the topography is dissipated in the water column. Similar ratios of dissipated to emitted energy have been observed in the ocean by (Sheen et al. 2013, Brearley et al. 2013). In simulations that reach saturation, we observe from figure 2.7 that at least 80% of the dissipated energy occurs below 600 m. In a nutshell, these results confirm those observed in the simulations by Nikurashin and Ferrari (2010).

2.3 Description of inertial oscillations

We shall now describe the inertial oscillations, which are the largest scale motion after the geostrophic current. This brief investigation is carried out on the same reference cases as the beginning of the previous section: the $H_{20}L_{2\_}fs$ cases.

The inertial oscillations have the characteristic of having an intrinsic frequency of $\omega = f$. To observe the presence of waves of specific frequency content, the most straightforward action to take is to observe a power spectrum of a velocity component, say w. To obtain the intrinsic frequency w must be computed in a frame moving at the geostrophic velocity U_G: $w(x') = x - U_G.t$. Figure 2.8 is such a power spectrum for simulation $H_{20}L_{2\_}fs$. The reference case with the lowest topography amplitude is considered since this is where the different waves and frequencies are most distinct (since there is little wave-wave interaction). The dashed line is the confidence level at 99%, implying that the spectrum significantly departs from red noise when it exceeds the dashed line. A peak clearly appears at the frequency $\omega = f$, which indicates the growth of inertial oscillations.

Knowing that inertial oscillations grow during the simulations, we can now have a look at their amplitude and vertical profile. Figure 2.9 displays the vertical profile of the IO amplitude for the $L_{2\_}fs$ reference cases, averaged from 12 to 15 inertial periods. The inertial oscillations have an amplitude that depends on the topographic height, and that can reach the amplitude of the geostrophic current. As the TKE dissipation rate in the previous section, they appear to only be of significance in the bottom 1000 m. In a nutshell, inertial oscillations can become leading order motions and appear to be of importance roughly at the same locations as the TKE dissipation rate. These results confirm those observed in the simulations by Nikurashin and Ferrari (2010).

2.4 On the link between IO amplitude and TKE dissipation rate

Figure 2.9 shows that, as far as energy is concerned, inertial oscillations should not be ignored, as they can contain a subsequent part of the energy of the fluid. Figures 2.4 and 2.9 further indicate that IOs and TKE dissipation rate are clearly enhanced near the topography, roughly in the 1000 m above the bottom. This strong similarity between the IO and TKE dissipation rate profiles suggests that they both are coupled, and that TKE dissipation rate cannot be tackled without first understanding the IOs. We shall here attempt to gather more observations from our simulations so as to compare the TKE dissipation rate to the inertial oscillations.

In the two previous sections, we have observed the profiles and amplitude of the two fields (TKE dissipation rate and IO amplitude) separately. Comparing the two directly can prove to be tricky, since the fields have different dimensions. The TKE dissipation rate can be directly scaled by the bottom energy conversion rate into internal lee waves P_{up}. The IO field could be compared to the geostrophic flow amplitude, but since the latter has the same value for all the cases, we suspect this is not the most judicious choice. The IO field (in m.s^{-1}) is better compared to the TKE dissipation rate if it is converted to energy per unit mass: $E = \frac{1}{2}U_I^2$. This energy can then be compared with the total energy in the ILW field radiated during one period $P_{up}/2\pi/|f|$.

Figure 2.10 shows a scatter plot of the two non-dimensional quantities integrated over the physical domain. To keep information on the $\mathcal{E}$-IO amplitude link, the cases with little IO growth are shown with empty markers, otherwise grey or black markers are used. For the cases corresponding to full markers, a limited range of values for the integrated TKE dissipation rate across the water column is observed, equal to 10 to 30% of the bottom energy conversion. This information was also seen further up in figure 2.6. Although the two-dimensional estimation of P_{up} is probably overestimated (Nikurashin et al. 2014), similar ra-

tios of dissipated to emitted energy have been observed in the ocean (Sheen et al. 2013, Brearley et al. 2013). We also notice that $\frac{1}{2}U_I^2/(P_{up}/2\pi/|f|)$ ranges from 0.3 to 0.7. An interpretation is that the IO field contains as much kinetic energy in the water column as what the bottom energy conversion inputs in the domain during 30 to 70% of an inertial period. Furthermore, IO amplitude and TKE dissipation rate amplitude seem to have similar parameter dependency, as the non-dimensional IO amplitude grows with the non-dimensional TKE dissipation rate. All in all, this figure does not make any direct link between IO amplitude and TKE dissipation rate amplitude, although it does point out strong similarities between the two.

This chapter presented some features of the simulations, and suggests a link between IOs and TKE dissipation rate. We have shown that, after several inertial periods, the IOs and TKE dissipation rate reach a quasi-steady state. Once this quasi-steady state is reached, about 10 to 30% of the internal lee wave energy is dissipated in the water column. One may wonder about the role IOs could play in the magnitude and distribution of turbulent kinetic energy dissipation rate. This led Nikurashin and Ferrari (2010) to propose a mechanism involving IOs in the prediction of TKE dissipation rates. Their mechanism accounted for the IO retroaction of the ILW emission, leading to a modification of the energy input in the ILW field, which lead to a modification of the TKE dissipation rate. However, their theoretical work was based on a parametric study, and was limited to the behavior of the fields above the topography. In this work, we shall attempt to gather insight on the phenomenons occuring *within* the water column. The next chapter extends their asymptotic theory in including the vertical dependency with the aim of predicting where IOs grow and inferring a vertical length scale below which dissipation occurs.

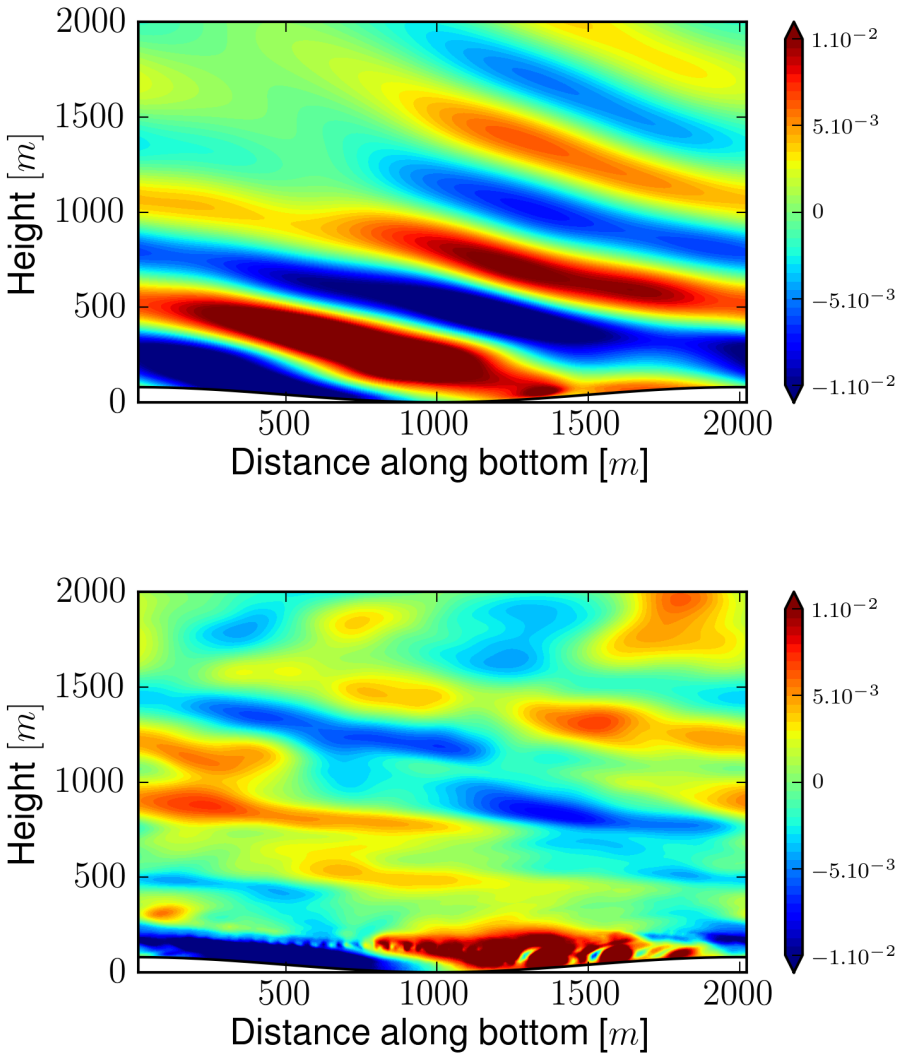

Figure 2.2 – *Snapshots of the vertical velocity for experiment $H_{40}L_2$: (top) after one inertial period; (bottom) after 7 inertial periods. The same colorbar is used for the two panels, but the maximum value is about three times higher in (b) than in (a). The top frame shows a quasi-linear regime, where internal lee waves can clearly be seen to radiate from the topography upwards. The bottom frame shows a strongly non-linear regime, with turbulent behavior near the bottom.*

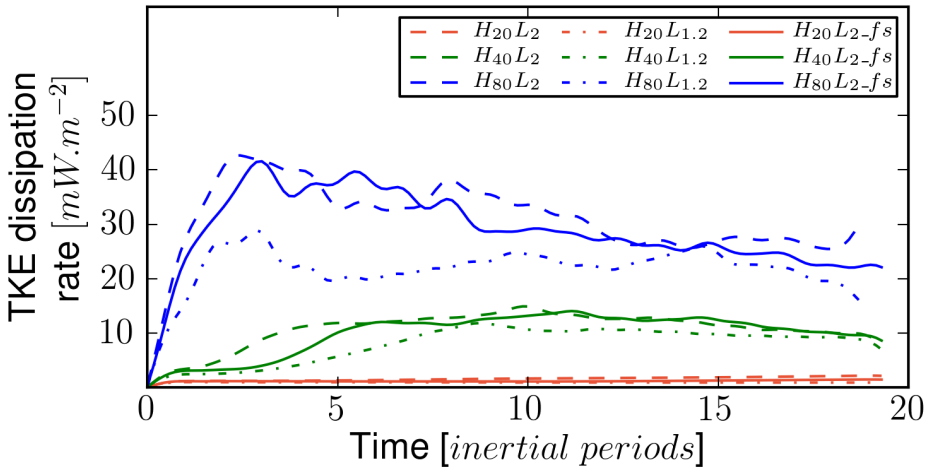

Figure 2.3 – *Temporal evolution of the turbulent kinetic energy dissipation rate for all simulations, in inertial periods. The TKE dissipation is integrated over the bottom 2000 m.*

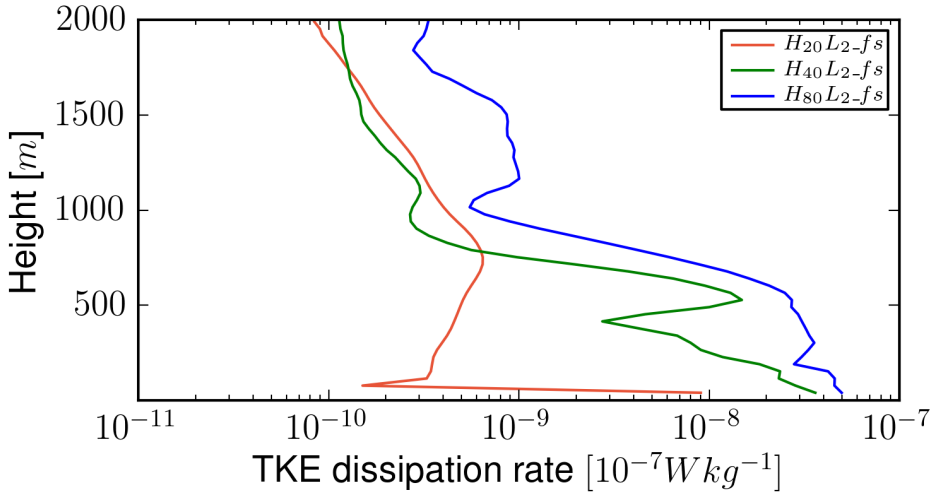

Figure 2.4 – *Vertical structure of the turbulent kinetic energy dissipation rate for the L_2_fs simulations. TKE dissipation is computed by interpolating the $\sigma-$coordinate field to $z-$coordinates and then averaged from* 12 *to* 15 *inertial periods. Note the logarithmic scale on the x-axis.*

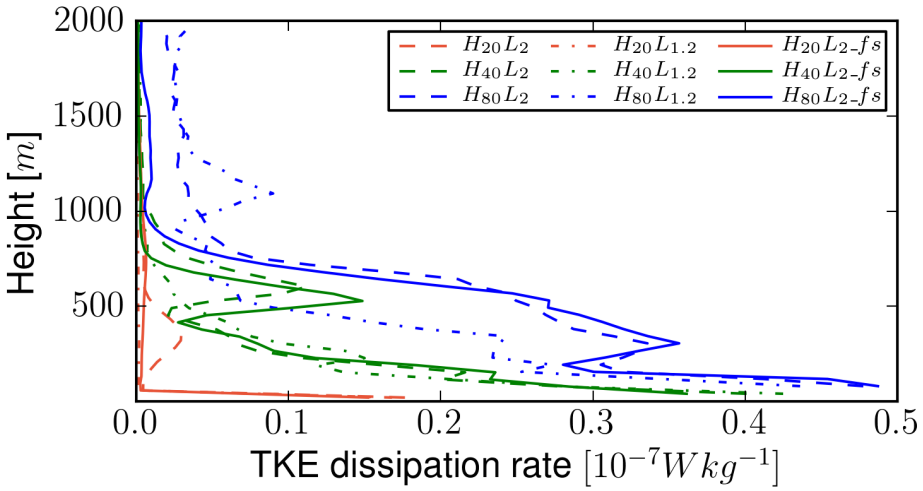

Figure 2.5 – *Vertical structure of the turbulent kinetic energy dissipation rate. For all the simulations, the TKE dissipation rate is averaged from* 12 *to* 15 *inertial periods.*

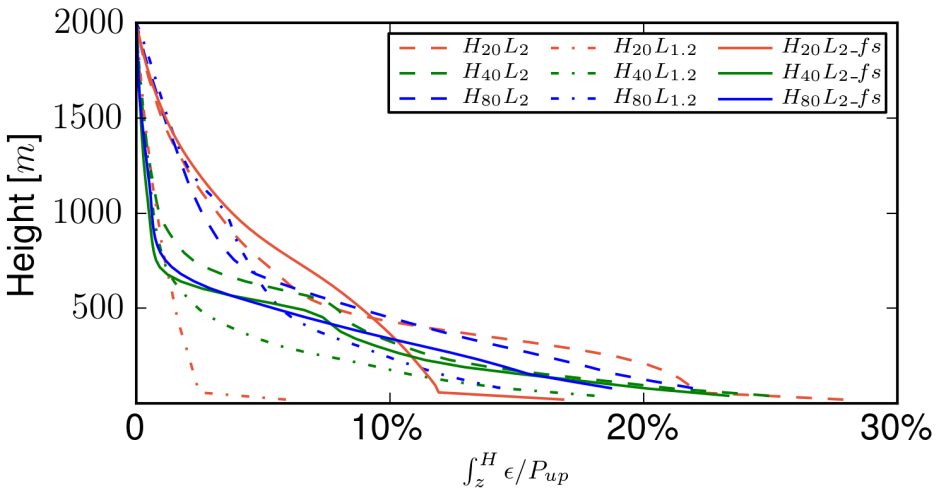

Figure 2.6 – $\int_z^H \mathcal{E} \partial z$ *normalized by the energy radiated at topography for all simulations in [m]. This represents the proportion of the energy converted from the mean flow to the internal wave field that is dissipated under a given height.*

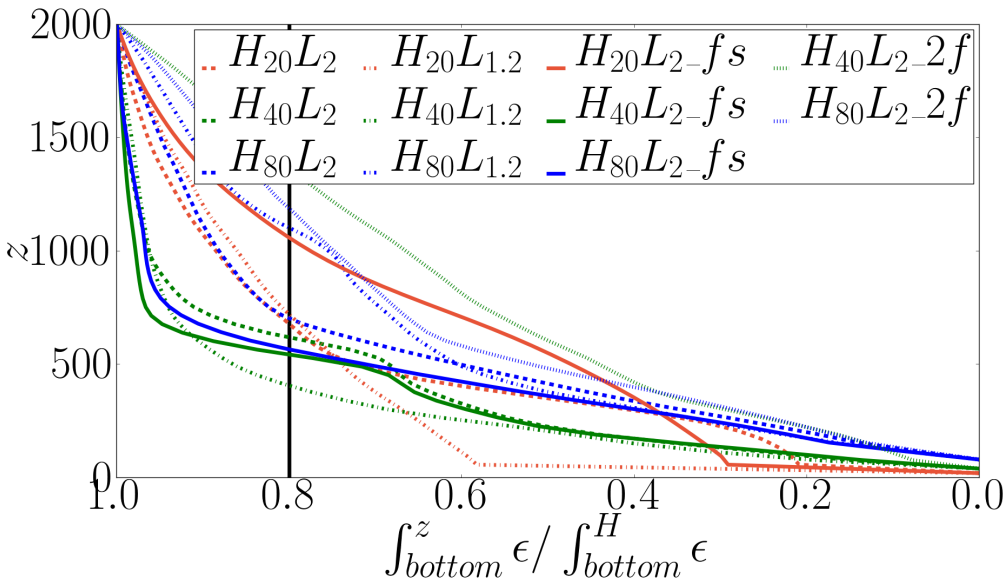

Figure 2.7 – $\int_z^H \mathcal{E}\partial z$ *normalized by* $\int_0^{2000} \mathcal{E}\partial z$ *for all simulations in [m]. This represents the proportion of the total TKE dissipation rate that is dissipated under a given height.*

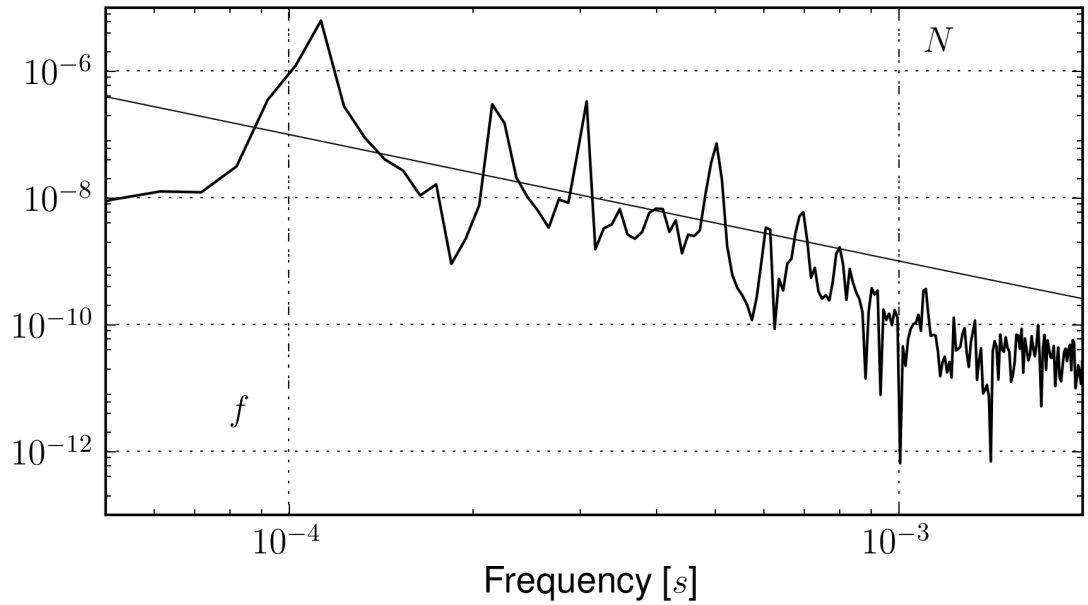

Figure 2.8 – *Variance preserving power spectrum of w for experiment* $H_{20}L_2$*, near 600 m above the topography, computed in a frame moving with the geostrophic velocity* U_G*. When the curve has a larger value than the dashed line, it departs significantly from red noise at 99% level. The inertial and Brunt Väisälä frequency are indicated with a dashed-dotted line.*

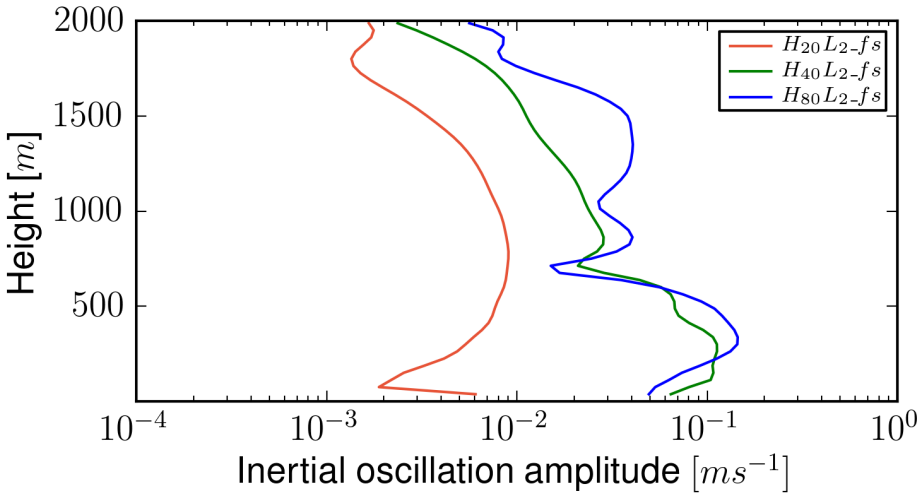

Figure 2.9 – *Vertical structure of the amplitude of inertial oscillations for the L_2_fs simulations. Note the logarithmic scale on the x-axis.*

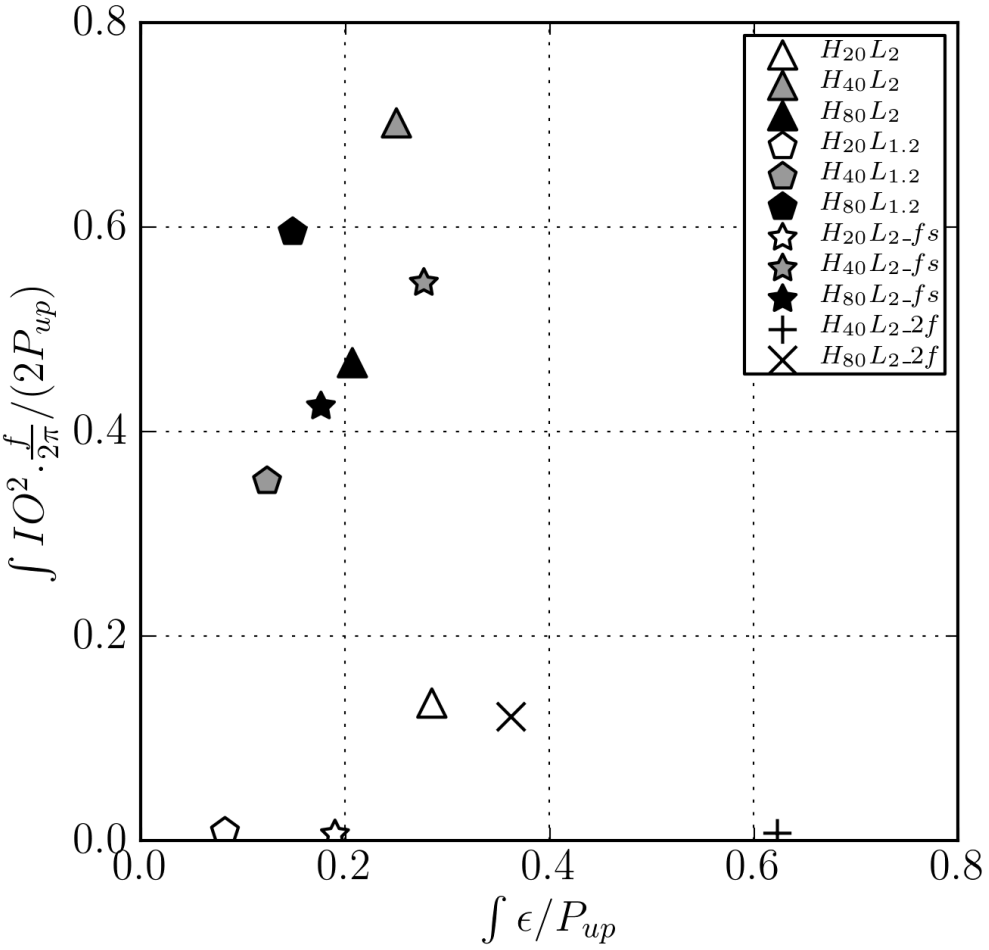

Figure 2.10 – *Scatter plot of the IO kinetic energy versus the TKE dissipation integrated over the domain. TKE dissipation is scaled by the bottom conversion rate. IO kinetic energy is normalized by the bottom conversion rate divided by an inertial period. Cases with little IO growth are shown with empty markers, the other with grey or black markers.*

3 Attempting to predict inertial oscillation amplitude: an approach following Nikurashin and Ferrari 2010

The goal of this chapter is to develop a theoretical framework to investigate the interaction between inertial oscillations and internal lee waves, leading to TKE dissipation. To do so we derive a set of equations describing the state of the medium when an inertial oscillation - internal lee wave feedback is acting. The starting point of this theoretical work is the paper by Nikurashin and Ferrari (2010). We then look at the validity of the theory in light of the numerical simulations.

3.1 The asymptotic theory

3.1.1 Assumptions of the theory

Quite a few assumptions are needed in order to develop this theoretical framework.

- The non-hydrostatic Boussinesq approximation is used (Eq. 2.2a, 2.2b, 2.3).
- The internal wave amplitude $\epsilon \sim Nh_T/U_G$ is supposed to be small so as to keep the whole theory weakly non-linear, since large non-linearities are usually analytically untractable. This is mostly valid for the smallest amplitude cases ($h_T = 20$ m), and can be extended to the medium ($h_T = 40$m) amplitude cases.

- The IO amplitude (through the parameter $\beta = U_I k_T / f$) is supposed to be small in order to get a simple analytical expression of the growth rate, which is a valid hypothesis for the beginning of all simulations, since the IO field starts from rest. Moreover, the parameter β is supposed to be independent of ϵ.
- The internal lee wave frequency $U_G k_T$ is supposed to be such that: $f << U_G k_T << N$. This allows simplifications in the theoretical development, although it is far from being valid in our numerical simulations (for the reference cases, $U_G k_T / f = \pi$ and $N / U_G k_T = 10/\pi$). While these assumptions are more or less physically plausible, others were made for mathematical tractability and lack physical meaning:
- Weak Rayleigh (linear) dissipation was used rather than Laplacian to represent the damping of the waves during their propagation to keep the problem analytically tractable (Goldstein 1980). Dissipation being essential for the mechanism described here, this hypothesis may have a very strong impact on the conclusions derived in the calculation.
- The internal wave field was computed as if it propagates without interactions after being emitted at the topography. This entails that, although the interaction of different waves can give rise to IOs, the expression for these waves is not impacted by the interaction, nor by the existence of IOs (except in the generation mechanism).

3.1.2 Keeping the vertical coordinate

We follow Nikurashin and Ferrari (2010), although we slightly depart from their paper by keeping track of the vertical coordinate.

The complete equations of motion and bottom boundary condition in the

fluid write:

$$\boldsymbol{u}_t + (\boldsymbol{u}.\boldsymbol{\nabla}_H)\cdot\boldsymbol{u} + w\boldsymbol{u}_z + f\boldsymbol{e}_z \wedge \boldsymbol{u} = -\boldsymbol{\nabla}_H p + \mathcal{D}_m(\boldsymbol{u}) \tag{3.1a}$$

$$w_t + (\boldsymbol{u}.\boldsymbol{\nabla}_H)w + ww_z = -p_z + b + \mathcal{D}_m(w) \tag{3.1b}$$

$$b_t + (\boldsymbol{u}.\boldsymbol{\nabla}_H)b + wb_z + wN^2 = \mathcal{D}_b(b) \tag{3.1c}$$

$$\boldsymbol{\nabla}_H \cdot \boldsymbol{u} + w_z = 0 \tag{3.1d}$$

where $\boldsymbol{u} = (u, v)$ and w are, respectively, the horizontal and vertical velocities, p the pressure deviation about hydrostatic equilibrium, $b = -g\frac{\rho-\rho_0}{\rho_0}$ the buoyancy, f the Coriolis frequency, N the Brunt-Väisälä frequency and ρ_0 the reference density. $\mathcal{D}_{m,b}$ is a representation of the viscosity and dissipation.

Let us expand the fields and the coordinates in a small parameter representative of the ILW field amplitude: $\epsilon = \frac{Nh_T}{U_G} << 1$:

$$\boldsymbol{u} = \boldsymbol{u}_G + \boldsymbol{u}_I + \sum_{i=1}^{\infty} \epsilon^i \boldsymbol{u}^{(i)} \tag{3.2a}$$

$$(w, b, p) = \sum_{i=0}^{\infty} \epsilon^i (w^{(i)}, b^{(i)}, p^{(i)}) \tag{3.2b}$$

$$\boldsymbol{x} = \sum_{i=0}^{\infty} \epsilon^{-i} \boldsymbol{X}^{(i)} \tag{3.2c}$$

$$t = \sum_{i=0}^{\infty} \epsilon^{-i} T^{(i)} \tag{3.2d}$$

where $[T^{(i)}, \boldsymbol{X}^{(i)}]$ are slower and shorter scales of the problem the larger the index i is. The fastest scales $(T^{(0)}, \boldsymbol{X}^{(0)})$ are the scales of the internal wave field.

It is noteworthy that although the IOs are initially of infinitesimal amplitude, their appearing at order 0 of the development in ϵ is equivalent to stating that their amplitude is independent on ϵ. It does not necessarily imply that they have an amplitude comparable to $\boldsymbol{u}_G$.

The development being identical to that of Nikurashin and Ferrari (2010), I do not detail it here, but in Appendix A.2. The zero order equations represent the bulk flow, and only take the constant flow and inertial oscillations into account.

The ILW are antisymmetric and periodic perturbations, and since they have a trivial horizontal mean they do not show up at this order. However, they do have a net effect on the Eulerian mean since they can force the IOs through $-\partial_{Z^{(1)}}\overline{\boldsymbol{u}^{(1)}w^{(1)}}^{x}$. The third order terms imply that U_I is forced on the slow time scales $T^{(3)}$ by the internal wave flux divergence: More precisely,

$$\boldsymbol{u}^I_{T^{(3)}} = -\partial_{Z^{(1)}}\overline{\boldsymbol{u}^{(1)}w^{(1)}}^{x} \tag{3.3}$$

Taking the complex notation $\mathcal{V} = u + iv$, and knowing from the order 0 equations that the IOs oscillate at frequency f, hence $\mathcal{V}^I = U_I e^{-if(t-t_1)}$, we obtain the slow time scale evolution of the IO field:

$$\partial_{T^{(3)}}U_I = \Re\big(\aleph\big)U_I = \Gamma U_I \tag{3.4a}$$

$$\partial_{T^{(3)}}t_1 = \Im\big(\frac{\aleph}{f}\big) \quad = \Lambda \tag{3.4b}$$

Where $\aleph(\beta, z) = -\frac{k_T}{f\beta}\partial_{Z^{(1)}}\overline{\mathcal{V}^{(1)}w^{(1)}}^{x}\big|_{\omega=-f(t-t_0)}e^{-if(t_1-t_0)}$ contains the amplitude (Γ) and phase (Λ) of the growth rate of the inertial oscillations, and depends both on z and U_I (through the intermediary of β). ft_0 is the original phase of the ILWs. We notice that at lowest order in β the IOs are expected to have an exponential growth, and their phase evolves linearly. Hence it is a good approximation to consider the phase of the IOs as constant over the time of growth of their amplitude.

As shown in figure 3.1, in the first moments of the instability process, the IOs appear to be in phase with the ILWs:

$$f(t_1 - t_0) = 0 \tag{3.5}$$

We now derive the ILW components ($u^{(1)}$,$v^{(1)}$,$w^{(1)}$) from usual wave calculations (Bell 1975):

$$\mathcal{D}^{(n)}_m\big(\boldsymbol{u}^{(n)}\big) = -\lambda\boldsymbol{u}^{(n)} \tag{3.6a}$$

$$\mathcal{D}^{(n)}_b\big(b^{(n)}\big) = -\lambda b^{(n)} \tag{3.6b}$$

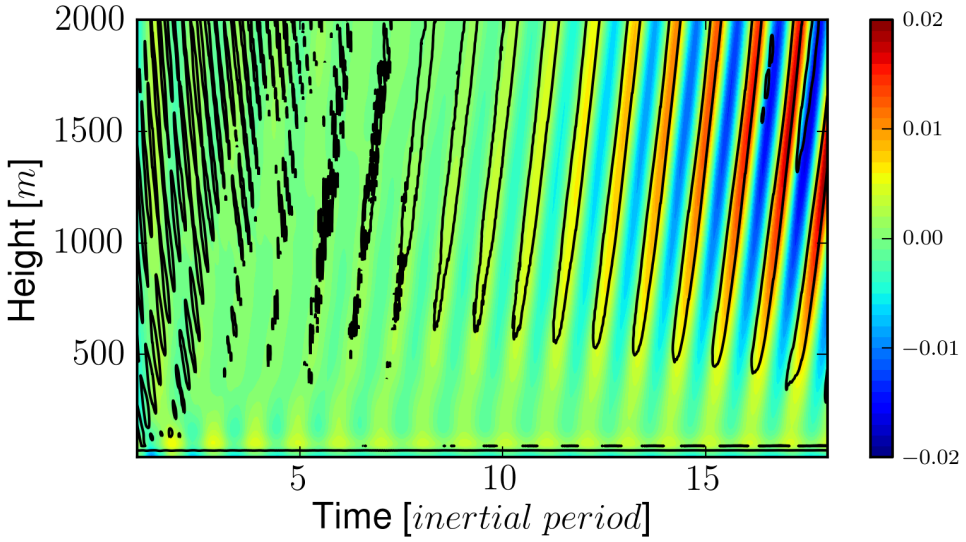

Figure 3.1 – *Time-height diagram of the horizontal velocity of the inertial oscillations (colors) and of the momentum deposit of the internal lee wave (contours) for experiment $H_{20}L_{20}\_fs$. The contours are hatched when $-\partial_z\overline{u'w'} > 0$.*

It entails that the fields can be written as:

$$u^{(1)}(t,\zeta,z) = -h_T \sum_n \sigma_n J_n(\beta) \frac{m_n}{k_T} \qquad \Im\left(e^{i\theta_n(t,\zeta,z)}\right) \tag{3.7a}$$

$$v^{(1)}(t,\zeta,z) = -h_T \sum_n \sigma_n J_n(\beta) \frac{m_n}{k_T} \frac{f}{\sigma_n - i\lambda} \Im\left(e^{i\theta_n(t,\zeta,z)}\right) \tag{3.7b}$$

$$w^{(1)}(t,\zeta,z) = -h_T \sum_n \sigma_n J_n(\beta) \qquad \Im\left(e^{i\theta_n(t,\zeta,z)}\right) \tag{3.7c}$$

where the fields are computed in the frame moving at the geostrophic velocity $\zeta = x - \int_{t_0}^{t} u_G dt'$, and the oscillatory propagation holds $\theta_n(t,\zeta,z) = k_T\zeta + m_n z + \sigma_n(t-t_0)$. For a given integer n, $\sigma_n = nf + U_G k_T$ in the n-th harmonic of the frequency f, Doppler shifted by $u_G k_T$, $m_n^2 = k_T^2 \frac{N^2}{(\sigma_n - i\lambda)^2 - f^2}$ is its complex vertical wavenumber where the imaginary part represents the damping with height due to dissipation. J_n is the n-th Bessel function of the first kind.

Note that the sum only holds for integers n such that the internal wave frequency lies within the internal wave range: $|f| < \sigma_n < N$, or $\frac{|f| - U_G k_T}{|f|} < n < \frac{N - U_G k_T}{|f|}$.

Inserting these expressions into the definition of Γ, and under the assumption

that $\frac{|f|}{U_G k_T}$, $\frac{\lambda}{U_G k_T}$ and β are much smaller that one ($= o(1)$) one gets:

$$\Gamma = \Gamma_0.\big(\cos(\phi z) + \frac{4.\lambda^2 - f^2}{4\lambda f}\sin(\phi z)\big) + \mathcal{O}(\frac{f^2}{U_G^2 k_T^2}, \frac{\lambda^2}{U_G^2 k_T^2}, \beta) \qquad \text{, with} \quad (3.8a)$$

$$\Gamma_0 = f^2 \frac{\epsilon^2 \lambda}{U_G^2 k_T^2}(1 + 4\frac{f^2}{U_G^2 k_T^2} - 6\frac{\lambda^2}{U_G^2 k_T^2}) \quad (3.8b)$$

and $\phi \sim -\frac{N|f|}{U_G^2 k_T}$,

Nikurashin and Ferrari (2010) found $\lambda = 5.10^{-5} s^{-1}$ from a least square fit of simulations, with $f = 10^{-4} s^{-1}$. This estimate entails $4\lambda^2 - f^2 \sim 0$, hence the growth rate has a typical vertical scale of

$$\phi h_c = -\frac{\pi}{2} \quad (3.9a)$$

$$\Rightarrow h_c \sim \frac{\pi U_G^2 k_T}{2N|f|} \quad (3.9b)$$

More generally,

$$h_c = -\frac{U_G^2 k_T}{N|f|}\arctan(\frac{4\lambda f}{4.\lambda^2 - f^2}) \quad (3.10a)$$

where the first negative solution is taken for the arctangent.

Since λ is a non-physical parameter which is difficult to estimate, this derivation may not be applicable to the real ocean. However, the dependency on the other parameters (U_G, k_T, f, N) can still be estimated from the numerical simulations.

Several conclusions can be inferred from this calculation.

- Viscous effects are fundamental in this mechanism, since the amplitude of Γ_0 is proportional to the amount of dissipation λ.
- This mechanism is also fundamentally nonlinear, as can be seen through the ϵ^2 dependency of the growth rate.
- The dependency of the interaction mechanism on the amplitude of the inertial oscillations is only seen through the emission process of the internal lee waves (via the prefactor $J_n(\beta)$). No feedback from the IOs to the ILWs in the water column is described.

- Since the growth rate is positive near topography and becomes negative above h_c, the IOs are expected to have a vertical extension of h_c above topography.
- Only the bulk envelop of the IOs can be described here. Little can be inferred on their vertical wavenumber.

3.2 Comparison with the simulations

We will here analyze the data from the numerical simulations to investigate whether the asymptotic theory can provide any significant insight into the physics at play.

3.2.1 Growth rate of the inertial oscillations

The amplitude of the inertial oscillations was computed through the water column at all times for each simulation, and were described in the previous chapter for the reference cases. Figure 3.2 shows the time evolution of the inertial oscillations taken at a height of 100 m above topography for all the simulations. The spin up of the simulation, during which the mean flow grows from 0 to U_G and IO are explicitly damped, is not shown. Three typical behaviors can be observed. For cases with $h_T = 20$ m, the IOs do not significantly grow. This is because the wave amplitude ϵ is much smaller than 1 in those runs, and $\Gamma \sim \epsilon^2$. Cases with $h_T = 40$ or 80 m show a much more robust growth, as the wave amplitude is higher. After a few inertial periods, the IOs in these simulations reach a statistically steady state, or saturation. For similar settings, it appears that as h_T or k_T increases, so does the amplitude of IOs at saturation. Finally, for simulations with twice the inertial frequency, where $f > U_G k_T - f$, the IOs do not significantly depart from noise (not shown).

Figure 3.3 is the same as Fig. 3.2 except for the time axis, which is made non dimensional using Γ_0 defined by Eq. 3.8b, with $\lambda = 1.10^{-4}$ s^{-1}. For $h_T \geq 40$ m, this scaling appears to be appropriate as the different curves approximately

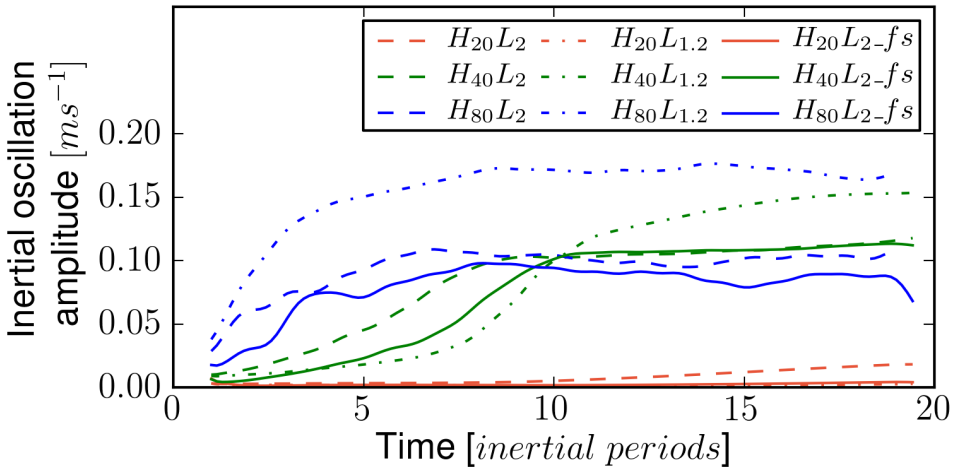

Figure 3.2 – *Temporal evolution of the amplitude of inertial oscillations at* 100 *m, in inertial periods. The IO signal was processed through a Lanczos low-pass filter at cutoff frequency* f*. The spin up of the simulation, during which the mean flow grows from* 0 *to* U_G *and IO are explicitly damped, is not shown.*

collapse during the IO growth. This choice of λ is poorly constrained and lacks physical insight, it is simply chosen here to fit the data at best, and to get insight on the functional dependency of Γ on the other parameters of the problem.

To get a more precise estimate of the rate at which the IOs grow, an exponential fit of the curves after spin-up was made. This gives quantitative estimates of Γ, noted $\Gamma_{simulations}$.

Figure 3.4 is a scatter plot representing the theoretical and simulated growth rates. The IOs seem to grow over the predicted time scale, with a saturation occurring for large topographic amplitude. This does not come as a surprise, since λ was chosen so as to correctly fit the numerical growth rate of the IOs. Indeed, computing the asymptotic theory with a Laplacian viscosity proved unfeasible. Nonetheless, as an alternate test of the theory, we proceeded in estimating the vertical profile of the IOs since h_c is independent on λ at lowest order.

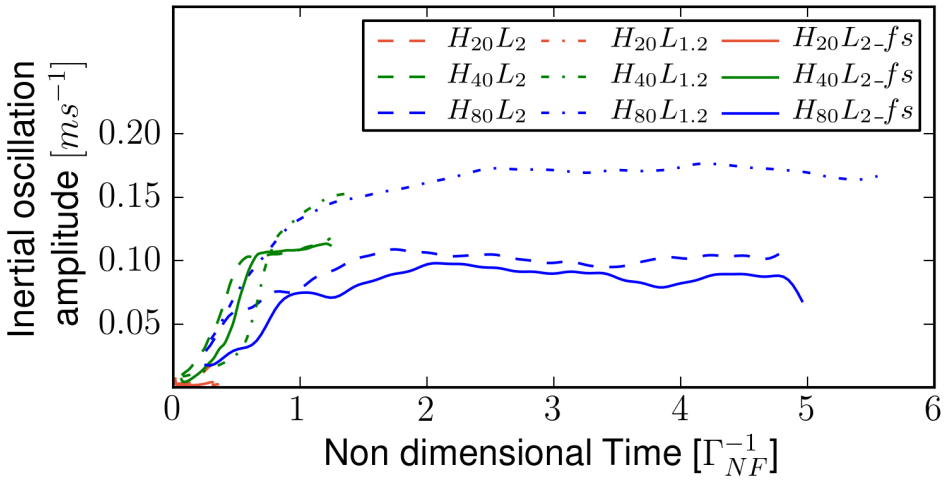

Figure 3.3 – *Time evolution of the IOs, as in figure 3.2, except that time is normalized by the growth rate from the asymptotic theory.*

3.2.2 Vertical extent of the inertial oscillations

Characterizing the field profiles requires describing their amplitude, as was done above, and their vertical dependency. We here explore the validity of the second information the asymptotic theory provides, which is the height under which the IOs are supposed to be significant. Both the IO and TKE dissipation rate profiles were computed by averaging the field amplitudes from 12 to 15 inertial periods. This calculation is quite accurate for simulations that saturate, but less valid for non saturating situations such as when the amplitude is small. Figure 3.5 shows the profile of the inertial oscillations amplitude for all the simulations.

The IOs all appear to be confined within 1000 m above the bottom, with some variations between simulations. The IOs display a growing behavior right above topography, up to roughly 500 m, decrease between 500 and 1000 m, and remain small for the rest of the water column.

To obtain a quantitative measurement of the vertical scale of the IOs and TKE dissipation rate, we chose an analytical profile $g(z_c, z_w, g_0, z)$ so as to optimize its correlation with a given profile, averaged from 12 to 15 inertial periods. The

analytical profile consists of a piecewise linear function:

$$g(z) = \begin{cases} g_0 + (1 - g_0)\frac{z}{z_c - z_w} & \text{if } z \in [0, z_c - z_w] \\ -\frac{z - z_c}{z_w} & \text{if } z \in [z_c - z_w, z_c] \\ 0 & \text{if } z \geq z_c \end{cases} \tag{3.11}$$

where z_c is the *effective height* above topography under which the field is confined, z_w and g_0 are adjustment parameters. Figure 3.6 shows the TKE dissipation (a) and IO amplitude (b) profiles averaged from 12 to 15 inertial periods in the simulation $H_{40}L_{2}\_fs$ and the corresponding analytical profiles. From this computation one gets (z_c, z_w, f_0) for both fields at saturation for each numerical simulation.

Figure 3.7 shows a scatter plot of the theoretical effective height predicted for the IOs by the asymptotic theory, and that diagnosed from the simulations. As in Chapter 2, simulations whose parameter range leads to a strong positive growth rate are shown with grey or black markers, the others with empty markers. Although the theory comes up with the tight orders of magnitude, the parametric dependency of the effective height does not seem to be correctly represented.

Figure 3.8 is a scatter plot of the effective height of the IOs versus that of the TKE dissipation rate for all the simulations. Little can be said for empty markers, that have such low amplitudes in one or both fields that the uncertainty of the effective height can be over 500 m. By contrast, the other simulations are well defined, and show that whereas the IO field effective height seems to be rather independent of the parameter range, no clear conclusion can be inferred for the TKE dissipation rate effective height. It does appear, however, that the TKE dissipation systematically occurs within the depth with strong inertial oscillations, and below 1000 m.

Together with the description of the amplitude of the IOs, this implies that the asymptotic theory as presently derived relies on a major approximation to represent the physics at play. It makes use of an arbitrary, non-physical parameter (λ), and even when investigating another prediction (namely h_c), fails at

reproducing the simulations. Our sensitivity study shows that simulations with strong IOs are systematically associated with strong TKE dissipation. However, obtaining the TKE dissipation rate vertical scale does not seem to be straightforward, and would require further work. This lead us to develop a second theoretical framework, relying on the Resonant Interaction Theory (RIT).

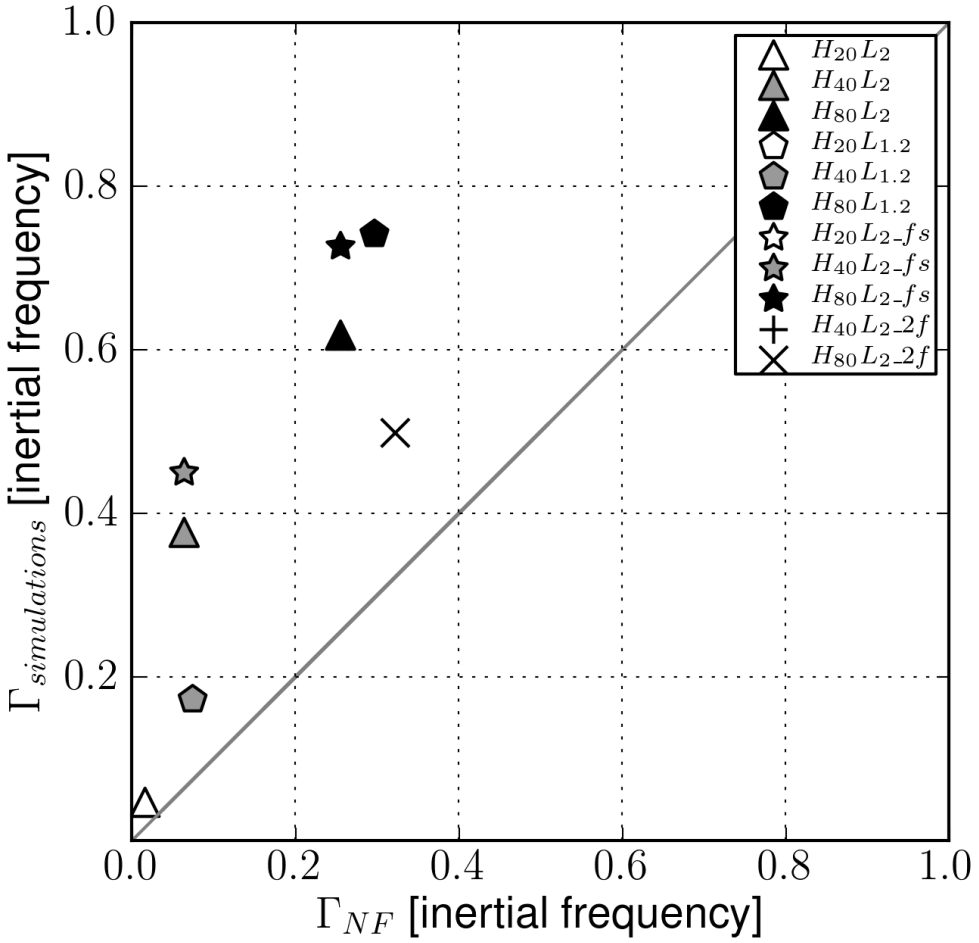

Figure 3.4 – *Comparison of the IO growth rate between that diagnosed from the simulations and that predicted by the asymptotic theory.*

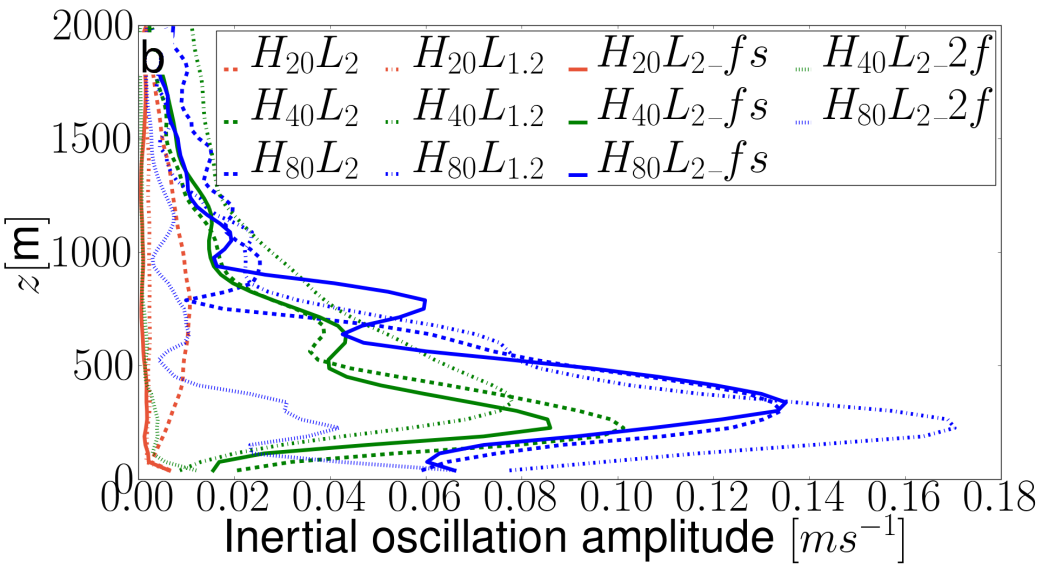

Figure 3.5 – *Vertical structure of the inertial oscillation amplitude. For all the simulations, the IOs are averaged from* 12 *to* 15 *inertial periods.*

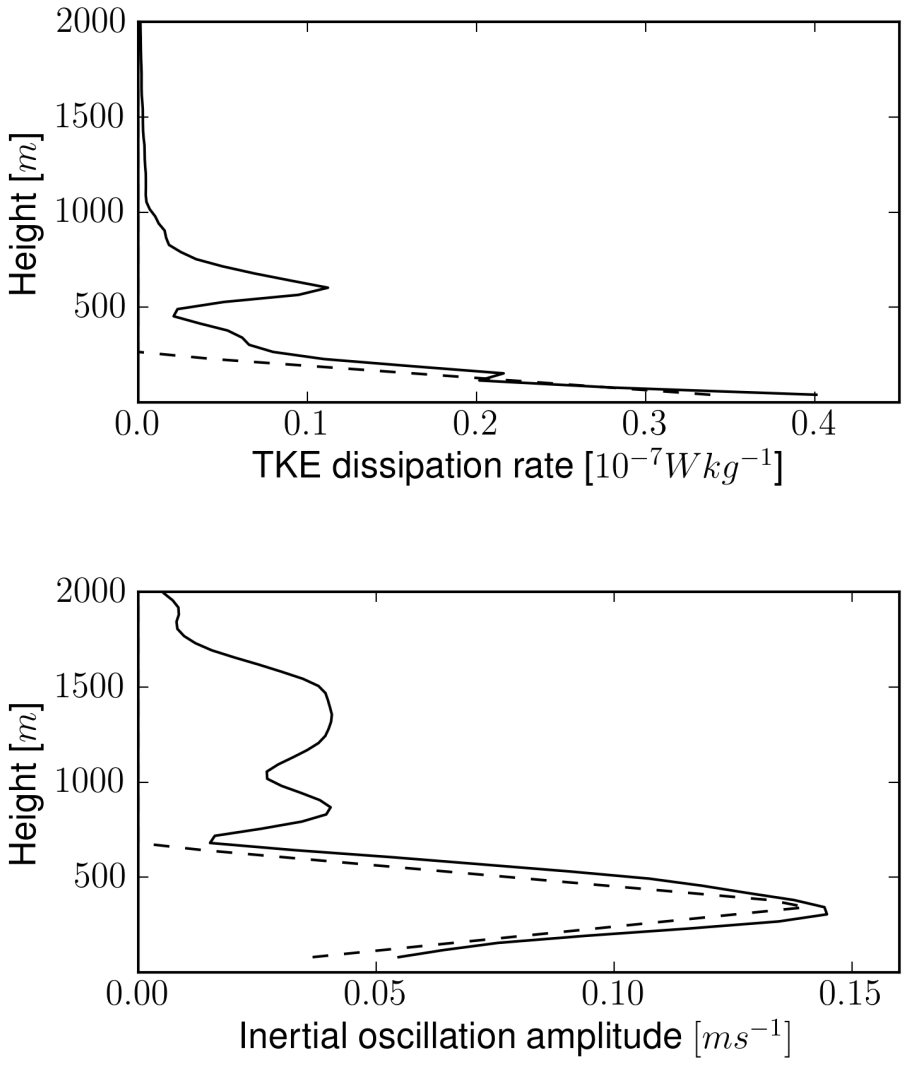

Figure 3.6 – *Analytical and simulated profiles for the TKE dissipation rate (a) and IO amplitude (b). Example of the analytical (in dotted line) to simulated (in full line) profile comparison for simulation* $H_{40}L_{20}\_fs$. *The simulation profile is averaged from* 12 *to* 15 *inertial periods.*

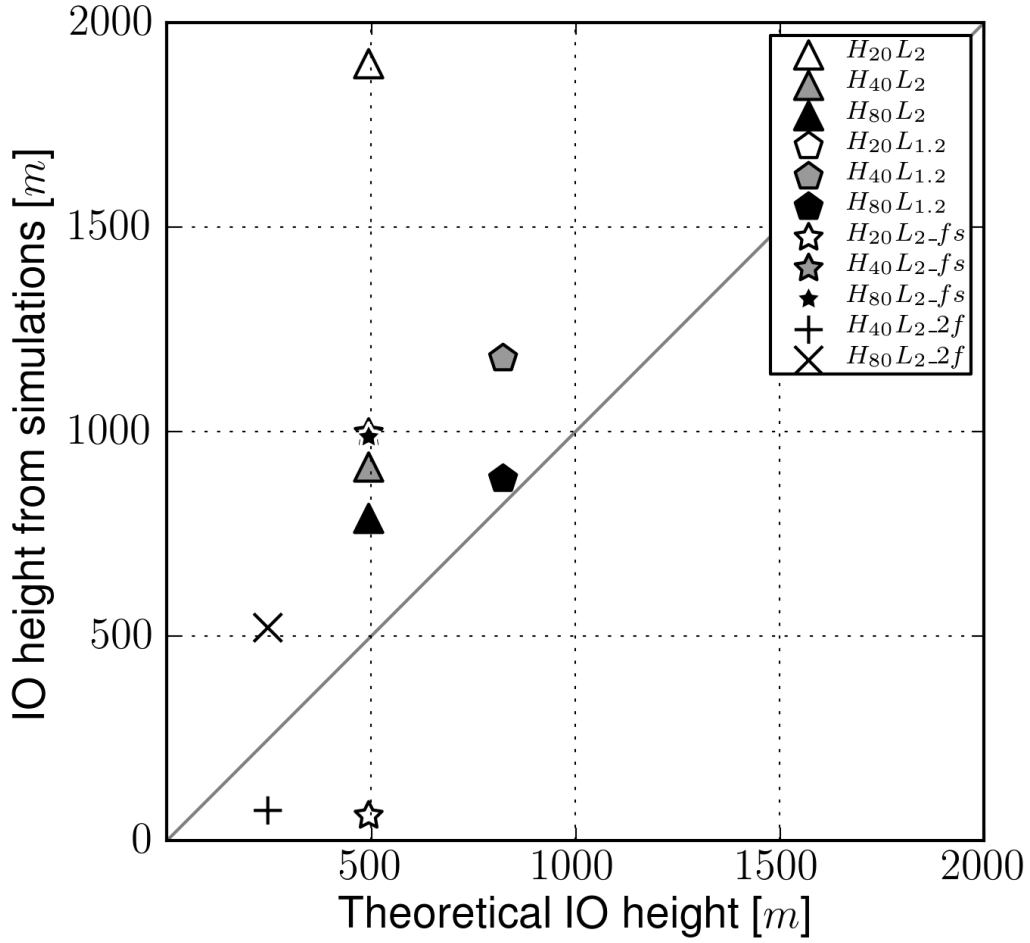

Figure 3.7 – *Comparison of the IO vertical extent between that diagnosed from the simulations and that predicted by the asymptotic theory using Eq. 3.11*

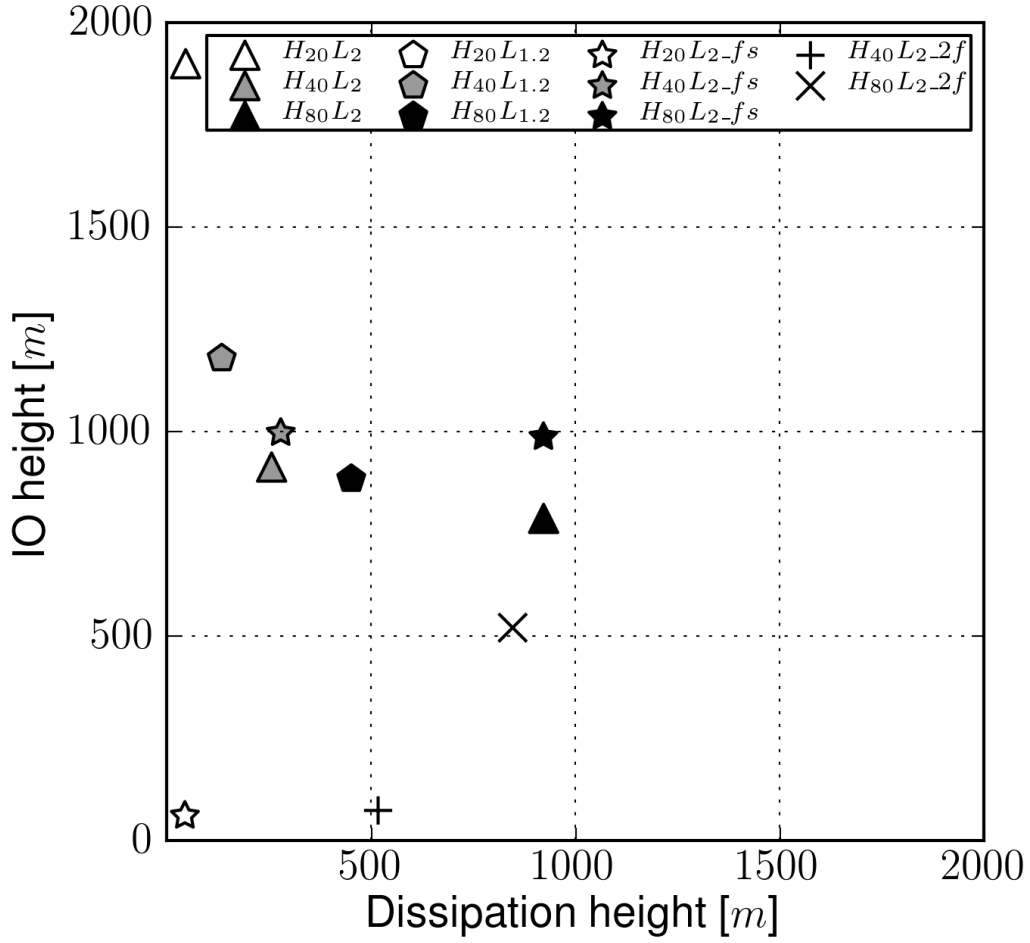

Figure 3.8 – *Scatter-plot of the diagnosed* effective height *for the IO amplitude and TKE dissipation rate, diagnosed from the simulations.*

Attempting to predict inertial oscillation amplitude: on the importance of resonant triad interactions

4

Since the asymptotic method described in the previous chapter relied on a major approximation to reproduce the physics at play, we chose to turn instead toward a more robust framework, although it bears less information in the physical space: the resonant interaction theory (RIT, Phillips 1967). This chapter aims at applying the RIT to our problem and comparing its conclusions with our numerical simulations, in the hope that it will fare better than the asymptotic theory.

4.1 The resonant interaction theory

4.1.1 Pros and cons of the underlying hypotheses

As we shall see in this section, the resonant interaction theory focuses on weakly non-linear interactions between internal waves. So as to have a general view of the applicability of this development, we discuss here the hypotheses made in the derivation of the RIT.

The derivation starts from the two-dimensional, Boussinesq equations, and invokes scaling arguments to neglect some terms.

- The Rossby number ($Ro = U/fL$ where L is a typical horizontal scale and U a typical horizontal velocity) is supposed very large ($Ro >> 1$), that is

to say the phenomena considered here are wave-like motions that occur on scale smaller than the Rossby radius.

- The dimensionless amplitude of the wave is the Froude number, defined here as $Fr = U/NL$, which is supposed very small ($Fr << 1$). U and L are characteristic velocity and length of the wave and N is the Brunt-Väisälä frequency.
- Finally, for deriving the amplitude evolution equations, the internal waves amplitude is supposed to be dominated by a single wave (still of small amplitude), the other ones being considered as perturbations.

4.1.2 Derivation

In this section, we derive a theoretical framework stating that the emergence of inertial oscillations results from resonant triad interactions among internal waves. It relies on the resonant interaction theory (RIT) (Phillips 1967). It can be shown from this theory that significant energy exchanges among a wave triad can only occur if the wave-vectors and frequencies satisfy specific relations. Under such conditions, the wave triad is said to be resonant. In what follows, we provide an overview of the resonant interaction theory, where dissipation is neglected. The full detailed calculations can be found in appendix A.1.

Deriving the resonant interaction theory

We start from the non-dimensional Boussinesq equations written in a vertical plan (Koudella and Staquet 2006):

$$\partial_t \Delta\psi + FrJ(\Delta\psi, \psi) = \frac{f}{N}\partial_z v + \partial_x \rho \tag{4.1a}$$

$$\partial_t v + FrJ(v, \psi) = -\frac{f}{N}\partial_z \psi \tag{4.1b}$$

$$\partial_t \rho + FrJ(\rho, \psi) = -\partial_x \psi \tag{4.1c}$$

where ψ is the stream-function, v is the meridional velocity and ρ the density and J is the Jacobian operator. The scaling makes use of L and U previously defined and of the time scale $T_0 \sim N^{-1}$.

We then assume that the Froude number Fr is small and consider two different time scales: $t_0 \sim N^{-1}$ is a fast time-scale and $t_1 \sim \frac{t_0}{Fr} \sim \frac{L}{U}$ is a slow time-scale. Expanding the fields around this small parameter yields:

$$t = t_0 + Frt_1 \tag{4.2a}$$

$$\psi(\boldsymbol{x}, t_0, t_1) = \psi^0(\boldsymbol{x}, t_0, t_1) + Fr\psi^1(\boldsymbol{x}, t_0, t_1) + \mathcal{O}(Fr^2) \tag{4.2b}$$

$$\rho(\boldsymbol{x}, t_0, t_1) = \rho^0(\boldsymbol{x}, t_0, t_1) + Fr\rho^1(\boldsymbol{x}, t_0, t_1) + \mathcal{O}(Fr^2) \tag{4.2c}$$

$$v(\boldsymbol{x}, t_0, t_1) = v^0(\boldsymbol{x}, t_0, t_1) + Frv^1(\boldsymbol{x}, t_0, t_1) + \mathcal{O}(Fr^2) \tag{4.2d}$$

Introducing Eq. 4.2 into Eq. 4.1 and identifying the terms with the same power of Fr leads to equations associated with each power of Fr. At order 0, one recovers the plane wave equations. In the following, we shall assume that ψ, ρ and v result from the superposition of three waves:

$$\psi^0(\boldsymbol{x}, t_0, t_1) = \sum_{j=0}^{2} A_j(t_1) e^{i\phi_j} + c.c. \tag{4.3a}$$

$$\rho^0(\boldsymbol{x}, t_0, t_1) = \sum_{j=0}^{2} \frac{k_j}{\omega_j} A_j(t_1) e^{i\phi_j} + c.c. \tag{4.3b}$$

$$v^0(\boldsymbol{x}, t_0, t_1) = \sum_{j=0}^{2} \frac{f}{N}\frac{m_j}{\omega_j} A_j(t_1) e^{i\phi_j} + c.c. \tag{4.3c}$$

where

$$\phi_j = \boldsymbol{k_j}.\boldsymbol{x} - \omega_j t_0$$

$$\boldsymbol{k_j} = k_j \boldsymbol{e}_x + m_j \boldsymbol{e}_z$$

A_j and ϕ_j refer to slowly varying amplitude and phase, respectively, of each wave, as a result of nonlinear interactions within the triad. The intrinsic frequencies ω_i are supposed to be positive without any loss of generality.

The amplitude equation of either wave is obtained by writing the equations at first order in Fr. Careful development leads to:

$$\sum_{\sigma_l=\pm1}\sum_{l=0}^{2}\sigma_l\mathcal{F}_l e^{i\sigma_l\phi_l}\frac{\partial A_l^{(\sigma_l)}}{\partial t_1}+\sum_{\substack{\sigma_n=\pm1\\ \sigma_p=\pm1}}\sum_{n=0}^{2}\sum_{p=0}^{2}\sigma_n\sigma_p\mathcal{G}_{n,p}e^{i(\sigma_n\phi_n+\sigma_p\phi_p)}A_n^{(\sigma_n)}A_p^{(\sigma_p)}=0 \tag{4.4}$$

Where $\sigma_i=\pm1$. $\mathcal{F}_l$ gathers the linear terms and $\mathcal{G}_{n,p}$ the non-linear terms:

$$\mathcal{F}_l=-2K_l^2\omega_l \tag{4.5a}$$

$$\mathcal{G}_{n,p}=(m_nk_p-m_pk_n)\left(K_p^2(\sigma_n\omega_n+\sigma_p\omega_p)+\frac{k_p}{\omega_p}(\sigma_nk_n+\sigma_pk_p)+(\frac{f}{N})^2\frac{m_p}{\omega_p}(\sigma_nm_n+\sigma_pm_p)\right) \tag{4.5b}$$

where $K=|\boldsymbol{k}|$, $A_j^{(1)}=A_j$ and $A_j^{(-1)}=A_j^*$.

From this equation, it follows that for resonant interactions to occur, one of the wave combinations needs to satisfy:

$$\forall\{l,n,p\}\in\{0,1,2\}^3\backslash l\neq n\neq p,\quad \exists(\sigma_l,\sigma_n,\sigma_p)\in\{-1,1\}^3\backslash\sigma_l\phi_l=\sigma_n\phi_n+\sigma_p\phi_p \tag{4.6}$$

We choose the convention $\omega_j>0$ without any loss of information. The resonant condition 4.6 can be written as:

$$\forall\{l,n,p\}\in\{0,1,2\}^3\backslash l\neq n\neq p,\quad \exists(\sigma_l,\sigma_n,\sigma_p)\in\{-1,1\}^3\backslash$$

$$\sigma_l\omega_l=\sigma_n\omega_n+\sigma_p\omega_p \tag{4.7a}$$

$$\sigma_l\boldsymbol{k}_l=\sigma_n\boldsymbol{k}_n+\sigma_p\boldsymbol{k}_p \tag{4.7b}$$

Introducing the resonant condition 4.7 into 4.5b holds, after some development:

$$\frac{\partial A_l^{(\sigma_l)}}{\partial t_1}=\sigma_n\sigma_pA_n^{(\sigma_n)}A_p^{(\sigma_p)}\frac{(m_nk_p-m_pk_n)}{2K_l^2\omega_l}\left((K_p^2-K_n^2)\omega_l+(\frac{k_p}{\omega_p}-\frac{k_n}{\omega_n})k_l+(\frac{f}{N})^2(\frac{m_p}{\omega_p}-\frac{m_n}{\omega_n})m_l\right) \tag{4.8}$$

Let us rewrite the two main results from this section in a more general way (in equations 4.7, $\sigma_l \to -\sigma_l$ without any loss of generality). If there exists a sign combination (σ_l, σ_n, σ_p) such that:

$$\sigma_l \omega_l + \sigma_n \omega_n + \sigma_p \omega_p = 0 \tag{4.9a}$$

$$\sigma_l \boldsymbol{k}_l + \sigma_n \boldsymbol{k}_n + \sigma_p \boldsymbol{k}_p = 0 \tag{4.9b}$$

then the final amplitude evolution equation holds:

$$\begin{aligned}\frac{\partial A_l^{(\sigma_l)}}{\partial t_1} =& \sigma_n \sigma_p A_n^{(-\sigma_n)} A_p^{(-\sigma_p)} \frac{(m_n k_p - m_p k_n)}{2K_l^2 \omega_l} \\ & \left((K_p^2 - K_n^2)\omega_l + (\frac{k_p}{\omega_p} - \frac{k_n}{\omega_n})k_l + (\frac{f}{N})^2 (\frac{m_p}{\omega_p} - \frac{m_n}{\omega_n}) m_l \right)\end{aligned} \tag{4.10}$$

Calculation of the growth rate

Let us assume that the primary wave 0 has the largest amplitude within the triad, and serves as a thermostat to the system (its amplitude is subject to small variations on timescale of order t_1, $\frac{\partial A_0}{\partial t_1} \sim 0$). Waves 1 and 2 may therefore grow thanks to the energy provided by wave 0. We recall that all three waves are assumed to be of infinitely small amplitude, as requested by the RIT theory.

From equation 4.10, the set of amplitude evolution equation can be written as:

$$\partial_{t_1} A_1^{(\sigma_1)} = S_1 A_0^{(-\sigma_0)} A_2^{(-\sigma_2)} \tag{4.11a}$$

$$\partial_{t_1} A_2^{(\sigma_2)} = S_2 A_0^{(-\sigma_0)} A_1^{(-\sigma_1)} \tag{4.11b}$$

where

$$S_1 = \sigma_0 \sigma_2 \frac{(m_2 k_0 - m_0 k_2)}{2K_1^2 \omega_1} \quad \left((K_0^2 - K_2^2)\omega_1 + (\frac{k_0}{\omega_0} - \frac{k_2}{\omega_2})k_1 + (\frac{f}{N})^2 (\frac{m_0}{\omega_0} - \frac{m_2}{\omega_2}) m_1 \right) \tag{4.12a}$$

$$S_2 = \sigma_0 \sigma_1 \frac{(m_1 k_0 - m_0 k_1)}{2K_2^2 \omega_2} \quad \left((K_0^2 - K_1^2)\omega_2 + (\frac{k_0}{\omega_0} - \frac{k_1}{\omega_1})k_2 + (\frac{f}{N})^2 (\frac{m_0}{\omega_0} - \frac{m_1}{\omega_1}) m_2 \right) \tag{4.12b}$$

We can rewrite equation 4.11 as:

$$\partial_{t_1}^2 A_1 = S_1 S_2 |A_0|^2 A_1 \tag{4.13a}$$

$$\partial_{t_1}^2 A_2 = S_1 S_2 |A_0|^2 A_2 \tag{4.13b}$$

We can already deduce from equations 4.13 that waves 1 and 2 are expected to have the same temporal evolution.

Equation 4.13 shows that A_1 and A_2 will grow exponentially provided that $S_1 S_2 > 0$; the non-dimensional growth rate is $(S_1 S_2)^{1/2}$.

Going back to dimensional parameters, the growth rate of the secondary waves becomes:

$$\Gamma^2 = \alpha C_{01} C_{02} \tag{4.14}$$

where α is a prefactor, and C_{01} and C_{02} are interaction coefficients between the primary and secondary waves:

$$\alpha = \sigma_1 \sigma_2 \frac{(m_2 k_0 - m_0 k_2)}{K_1^2 \omega_1} \frac{(m_1 k_0 - m_0 k_1)}{K_2^2 \omega_2} |A_0^{\mathcal{R}}|^2 \tag{4.15a}$$

$$C_{01} = \left((K_0^2 - K_1^2)\omega_2 + N^2 (\frac{k_0}{\omega_0} - \frac{k_1}{\omega_1}) k_2 + f^2 (\frac{m_0}{\omega_0} - \frac{m_1}{\omega_1}) m_2 \right) \tag{4.15b}$$

$$C_{02} = \left((K_0^2 - K_2^2)\omega_1 + N^2 (\frac{k_0}{\omega_0} - \frac{k_2}{\omega_2}) k_1 + f^2 (\frac{m_0}{\omega_0} - \frac{m_2}{\omega_2}) m_1 \right) \tag{4.15c}$$

$A_0^{\mathcal{R}}$ is the real amplitude of the waves. Note that the complex amplitude of the waves is twice the real amplitude, $|A_0| = 2A_0^{\mathcal{R}}$.

4.2 Analyzing the numerical experiments in light of the resonant interaction theory

The previous derivation was made in very general terms. We will here apply the RIT to out study, before comparing the results from the simulations to the theoretical predictions.

4.2.1 Applying the RIT to the interaction involving inertial oscillations and internal lee waves

Equation 4.9 states that three internal waves are involved in a resonant triad if the algebraic sum of their frequencies and the sum of their wave vectors amounts to zero. Assuming two of these waves are the ILW and the IO and denoting the third wave with a $*$ subscript, these relations are:

$$\sigma_{ILW}\omega_{ILW} + \sigma_*\omega_* + \sigma_{IO}\omega_{IO} = 0 \tag{4.16a}$$

$$\sigma_{ILW}\boldsymbol{k}_{ILW} + \sigma_*\boldsymbol{k}_* + \sigma_{IO}\boldsymbol{k}_{IO} = 0 \tag{4.16b}$$

where the subscripts refer to the different waves, $\sigma = \pm 1$, $\boldsymbol{k} = (k, m)$ is the wave vector (in the present two-dimensional case) and ω the intrinsic frequency. We recall that the frequencies ω are assumed to be positive implying that the σ coefficients cannot be of the same sign. Along with the three dispersion relations, one gets 6 equations for 9 variables. Depending on the choice of $(\sigma_{ILW}, \sigma_*, \sigma_{IO})$, several triads, involving different waves, can arise. Since only the wave of largest amplitude (the internal lee wave) has the same spectral properties throughout the different triads, these can be considered as independent (Chow et al. 1996).

Let us first consider that $\sigma_{ILW} = -\sigma_{IO} = -\sigma_* = 1$. The problem is closed by expressing that the lee wave parameters verify:

$$k_{ILW} = k_T \tag{4.17a}$$

$$\omega_{ILW} = U_G k_T \tag{4.17b}$$

and by writing that the inertial oscillations are homogeneous in the horizontal plane with frequency $|f|$:

$$k_{IO} = 0 \tag{4.18a}$$

$$\omega_{IO} = |f|. \tag{4.18b}$$

Using the dispersion relations, we now have 5 equations for 5 variables and the problem can be solved analytically. The solution of these equations is presented in Table 4.1 for clarity:

ILW	$*$	IO
$k_{ILW} = k_T$	$k_* = k_T$	$k_{IO} = 0$
$\omega_{ILW} = U_G k_T$	$\omega_* = U_G k_T - \lvert f \rvert$	$\omega_{IO} = \lvert f \rvert$
$m_{ILW} = -\sqrt{\frac{N^2 - (U_G k_T)^2}{(U_G k_T)^2 - f^2}} k_T$ (4.19)	$m_*^2 = \frac{N^2 - (U_G k_T - \lvert f \rvert)^2}{(U_G k_T - \lvert f \rvert)^2 - f^2} k_T^2$ (4.20)	$m_{IO} = m_{ILW} - m_*$ (4.21)

Table 4.1 – *Wave characteristics of the triad involving the wave $*$ of frequency $U_G k_T - \lvert f \rvert$*

ILW	$*$	IO
$k_{ILW} = k_T$	$k_* = k_T$	$k_{IO} = 0$
$\omega_{ILW} = U_G k_T$	$\omega_* = U_G k_T + \lvert f \rvert$	$\omega_{IO} = \lvert f \rvert$
$m_{ILW} = -\sqrt{\frac{N^2 - (U_G k_T)^2}{(U_G k_T)^2 - f^2}} k_T$ (4.22)	$m_*^2 = \frac{N^2 - (U_G k_T + \lvert f \rvert)^2}{(U_G k_T + \lvert f \rvert)^2 - f^2} k_T^2$ (4.23)	$m_{IO} = m_* - m_{ILW}$ (4.24)

Table 4.2 – *Wave characteristics of the triad involving the wave $*$ of frequency $U_G k_T + \lvert f \rvert$*

The case $\sigma_{ILW} = \sigma_* = -\sigma_{IO} = 1$ is equivalent to the case described above. Finally, the case $\sigma_{ILW} = -\sigma_* = \sigma_{IO} = 1$ is displayed in Table 4.2.

In short, two possibilities arise for the frequency of the third wave ($\omega_* = U_G k_T \pm \lvert f \rvert$), and two possibilities arise for the choice of the sign of the vertical wavenumber of wave $*$, making a total of 4 possible triads, each corresponding to a different IO vertical wavenumber.

Thus, we can compute the parameters of the waves possibly involved in energy exchanges with the inertial oscillations and infer whether the IOs are expected to grow. The vertical wavenumber of the IOs for the relevant triads can also be computed.

4.2.2 Comparison with the simulations

Figure 4.1 is a power spectrum of the vertical velocity w computed in a frame of reference moving at the geostrophic velocity U_G for simulation $H_{20}L_{2\_}fs$. The dashed line is the confidence level at 99%, implying that the spectrum significantly departs from red noise when it exceeds the dashed line.

Four peaks clearly emerge from the power spectrum, in agreement with the RIT: $\omega = U_G k_T$, $\omega = |f|$ and $\omega = U_G k_T \pm |f|$. This is consistent with the prediction that the original ILW amplifies, or gives rise to, three waves predicted by the resonant interaction theory, the IOs and the sum and difference of the ILW and IO. Smaller peaks can also be seen at $\omega = U_G k_T + 2|f|$ and $\omega = U_G k_T + 3|f|$, indicating the existence of higher order triads.

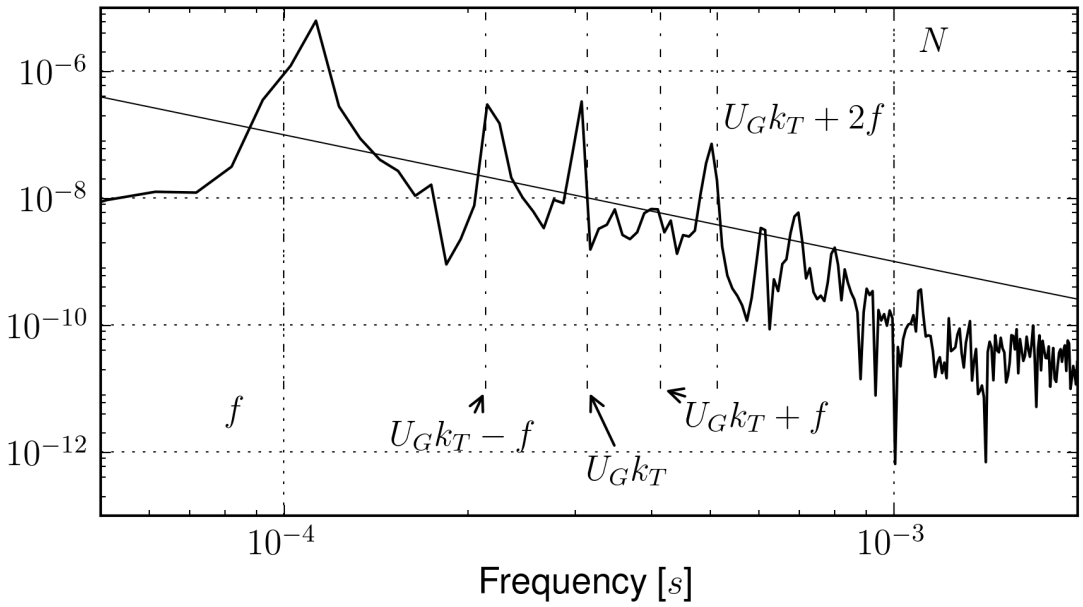

Figure 4.1 – *Variance preserving power spectrum of w for experiment $H_{20}L_2$, near 600 m above the topography, computed in a frame moving with the geostrophic velocity U_G. When the curve is larger than the dashed line, it departs significantly from red noise at 99% level. The inertial and buoyancy frequencies are indicated in dashed-dotted line, as well as the frequencies predicted by the resonant interaction theory.*

Eq. (4.13) indicates that at early times when the amplitude of IOs is weak, the

evolution of IOs is exponential in time if $S_1 S_2 > 0$. In the range of parameters we use, $\Gamma > 0$ for all simulations except for those with $f = 2.10^{-4}$ s^{-1}, where Γ is not defined since $U_G k_T - 2|f| < |f|$. Therefore, one does not expect these simulations to present any significant IO growth. Consistent with this prediction, we saw in Chapter 3 (figure 3.2) that simulations with small and moderate amplitude of the topography ($h_T = 20$ and 40 m) and with f double exhibit hardly any growth of inertial oscillations over the time of the simulations (results of the weakly nonlinear RIT do not strictly apply to the $h_T = 80$ m topography).

For initial times, the growth rate Γ can be estimated by fitting the curves with an exponential function over the time of growth of the inertial oscillations.

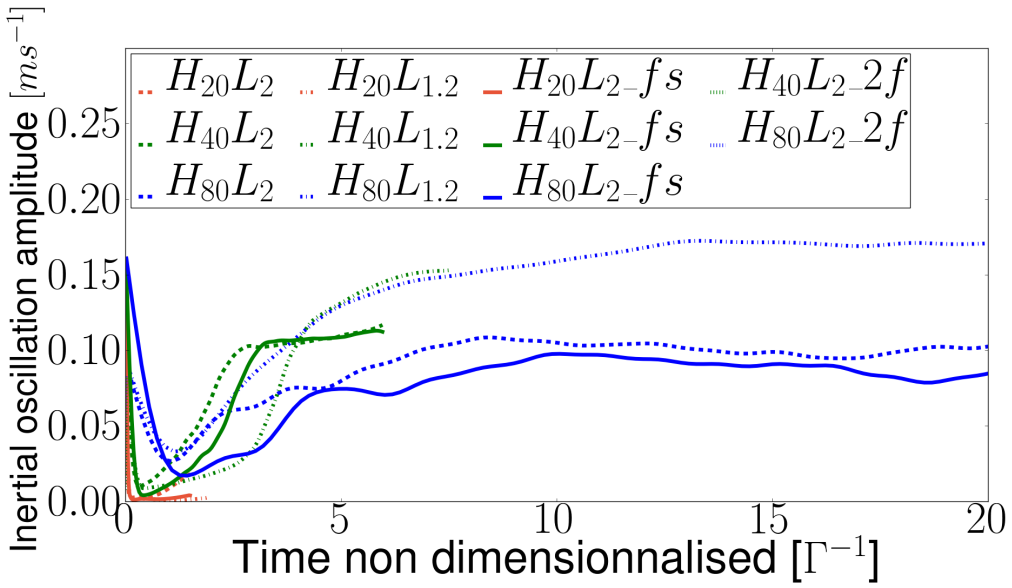

Figure 4.2 – *Time evolution of the IOs, as in figure 3.2, except that time is scaled by the growth rate from the resonant interaction theory.*

Figure 4.2, equivalent to Fig. 3.2, displays the evolution in time of the IO amplitude at 100 m above topography, time being now scaled by Γ^{-1}. Here again, as for the asymptotic theory, eyeballing the curves indicates reasonable fit, but such qualitative measure gives little credit to the theory. For a more quantitative assessment, we used the same fitted estimates of the growth rates as in Section 3.

Figure 4.3 is a scatter plot of Γ measured from the simulations versus Γ computed from the resonant triad theory. Growth rates are normalized by the inertial frequency. Simulations for which the theory predicts a strong growth rate (corresponding to a typical time-scale lower than 3 inertial periods) are indicated with a grey or black marker; otherwise (when this time is higher than 10 inertial periods) the marker is left empty. Only positive growth rates are shown.

Since simulations with $h_T = 20$ m present little growth of IOs, the computation of the growth rate for these simulations is not very reliable, and little can be said of the comparison of the theoretical predictions to the simulations. Empirical growth rates for cases of higher topographic amplitude are much more robust and compare reasonably well with the RIT, although the theory present a systematic overestimation of the growth rates. The departure of numerical simulations from the resonant interaction theory, which is a weakly non-linear theory, is expected to become significant when the non-linearity grows. That is because the weakly non-linear theory struggles to keep track of finite amplitudes, and fails to capture feedbacks that could become of leading order in the presence of strong non-linearities. However, since the growth rate is computed at the beggining of the simulations, even the most nonlinear simulations considered here are expected to present a weakly nonlinear behavior.

Figure 4.3 is not significantly different than figure 3.4. In that respect, those figures do not allow for differentiating between the theories. Let us consider a different criterion instead.

The Hasselman criterion (Hasselmann 1967), states that a primary internal wave involved in a resonant triad is unstable if its frequency is the highest frequency of the three waves. From the expression of the growth rate of the inertial oscillations and this criterion, we can now only consider the triad involving the $*$ wave of frequency $U_G k_T - |f|$. The expression of the vertical wavenumber of the IO corresponding to this triad is

$$m_{IO} = k_T \left| \sqrt{\frac{N^2 - (U_G k_T)^2}{(U_G k_T)^2 - f^2}} - \sqrt{\frac{N^2 - (U_G k_T - |f|)^2}{(U_G k_T - |f|)^2 - f^2}} \right|. \tag{4.25}$$

The vertical phase speed of the IO can then be computed using $c_\phi^z|_{IO} = f/m_{IO}$.

Figure 4.4 shows a time-height diagram of the horizontal velocity of the IO component for simulation $H_{20}L_{2\_}fs$. The tilted line has a slope equal to the vertical phase speed of the IOs.

Figure 4.4 shows that the vertical phase speed of the IOs is of the same order as the theoretical predictions from the resonant interaction theory. This agreement provides further information on the properties of the inertial oscillations inferred from the resonant interaction.

The asymptotic theory started to give ground to the RIT theory when it got wrong estimates of the vertical dependency of the growth rate. The RIT theory acquired some more credibility by correctly predicting the wave spectrum. The downfall of the asymptotic theory is achieved with a simple physical principle, that could have been used at the very beggining (known as Occam's razor (Monvoisin 2007), or ontological parsimony (Newton 1726)). Since the RIT theory does not require as many assumptions as the asymptotic theory (especially concerning the idealized dissipation), one should favor the alternative that uses the least unphysical assumptions.

4.3 The computation of $\partial_z\overline{u'w'}$ in the RIT

Although the RIT proved more robust than the asymptotic theory, the latter was constructed from many solid bricks (such as the momentum deposition concept), that are not used by the RIT. The main question that remains is whether momentum deposition also occurs in the RIT. Before performing the computation of $\partial_z\overline{u'w'}$ in the RIT framework, we briefly discuss about the importance of this momentum flux in other theories.

Many analytical theories (such as the quasi-geostrophic (QG) model for instance) using Eulerian mean state that a change in zonal (averaged along the x-axis) flow arises from the divergence of internal wave stresses, $-\boldsymbol{\nabla}\cdot\overline{u'\boldsymbol{u}'}^x$.

Since our setting is periodic in the x-direction and two-dimensional, $\begin{pmatrix} \partial_x \\ \partial_y \end{pmatrix} = \begin{pmatrix} 0 \\ 0 \end{pmatrix}$, the QG theories would predict, as do Nikurashin and Ferrari (2010),

$$\partial_t \overline{u}^x = \partial_t U_G + U_{IO} = \partial_t U_{IO} = -\partial_z \overline{u'w'}^x \tag{4.26}$$

In this section, will compute the internal wave momentum deposit $-\partial_z\overline{u'w'}^x$ from the RIT theory, to see if the predictions can agree with other theories.

It is noteworthy that the Charney-Drazin, or non-acceleration theorem, states that steady, linear, non-dissipative waves do not induce any momentum flux (Andrews and McIntyre 1978). This does not contradict with the present study, since the internal waves other than the ILWs are not stationary, but grow in time, as do the IOs (which are a mean flow from the horizontal mean). Moreover, once the mechanism is of large enough amplitude, intense wave breaking occurs, which introduces dissipation in the problem, another reason to discard the Charney-Drazin theorem.

According to the definitions used in the triad interaction theory, the total stream-function follows:

$$\psi^0 = \sum_{j=0}^{2} A_j e^{i\phi_j} + \text{c.c.} \tag{4.27}$$

$$= \sum_{j=0}^{2} A_j e^{i(\boldsymbol{k}_j \boldsymbol{x} - \omega_j t)} + \text{c.c.} \tag{4.28}$$

$$u' = \partial_z \psi = \sum_{j=0}^{2} A_j i k_j^z e^{i\phi_j} + \text{c.c.} \tag{4.29}$$

$$w' = -\partial_x \psi = -\sum_{j=0}^{2} A_j i k_j^x e^{i\phi_j} + \text{c.c.} \tag{4.30}$$

where $\boldsymbol{k}_j = k_j^x \boldsymbol{e_x} + k_j^z \boldsymbol{e_z}$ and $\omega > 0$.

$$u'w' = (\sum_{j=0}^{2} A_j i k_j^z e^{i\phi_j} + \text{c.c.})(-\sum_{n=0}^{2} A_n i k_n^x e^{i\phi_n} + \text{c.c.}) \tag{4.31}$$

$$= \sum_{j=0}^{2}\sum_{n=0}^{2} (A_j k_j^z e^{i\phi_j} - A_j^* k_j^z e^{-i\phi_j})(A_n k_n^x e^{i\phi_n} - A_n^* k_n^x e^{-i\phi_n}) \tag{4.32}$$

$$= \sum_{j=0}^{2}\sum_{n=0}^{2} k_j^z k_n^x (A_j A_n e^{i(\phi_j+\phi_n)} - A_j A_n^* e^{i(\phi_j-\phi_n)} - A_j^* A_n e^{-i(\phi_j-\phi_n)} + A_j^* A_n^* e^{-i(\phi_j+\phi_n)}) \tag{4.33}$$

$$\partial_z u'w' = \sum_{j=0}^{2}\sum_{n=0}^{2} k_j^z k_n^x (i(k_j^z + k_n^z) A_j A_n e^{i(\phi_j+\phi_n)} \tag{4.34}$$

$$-i(k_j^z - k_n^z) A_j A_n^* e^{i(\phi_j-\phi_n)} \tag{4.35}$$

$$+i(k_j^z - k_n^z) A_j^* A_n e^{-i(\phi_j-\phi_n)} \tag{4.36}$$

$$-i(k_j^z + k_n^z) A_j^* A_n^* e^{-i(\phi_j+\phi_n)}) \tag{4.37}$$

Noting $\sigma_m = \pm 1$, $A_m^{(1)} = A$ and $A^{(-1)} = A^*$, the previous expressions holds:

$$\partial_z u'w' = \sum_{\sigma_j=\pm 1} \sum_{\sigma_n=\pm 1} \sum_{j=0}^{2}\sum_{n=0}^{2} i\sigma_j\sigma_n k_j^z k_n^x (\sigma_j k_j^z + \sigma_n k_n^z) A_j^{(\sigma_j)} A_n^{(\sigma_n)} e^{i(\sigma_j\phi_j + \sigma_n\phi_n)} \tag{4.38}$$

Going from $\partial_z u'w'$ to $\partial_z \overline{u'w'}$ holds non trivial terms only for cases where the term proportional to x in the exponential vanishes:

$$\sigma_j k_j^x + \sigma_n k_n^x = 0$$

.

Several cases arise:

- $k_j^x = k_n^x$. Then, either $\sigma_j = -\sigma_n$, or $k_j^x = 0$. Both cases end up nullifying the prefactor, and the interaction coefficient becomes 0.
- $k_j^x \neq k_n^z$. Then, the only solution arises from the interaction condition (4.9): $\sum_j \sigma_j k_j^x = 0$, knowing that $k_{IO}^x = 0$, j and n refer to the ILW and the * wave. It entails that $\sigma_{ILW}\phi_{ILW} + \sigma_*\phi_* = -\sigma_{IO}\phi_{IO} = -\sigma_{IO}(k_{IO}^z \boldsymbol{z} - \omega_{IO} t)$.

Finally, the momentum deposit equation boils down to:

$$\partial_z \overline{u'w'} = -i\sigma_{ILW}\sigma_{IO}\sigma_*(k^z_{ILW}k^x_* + k^z_* k^x_{ILW})k^z_{IO} A^{\sigma_{ILW}}_{ILW} A^{\sigma_*}_* e^{-i\sigma_{IO}\phi_{IO}} + \text{c.c.} \tag{4.39}$$

$$\tag{4.40}$$

Or, for the sake of clarity,

$$\partial_z \overline{u'w'} = A_{\partial_z \overline{u'w'}} \quad e^{-i\sigma_{IO}(k^z_{IO} z - \omega_{IO} t)} + \text{c.c.} \tag{4.41}$$

where $A_{\partial_z \overline{u'w'}}$ is a non zero amplitude.

The main results that arise from this calculation are:

- The traditional momentum deposit $\partial_z \overline{u'w'}$ calculated from the RIT is non zero.
- It has a vertical structure, and the same vertical wavenumber as the IOs.
- It oscillates at $\omega_{IO} = f$.
- As a result from the two previous points, it propagates in the vertical at the vertical phase speed of the IOs.

The RIT is fully consistent with momentum deposition, and predicts the vertical profile of $\partial_z \overline{u'w'}$.

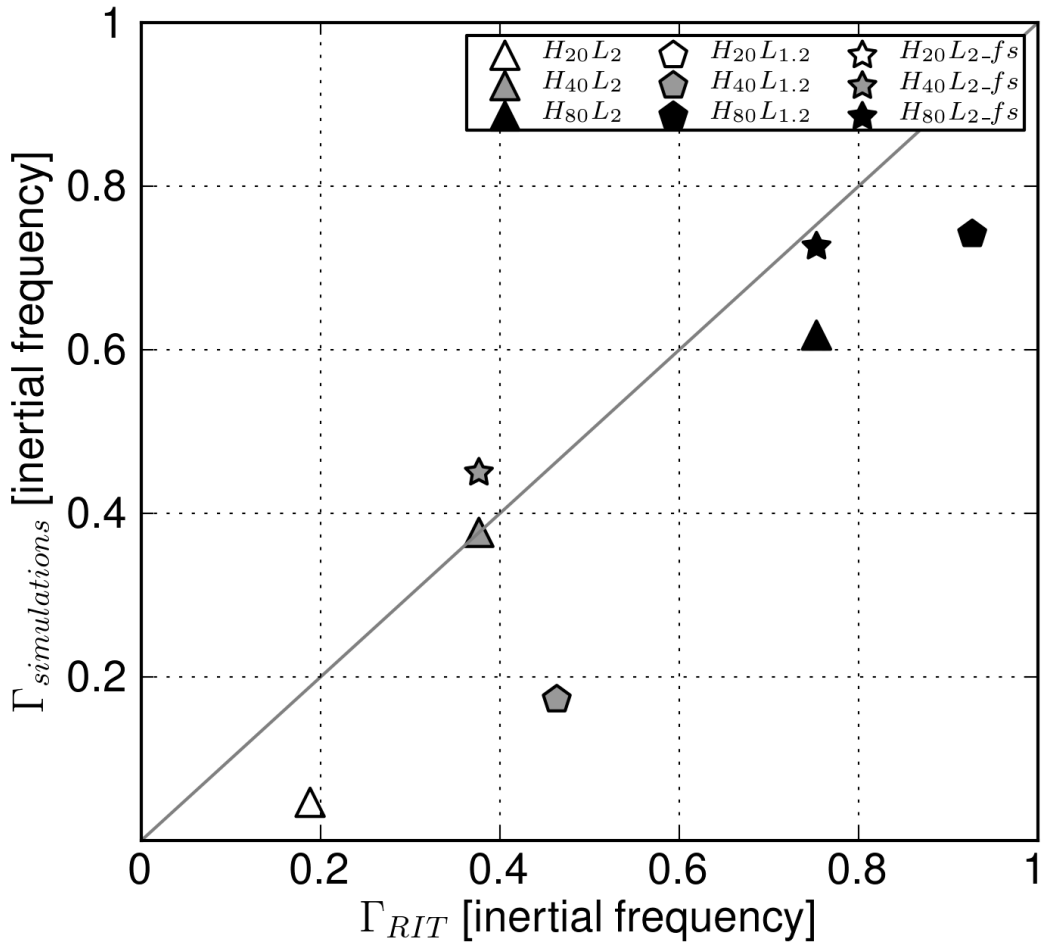

Figure 4.3 – *Scatter-plot of the growth rate diagnosed from the simulations and that predicted by the RIT.*

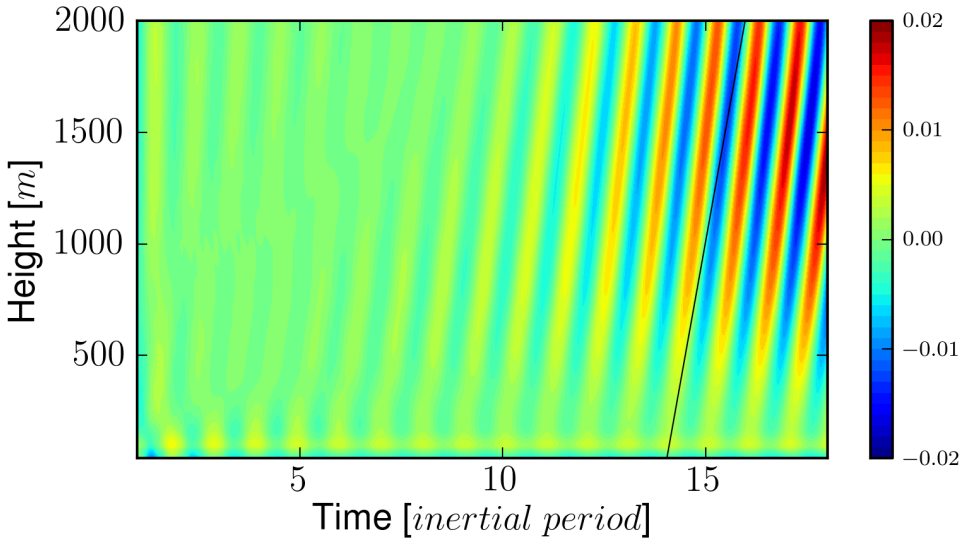

Figure 4.4 – *Time-height diagram of the horizontal velocity of the inertial oscillations for* $H_{20}L_{2\_}fs$. *The slope of the red line has the value of the vertical phase speed of the IOs* f/m_{IO} *with* m_{IO} *derived from the resonant interaction theory. Only the triad corresponding to a third wave of frequency* $U_G k_t - |f|$ *and negative vertical wavenumber is shown.*

Towards a three dimensional description

5

The previous chapters shed light on the energy pathways involved in the life-cycle of an internal lee wave travelling in a two-dimensional rotating frame. The following sections will now investigate how three-dimensional dynamics can impact on the fluid response, and attempt to build a numerical configuration able to tackle the questions raised by the introduction of a third dimension.

5.1 Possible implications of three-dimensional dynamics

5.1.1 Specificities of two and three-dimensional studies

The two-dimensional framework used in our studies up to this point prevents a number of physical processes from occurring. When moving to a fully three-dimensional space we can expect severe limitations to our previous results to be put forward, either concerning the physics of the wave generation, or the possibility to build up meridional gradients.

How bottom energy conversion might differ in a three-dimensional domain.

The bottom energy conversion theory previously presented in our study is developed for a two-dimensional configuration. A three-dimensional version of this theory predicts a slight decrease in the amount of internal lee waves emitted, but still of the same order of magnitude (Nikurashin 2009). This estimate relies

on the assumption that the bottom reaching mean current is not horizontally deviated by the topography, and flows directly above it. Although this may be the case for a small enough topography, other behaviors can be expected that would lead to yet less internal lee wave emission. Reinecke and Durran (2008) suggest to categorize the different flow regimes through the Froude number ($Fr = \frac{U}{Nh_T}$ as previously defined):

- If $Fr \ll 1$, the bottom mean flow does not have enough kinetic energy to go over the topography and generate internal lee waves. The flow is either partially *blocked* by the topography, or it *splits* and bypasses the obstacle on its sides (Nikurashin et al. 2014).
- For $Fr \sim 1$, the flow can also be partially *blocked* or *splitted* by the topography. Some internal wave emission is expected, but it could be reduced by a factor of up to 35% (Nikurashin et al. 2014).
- If $Fr \gg 1$, the topography hardly modifies the flow. While the theoretical computation holds, it predicts a wave field of amplitude proportional to Fr^{-2}, which results in little wave activity.

From these arguments, moving from a two to three-dimensional simulation is expected to reduce the amplitude of the flow *above* topography, the displacement of the isopycnals, and the emission of internal lee waves. According to the energy pathways presented above, this weaker internal lee wave field will result in a weaker feedback mechanism, and eventually less inertial oscillations and energy dissipation will be observed.

The possibility of building meridional gradients, and their impact on the flow behavior.

In a three-dimensional setting the fields are allowed to vary in the meridional direction. This allows in particular meridional mass gradients to equilibrate vertically sheared flows through the thermal wind balance. As such, a meridional transport of mass can lead to the modification of the slowly varying flow, which in turn might affect the internal wave field. In parallel, we saw in the previ-

ous chapter the importance of momentum deposition from wave-wave interactions. Since meridional gradients and mean flow modifications are permitted in three dimensions, momentum deposition is not confined to wave-wave interactions anymore, but can be extended to wave-mean flow interactions, where mean flow denotes the zonally averaged, slowly varying motions. From these two arguments, it follows that wave-wave interactions as described in previous chapters will now compete with wave-mean flow interactions.

5.1.2 Implications of momentum deposition on large scale circulation

Section 4.3 showed the presence of significant momentum deposition in our two-dimensional simulations through the term $\partial_z \overline{u'w'}$, as well as the importance of momentum deposition by internal waves for atmospheric dynamics. Very few ocean studies have been conducted on this subject, and to our knowledge they mostly focus on equatorial deep jets (Muench and Kunze 1999) or on large scale, global descriptions (Naveira Garabato et al. 2013). This raises several questions: is momentum deposition crucial in the deep ocean? Are its consequences the same as described in atmospheric literature? We shall see in this section that answering to these questions requires a three-dimensional setting.

Momentum deposition on the mean flow

In the absence of uniform and constant forcing, the barotropic flow can evolve freely, and wave-mean flow interactions can take place. The effects of the waves on the mean flow can be formalized through the Eliassen-Palm (E-P) flux tensor $\vec{\vec{F}}$ (Andrews and McIntyre 1978), where the acceleration of the mean flow is represented through the Eliassen-Palm flux divergence $\nabla \cdot \vec{\vec{F}} = \sum_{ij} \partial_j F_{ij} \boldsymbol{e}_i$ (Andrews and McIntyre 1978, Bühler 2014). For illustration, let us write the E-P flux vector that acts on a zonal mean flow $\overline{u}^x$:

$$\begin{aligned} \vec{\vec{F}} &= \begin{bmatrix} F_{xy} & F_{xz} \end{bmatrix} \\ &= \begin{bmatrix} \overline{u'v'}^x & \overline{u'w'}^x + \frac{f}{N^2}\overline{v'b'}^x \end{bmatrix} \end{aligned} \tag{5.1}$$

Although wave-mean flow interactions are supposed to take place on longer time scales than wave-wave interactions (Lott 2003), it may drive a significant flow through cumulative effects. Note the presence of $\overline{u'w'}^x$, which entails a forcing term $\partial_z \overline{u'w'}^x$ in $\nabla \cdot \vec{\vec{F}}$, as used in previous chapters.

If the internal wave motion ceases (through wave breaking or dissipation for instance), momentum conservation implies that the wave-induced momentum should persist: a mean flow is left. The E-P flux tensor is a very useful formalism to represent the associated transfer of energy to the mean flow.

Meridional mass redistribution

If ILW are generated at the topography and undergo momentum deposition, the wave-mean flow interactions (which does not necessarily occur close to the topography) lead to a vertically sheared geostrophic flow. The thermal wind balance states that a vertical gradient of geostrophic speeds has to equilibrate with a horizontal gradient of density (Haynes et al. 1991):

$$\frac{\partial \boldsymbol{u}_g}{\partial_z} = -\frac{g}{f\rho_0}\hat{\boldsymbol{z}} \wedge \nabla\rho \tag{5.2}$$

where $\hat{\boldsymbol{z}}$ is a vertical unit vector. Thus, for momentum deposition to accelerate the zonal flow and establish the meridional mass gradient, mass transport is required ($\partial_y \rho \neq 0$). The parameterisation of this mass redistribution mechanism was found to be fundamental in correctly representing the lower stratospheric circulation (Garcia and Boville 1994), which hints to the need of similar parameterisations in the ocean.

Questions raised by a fully three-dimensional framework

We shall here prepare future studies aiming at understanding what the energy pathways are in the unconstrained ocean by investigating the following question:

- How intense is the bottom energy conversion from the geostrophic flow to the internal lee wave field?

- Is the momentum deposition of the ILWs onto the IOs as vigorous as in the two-dimensional case?
- How is the geostrophic flow modified by the momentum deposition from the ILWs?
- Is there an important redistribution of mass in the meridional direction?
- Is TKE dissipation significantly different that in the two-dimensional case?

We will rely on atmospheric literature so as to understand what phenomenons are to be expected. We will present the development strategy for building numerical simulations as close as possible to the open ocean with respect to the mechanisms at play. Once such simulations have been designed, specific theoretical tools to understand and quantify the transfers at play will be presented. Finally, we describe preliminary results of three-dimensional simulations.

5.2 Design of the numerical experiment

5.2.1 A new numerical code

We saw in the previous section that the two-dimensional investigation described in the first chapters of this manuscript does not permit to fully investigate the effects of internal lee waves on the mean flow, neither through changes in mass horizontal distribution nor through momentum deposition. Answering these questions requires numerical simulations that:

- are fully three-dimensional, to permit meridional gradients,
- do not force the mean flow through a constant body force but allow it to evolve freely,
- have a meridionaly localized topography, to investigate the dynamics far from the wave emission,
- are fully non hydrostatic, to resolve the internal wave breaking processes,
- have a domain large enough to englobe the meridional gradients relative to a change in the mean flow, typically, from the thermal wind balance, more

than the internal Rossby deformation radius R_d ($R_d = NH/f$, where H is a typical scale height, namely the vertical height of the physical domain).

Moreover, the analytical tools used for our two-dimensional simulations are not sufficient to answer these questions. The mean flow has to be diagnosed, thus changing the calculation of the inertial oscillations and internal wave fields. Andrews and McIntyre (1978) showed that the usual frameworks do not correctly account for wave-mean flow interactions, and developed the Transformed Eulerian Mean (TEM) approach for such use.

We will first describe how we devised and developed numerical simulations to tackle these questions, before describing the diagnostic framework that would be best for investigating said simulations.

Let us come up with a rough estimate of the computation cost of an ideal, low resolution simulation. We study a high latitude phenomenon, where the planetary rotation is supposed to have an important impact. The Earth's rotation has an impact on horizontal scale typically of the first internal Rossby deformation radius R_d. To assess these effects, the physical domain meridional size should be larger than R_d, which in our parameter range amounts to about 20 km. To correctly address the effects of the internal waves on the mean flow also requires that the non hydrostatic equations are solved. Developing a 20 km x 20 km simulation of grid size 50 m would require 400^2 grid cells in the horizontal. Add to this at least 2 km depth and vertical resolution of at utmost 50 m leads to a total of $400^2 \times 40 = 6.4 \quad 10^6$ grid cells, which is not affordable for such prospective and uncertain investigation. An alternate configuration is proposed below.

A new code

The Symphonie NH (SNH) model used in the two-dimensional simulations required a full week of computation to output 20 simulated inertial periods on the supercomputer JADE (CINES, France). This long waiting time is explained by the fact that our setting was at a scaling optimum (the number of cells per processor ensured fastest computation), and hence the duration of the numerical

computation was directly constrained by the choice of the time-step. The version of the SNH code we used computes separately barotropic and baroclinic motions, with separate time steps ($\Delta_t^{barotropic} < \Delta_t^{baroclinic}$), because of the fast propagation of barotropic motions. In practice, we had $\Delta_t^{baroclinic} / \Delta_t^{barotropic} \leq 6$. We estimated that three-dimensional simulations with the same parameters would take at least a month of computation for a single simulation. More recent versions of Symphony NH are far more efficient though. The compressible Boussinesq equations are now solved in order to waive the dependency of $\Delta_t^{baroclinic}$ on $\Delta_t^{barotropic}$ and therefore to speed up the code (Marsaleix et al. 2011). In the meantime, we chose another numerical model for the three-dimensional study: the Non Hydrostatic Ocean model for the Earth Simulator (NHOES, Aiki and Yamagata 2004). The NHOES model, based on the MITgcm, is similar to Symphonie NH in most aspects, except that the vertical coordinate is not topography following but Cartesian, with partial bottom steps (Adcroft et al. 1997). Moreover, the upper boundary is represented by a rigid surface, which drops the constraint on the barotropic to the baroclinic time steps, ensuring fast computation. Although spurious effects might occur near topography, this code therefore appeared to be more suitable to deal with our three-dimensional problem.

First steps: reproducing previous works

Moving from the design of the setup to the numerical experiments with a different code amounts to building numerous simulations brick by brick. The first step consists in reproducing previous results, to assess their robustness with NHOES. To this end, a two-dimensional simulation was conducted to reproduce simulation $H_{40}L_{2\_}fs$ in z-coordinates. Similar IO and TKE dissipation rate amplitudes and profiles were found. For illustration, figure 5.1 shows the time-height diagram of the IO field for setting $H_{40}L_{2\_}fs$ in NHOES and SNH. The NHOES simulation has a resolution twice rougher than the SNH simulation, which we suspect might explain the slight changes in the figure details. The black lines cor-

respond to a signal moving at the vertical phase speed of the IOs as predicted by the RIT.

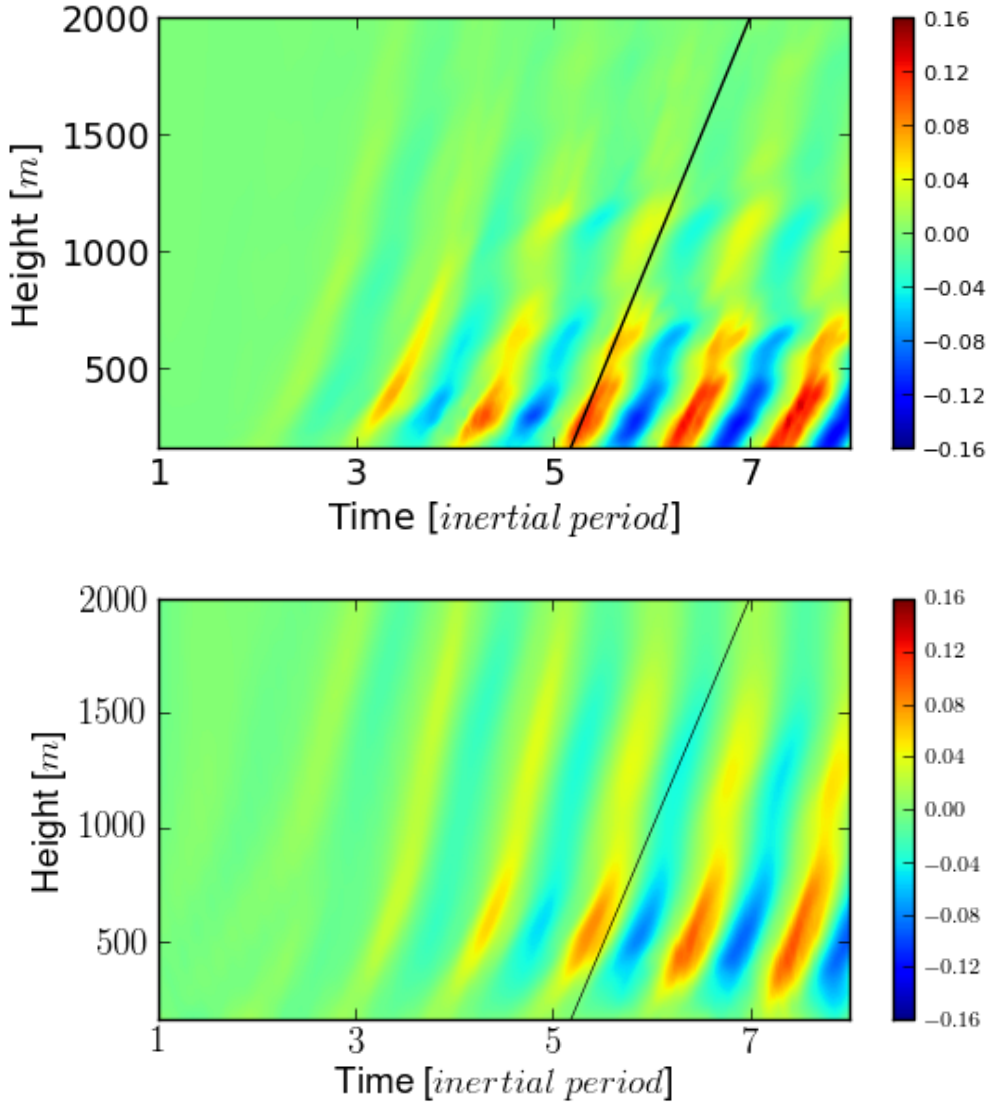

Figure 5.1 – *Comparison of the time-height diagrams of the IO field above the topography for setting $H_{40}L_{2\_}fs$ in NHOES (top) and SNH (bottom).The NHOES simulation has a resolution twice rougher than the SNH simulation The black lines correspond to a signal moving at the vertical phase speed of the IOs as predicted by the RIT.*

This first step proved to be conclusive, namely the NHOES code can reproduce the two-dimensional setting. Next is moving to three-dimensionality, if possible in comparison with existing results. To do so we considered the three-dimensional work of Nikurashin (2009), which is an extension of the two-

dimensional setting to a sinusoidal topography in both directions:

$$h(x, y) = h_T \cos(k_T x) \cos(l_T y) \tag{5.3}$$

where k_T and l_T are the zonal and meridional wavenumbers, and h_T is the amplitude of the topography (half the peak-to-peak distance).

We reproduced one experiment, with both topographic wavelengths of 2 km, and topographic amplitude $h_T = 40$ m. The other parameters are the same as Nikurashin (2009), and also the same as used in our two-dimensional study. Comparison proved to be quite convincing as well (not shown).

5.2.2 Defining the experimental setup

From the discussion above we now attempt to define a numerical setting that will permit to investigate both wave-wave and wave-mean flow interactions in the energy pathways of internal lee waves.

This is achieved as follows. First, since the domain needs to be large especially in the meridional direction, we can reduce our problem by using periodic boundary conditions in the x direction. This allows for a relatively small zonal direction ($\sim$ 2 km, or 40 cells) and corresponds to an infinity of bumps in the x direction. However, we will later see that doing so requires careful thinking on the forcing of the flow, since upstream forcing is not possible anymore. Secondly, the meridional boundary conditions can be adapted so as to lower the size of the domain in the N-S direction. We first consider the domain to have 500 m with flat bottom on each side of the topography, to be able to investigate the behavior of the flow further from bathymetry and avoid spurious boundary effects. In addition, open boundary conditions are set, that radiate the signals with phase speed larger than a prescribed threshold (Aiki and Yamagata 2004). The above two modifications reduce the amount of grid cells needed to $\sim 0.5 - 1 \quad 10^5$ cells, which is now affordable. This choice of meridional extent falls quite short on the Rossby radius condition, and as such might not capture all the mass re-

distribution in the flow. However, the compromise permits the investigation of momentum deposition that can occur along the wave trajectory.

Next is choosing the topographic shape so as to emit ILW and be consistent with the lateral boundary conditions. Since the aim of this study is to see the effects of three-dimensionality, the possible mass redistributions and momentum transfer, it is important to be able to contrast the areas above, on the side of and far from the topography in the N-S direction. As such, the topographic feature needs to have a compact support in the meridional direction: the function defining the topography in the meridional direction is non zero only over a restricted area smaller than the cross-section extent of the domain (or, equivalently, $h_T(x, y) = 0$ over a non zero area at the meridional boundaries). However and as mentioned above, along the direction of the mean flow, the mass redistribution, the momentum transfer and their impacts are expected to be of lesser amplitude. As such, the topography can consist in a periodic, sinusoidal bump, which also has the advantage of being monochromatic and thus simplify Fourier analysis.

An analytical formulation of these two conditions gives a topographic height defined by:

$$h(x,y) = h_T \frac{1}{2}(1+\cos(2\pi\frac{x}{L_x}))(1+\cos(2\pi\frac{y}{L_y})) \\ \frac{1}{4}(1+\tanh(10\frac{L_y/2+y}{L_y}))(1+\tanh(10\frac{L_y/2-y}{L_y})) \tag{5.4}$$

where the x, y coordinates originate from the top of the bump, L_x and L_y are respectively the zonal and meridional sizes of the topography. h_T corresponds to the topographic height as defined in the two-dimensional simulations, entailing that the peak-to-peak distance is $2h_T$.

The tanh functions ensure that the topography is at compact support in a smoother way than a boxed window. The subsequent topographic profile is shown in figure 5.2.

The last remaining feature to build is the forcing, that should ensure that a

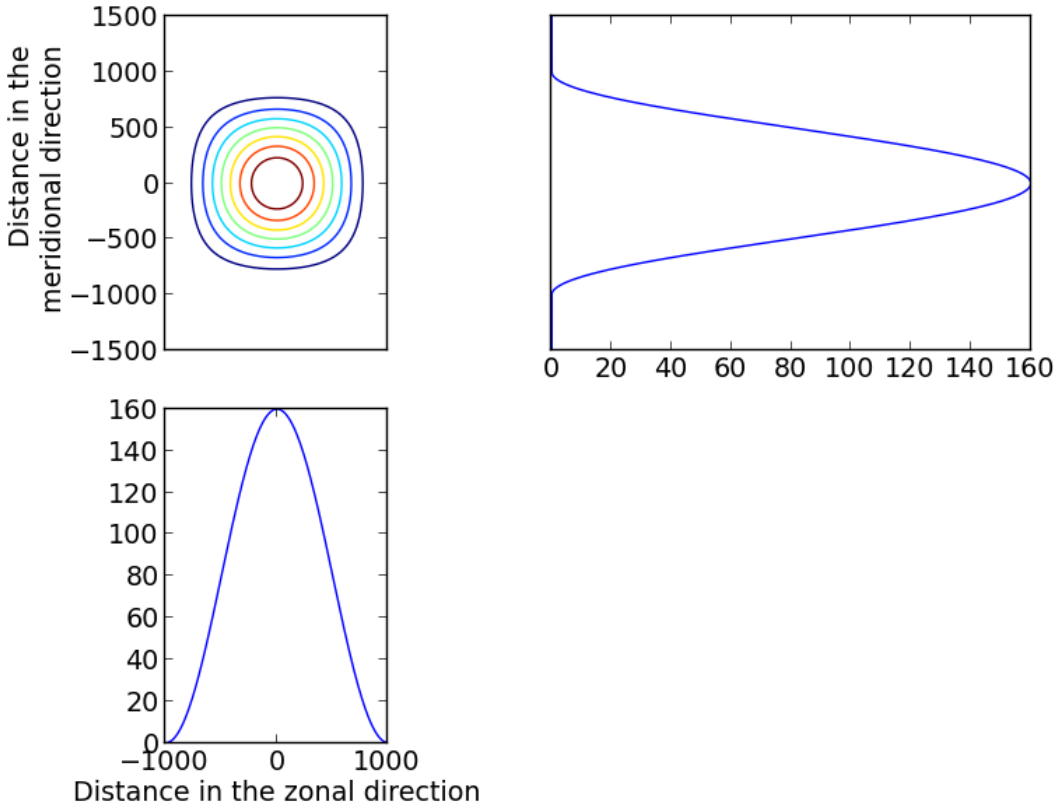

Figure 5.2 – *Topographic profile corresponding to Eq. 5.4*

bottom reaching jet impinges on the topography to generate ILWs. To this end we chose to use a body forcing during the first 24h, as in the two-dimensional simulations. However, after 24h the forcing is stopped altogether, and the simulation is free to spin down to rest. This entails that, after being forced in the whole domain, the flow evolution is completely free, which is a major difference with previous chapters (and also Nikurashin 2009 for instance). One can expect that after a long time the flow might set to rest. Comparing the different spin down regimes in simulations of various parameters would provide useful material that could thereafter be used to design a suitable configuration for our problem, depending on the relative importance of the different physical processes at play.

5.2.3 Practical implementation

The transition to the new setting was done in several successive steps that are here briefly described. Each step was validated by a short numerical test over 0.1 inertial period, except when stated otherwise.

- Once the 'physical' settings were set then came the tuning of the purely numerical parameters, starting with the horizontal and vertical resolution. We chose two main configuration: high and low resolution. High resolution simulations are set to have horizontal resolution of 12.5 m and vertical resolution of 10 m under the sponge layer. Low resolution simulation horizontal and vertical resolutions are respectively set to 50 and 30 m. The development was systematically done at low resolution, high resolution being planned only for a final study.
- The choice of the grid size and of the domain extent directly gives the amount of grid points needed in each horizontal and vertical direction. The NHOES code enable multi-processing, meaning that the calculations can be done with different processors, each processor doing its calculation in parallel with the other. Each processor would then carry computations on a small portion of the domain: a volume of a few grid points in both horizontal directions, but spanning from bottom to top. This allows for a much faster calculation: in a ideal frame the duration of the computing is inversely proportional to the amount of processors. In practice, this inverse law is only valid for a small number of processors, and adding processors for a given number of grid points becomes less efficient. Searching for the optimal number of grid points per processor is a process called scalability study. We conducted such a study for the numerical code and found that an optimum could be reached around 256 processors for a 2 km $\times$ 2 km domain.
- After the resolution and scalability studies came the setting of the time step. With the explicit time scheme of the NHOES code, the time step

is controlled by the Courant–Friedrichs–Lewy (CFL) criterion, $\Delta t \leq c\frac{\Delta x}{U}$ where U is the the speed of the fastest propagating signal in the domain, Δt and Δx are the time step and the horizontal grid size, and c is a multiplicative constant of order 1, determined empirically. Several simulations of duration 1 or 2 inertial periods were conducted to adjust the time step (in practice, the time step was continuously raised, before entailing numerical instabilities, at which point we could decide on an optimum).

- Finally the viscosity and diffusivity amplitudes, in addition to their physical properties, are key features in controlling the numerical stability of the code. The aim was to lower their amplitude so as to better describe the physics of the problem while keeping large enough values to ensure stability. This process was made in the same way as the choice of the time step, and ended with the choice of $\nu = 1.10^{-1} m^2.s^{-1}$ and $\kappa = 1.10^{-2} m^2.s^{-1}$.

All these implementations have been carried out. However, due to lack of time, no extensive study was done yet, and only preliminary results are available. They are described in the last section of this chapter.

5.3 Analysis of the simulations

We describe here theoretical tools that are suitable for the study of three-dimensional wave-mean flow interactions.

5.3.1 Overview of the analysis

The three-dimensional numerical simulations were devised to thoroughly investigate wave-mean flow interactions in the case of a bottom reaching jet above topography. To analyze these simulations we might take interest in a variety of fields, scalar and vector. A first order investigation is performed which, although it remains qualitative, gives good ideas of the physics at play. We then focus on the energy reservoirs, energy transfers and energy dissipation in a zonal-mean

framework to compare with the two-dimensional studies. Finally, specific diagnostics are set up for investigating wave-mean flow interactions.

5.3.2 Energy reservoirs and fluxes

We first need the definition of a local (and a temporal) mean. We will note such a spatial mean as $\overline{(.)}$ and temporal mean as $\overline{(.)}^t$. We will not specify them any further yet, since many definitions can be used such as means over a constant depth, constant height over topography, along density contours, etc.

As stated in the previous paragraph, a first understanding of the three-dimensional cases can be achieved with the description of the motions of the fluid. The two-dimensional section presented a decomposition of the flow into two major motions: the slowly varying flow and the internal waves (the ILWs, the IOs and the waves produced by non linear interactions). As in the two-dimensional study, since the domain is smaller than R_d and periodic in the zonal direction, the mean flow and the inertial oscillations can be considered as being the only two fields that are non trivial after a zonal mean: $\overline{\mathbf{u}}^{E-W} = \mathbf{U_G} + \mathbf{U_{IO}}$, where $\overline{(.)}^{E-W}$ is a zonal mean, and $\mathbf{U_G}$ and $\mathbf{U}_{IO}$ are three-dimensional vectors in a two-dimensional $y-z$ plane, or equally they can be defined in the three-dimensional space but independent along the zonal direction. The mean flow and IOs can then be separated through temporal filtering: since the IOs oscillate at frequency $|f|$, $\mathbf{U}_{IO} = \overline{\mathbf{u}}^{E-W}|_{\omega=|f|\pm\partial\omega}$ where $\partial\omega$ is a prescribed width for the band-pass filter, and $\mathbf{U}_G = \overline{\mathbf{u}}^{E-W} - \mathbf{U}_{IO}$. From these calculations one can compute the ILW field: $\mathbf{u}' = \mathbf{u} - \overline{\mathbf{u}}^{E-W}$.

The energy reservoir can be seen through the energetic content of the fields stated above, while turbulent kinetic energy dissipation can be inferred from $\mathbf{u}'$ as in the two-dimensional study. The transfers of energy and tracers can be investigated thanks to turbulent fluxes: $\mathbf{F}(c) = \overline{\mathbf{u}'c'}$ where c is either a scalar or a component of a vector. Finally, the forcing of the mean flow by the waves can be

diagnosed through the Eliassen-Palm flux divergence, as shown in the previous section.

5.3.3 The Transformed-Eulerian Mean (TEM) framework

We now turn to the definition of averaging operators. The two-dimensional study discussed in previous chapters was conducted in an Eulerian framework: the mean used was a horizontal mean at constant height above bottom. Since we compared our two-dimensional results with those of Nikurashin and Ferrari (2010), it was logical to use the same framework. It is the most straightforward spatial averaging, but it has some serious drawbacks as soon as no homogeneity assumption can be made in the averaging direction. For instance, when the topography or the isopycnals are sloped in the averaging direction, the mean can exhibit velocities and fluxes (Kuo et al. 2005). But these can be artefacts that arise from the fact that the contours cross the iso-levels, and not from physical processes: for instance, the average depth of an iso-density contour is different from the depth of an iso-level of mean density. One must be particularly cautious of these artefacts when dealing with momentum fluxes and mean flow forcing, especially when they occur near non zonal features such as topography.

To avoid the artefacts that arise from the Eulerian mean, one can apply a gauge change to the horizontal mean with a "quasi-Stokes stream-function". The quasi-Stokes stream-function is defined in relation to buoyancy, which permits the concept of an average that accurately diagnoses momentum fluxes and wave-mean flow interactions. This change is the fundamental stepping stone of the Transformed Eulerian Mean (TEM, Plumb and Ferrari 2005). We will here attempt to describe this formalism.

The transformation consists in the change of the horizontal, Eulerian mean $\overline{(*)}^x$ into the transformed Eulerian mean $\overline{(*)}^\dagger$, where $*$ is the field to average. This change is made through the "quasi-Stokes stream-function" ψ that is not strictly defined since the gauge transformations have a degree of freedom:

- For the velocity fields: $\overline{\mathbf{u}}^{\dagger} = \overline{\mathbf{u}}^{x} + \nabla \wedge \mathbf{i}\psi$ where $\mathbf{i}$ is the unit vector in the direction of the flow (here, the x direction).
- Consistently, for scalar fields, the residual eddy flux is: $\overline{\mathbf{u}'\mathbf{s}'}^{\dagger} = \overline{\mathbf{u}'\mathbf{s}'}^{x} - \psi\mathbf{i} \wedge \nabla\overline{s}^{x}$.

The simplest definition of ψ for computing diapycnal and isopycnal fluxes is: $\psi = -|\nabla\overline{b}^{x}|^{-1}(\mathbf{s}.\overline{\mathbf{u}'b'}^{x})$ where $\mathbf{s}$ is a unit vector along the buoyancy contour. The mean current forcing equation becomes:

$$\overline{u}^{x}_{t} + (\overline{\mathbf{u}}^{\dagger}.\nabla)\overline{m}^{x} = -\nabla \cdot (\overline{\mathbf{u}'m'}^{x} - \psi\mathbf{i} \wedge \overline{m}^{x}) \tag{5.5}$$

where $m = u - \int f dy$ is the linear angular momentum per unit mass

As such, the TEM changes the definition of the spatial averages and of the eddy fluxes, but the governing equations are highly similar to those in the Eulerian mean framework. Although we developed TEM analysis tools for investigating the three-dimensional numerical simulations, time constraints did not allow for any application yet.

5.3.4 Preliminary results

A first simulation has been run, which provides some insight on the suitability of the setting devised in the first section of this chapter. This simulation was set with a ($L_x = 2$ km, $L_y = 2$ km) topography, the domain size being of 2 km in the zonal direction (with periodic conditions) and 3 km in the meridional direction (with open boundary conditions). Let us remind the reader that the flow was forced during the first 24h then the forcing was stopped and the flow could freely evolve.

Figure 5.3 depicts the general structure of the flow at the end of the simulation (after 11 inertial periods). Topography is shown in shades of copper. The top frame displays the velocity vectors taken in a $y - z$ plane situated at mid-ridge in the x direction, the domain is seen from South-East. The bottom frame displays contours of same velocity amplitude, and is seen from the West (the current flows away from the reader through the paper plane). As can be seen

on these frames, the zonal current at the end of the simulation varies with the vertical and meridional position considered. Away from the bottom and meridional boundaries, the flow typically reaches 0.1 $m.s^{-1}$, and is mostly oriented in the zonal direction, close to the original forced signal. When closer to the boundaries the flow intensity greatly diminishes, although it remains essentially directed in the zonal direction, apart from the area closest to the topographic feature.

Figure 5.4 displays iso-levels of the zonally averaged density along the zonal (left) and meridional (right) directions. An average at constant depth was used since it is the most straightforward and compares better with the previous results presented earlier in this manuscript. Dashed lines are the positions of the isopycnals at the beginning of the simulation, while the full lines represent the isopycnal positions at the end of the computation. Little or no change appears above 1000 m from the bottom, but closer to the topography the isopycnal surfaces become more distant, and present a meridional slope in the meridional direction. The widening of dense waters, and the disappearance of the densest waters points to a global lightening of the bottom waters of the domain. This suggests that the interaction of the flow with the topography, along with the boundary conditions, leads to a net mass transport out of the domain and the loss of energetic features close to topography. Although this affirmation would require a diagnostic of the mass transport out of the domain, we can relate this behavior to the description at the beginning of this chapter. Here $Fr \sim 0.8$, namely Fr is of order 1. Part of the densest waters flow around the topography, where no particular mechanism constrains the current to flow back in the center of the domain, and it will travel towards the meridional boundaries and eventually exit the domain (Nikurashin et al. 2014). The same process would happen continuously until the meridional component of the flow vanishes in the entirety of the domain. The net effect is an important loss of mass and energy of the flow.

Moreover, the apparition of a positive meridional mass gradient together

with the positive Coriolis frequency explains the positive vertical gradient in the geostrophic flow through the thermal wind, as explained previously. Since the upper part of the domain hardly feels the topography, this positive gradient is achieved by greatly decreasing the flow intensity near the bottom.

Figure 5.5 shows the time evolution of $\overline{\mathbf{u}}^x$ along a plane (top frame) 100 m above the top of the topography and along a line (bottom frame) situated in the center of the domain in the meridional (y) direction, 100 m above the top of the topography. As such, it should encapsulate the mean flow and inertial oscillations. After the forcing is stopped (at 24h), the zonal flow decreases exponentially directly above the topography and on the sides, and no inertial oscillations nor meridional flow are generated. Moreover, representations of the state of the flow at other times than at the very end of the simulation display similar features.

Analysis of momentum deposition through $\partial_z \overline{u'w'}^x$ was not yet conducted, although it appears that very little internal lee waves are emitted. Calculations of the bottom energy conversion rate indicated typical rates of less than 2.10^{-5} W.m^{-2}, and no internal lee wave was observed after the decrease of the bottom geostrophic flow. This behavior is expected, since the currents stop feeling the topographic feature. That in turn suggests that non linear wave-wave interactions are not at play, and explains why inertial oscillations do not grow.

This simulation is still under investigation in order to understand the disappearance of internal lee waves. A simple first step could be to perform a numerical simulation similar to the one discussed above, but with a continuous forcing that remains during the whole simulation, as in our two-dimensional simulation or in Nikurashin (2009). Doing so would provide knowledge on the separate effects of the lateral conditions and of the forcing, and should maintain the bottom reaching flow over the topography. Another experiment with no topographic feature could also be computed, to estimate the influence of mixing, bottom boundary interactions or of dissipative effects of the mean flow.

5.4 Conclusion

This chapter aimed at designing numerical simulations and introducing theoretical tools in order to investigate complex three-dimensional wave-mean flow interactions. We developed a strategy for this purpose: we define the physics expected to be at play, design the three-dimensional simulations, develop the numerical tools and describe a suitable theoretical framework for this case. We carried out one simulation, underwent a first analysis, and came to the conclusion that the mean flow is greatly influenced by the topography and meridional boundary conditions, leading to its baroclinisation and reduction above the topography, and hence to the disappearance of internal lee wave emission. It is unclear at this stage whether this three-dimensional configuration is an appropriate framework for tackling wave-wave and wave-mean flow interactions, although it does provide information on topography-mean flow interactions. We recommend researchers interested in further investigation to start off from this study, as it puts the basic stepping stones into place.

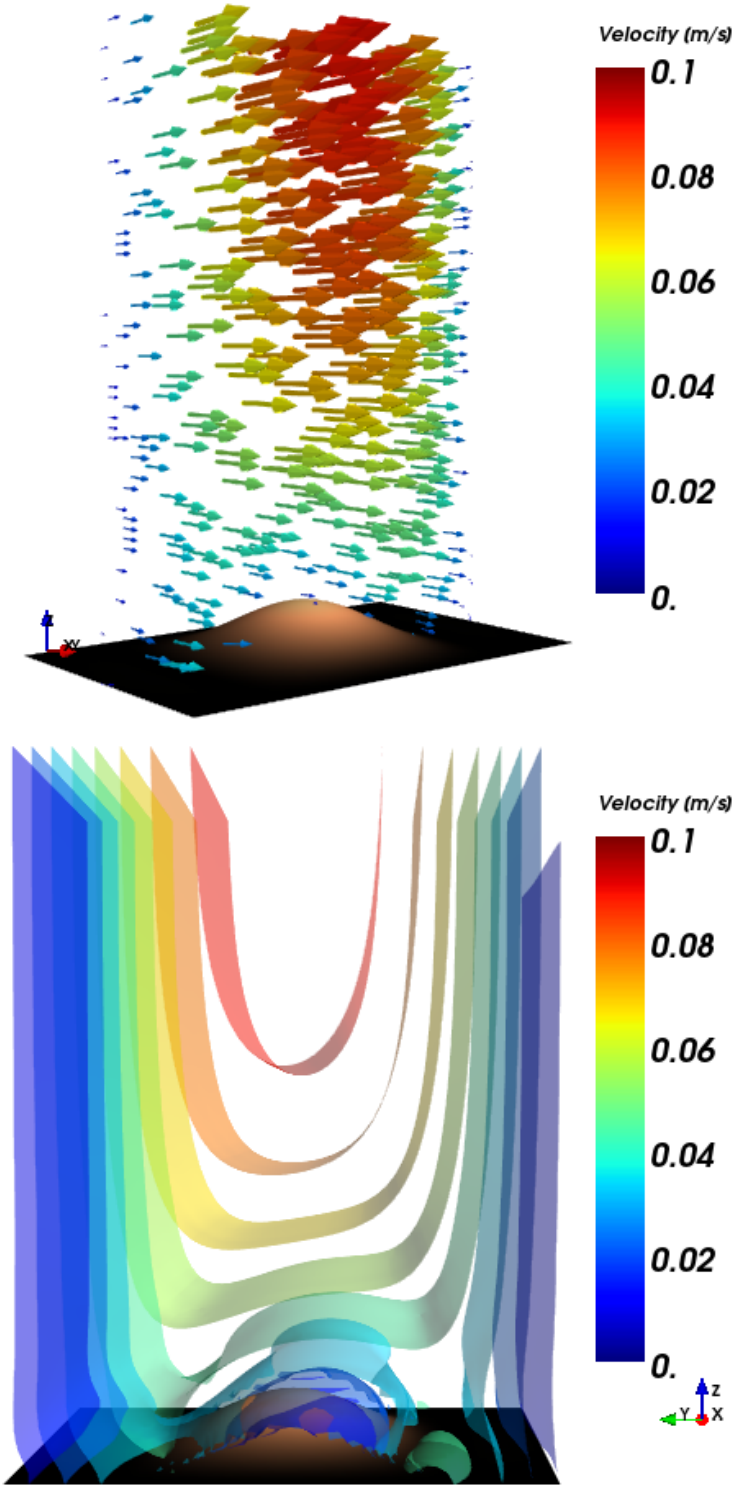

Figure 5.3 – *State of the flow at the end of the simulation (after 11 inertial periods) Top: vectors of* $\mathbf{u}$*, the mean current flows to the right. Bottom: iso-contours of* $\mathbf{u}$*, the mean current flows away from the reader into the paper.*

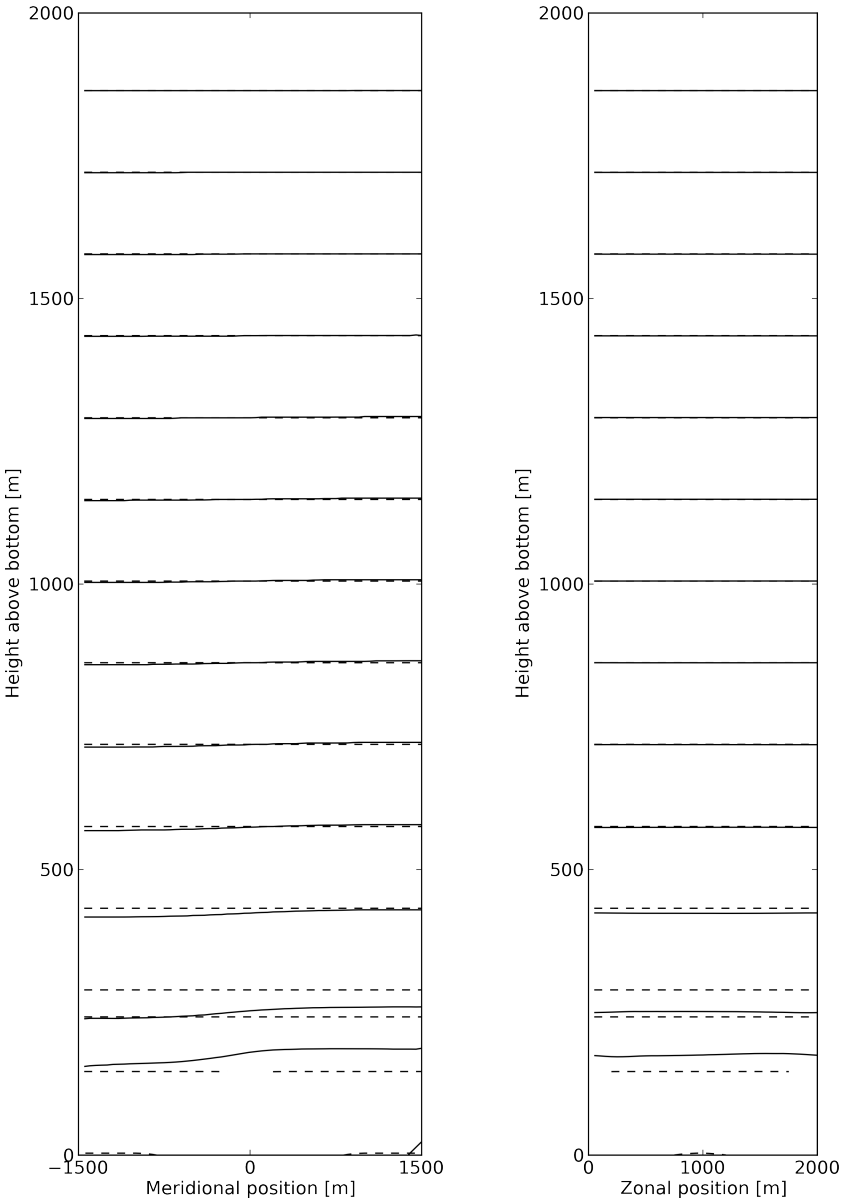

Figure 5.4 – *Iso-levels of the zonally averaged density along the zonal (left) and meridional (right) directions. Dashed lines are the positions of the isopycnals at the beginning of the simulation. Full lines represent the isopycnal positions at the end of the computation.*

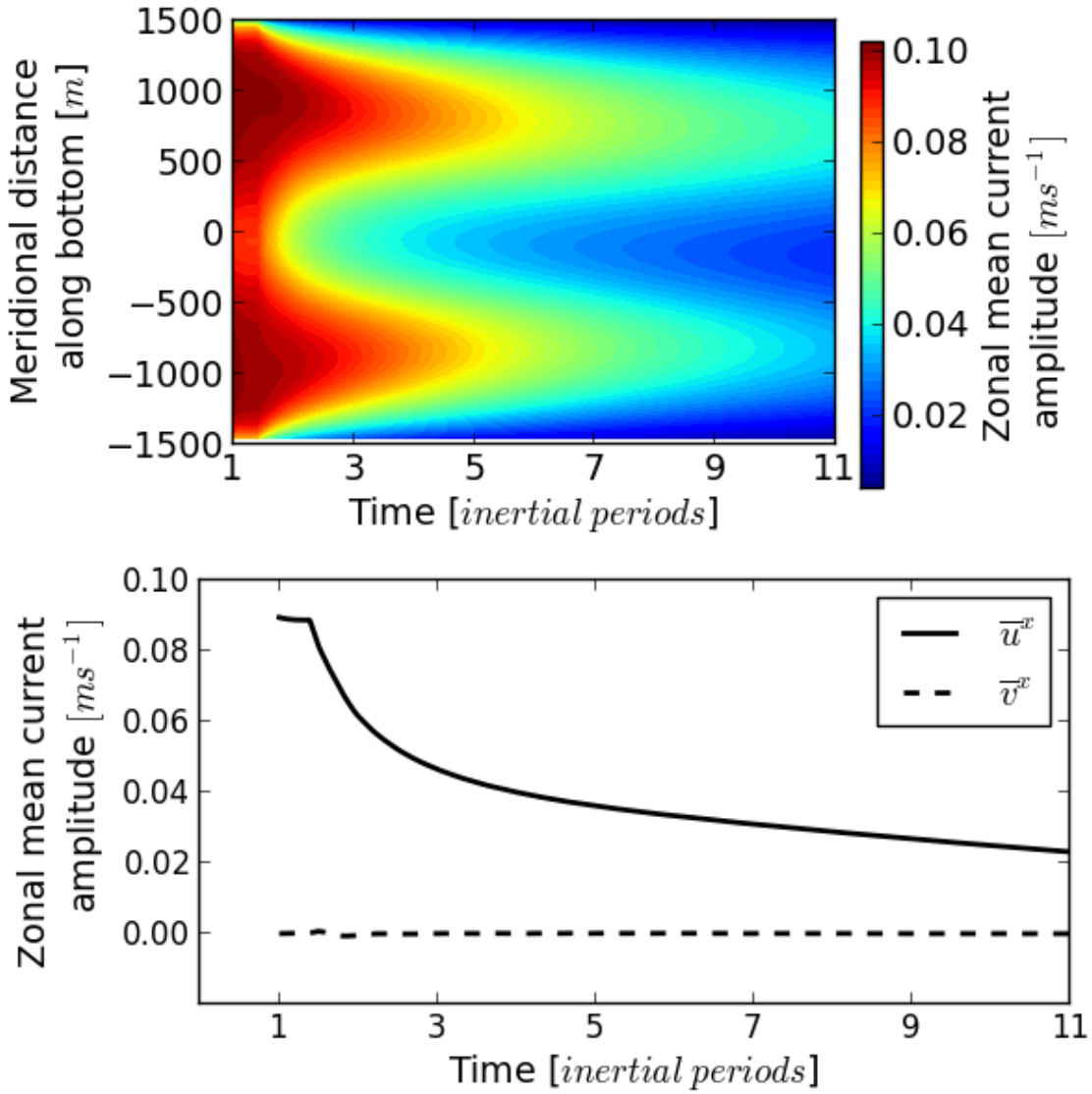

Figure 5.5 – *Time evolution of $\overline{\mathbf{u}}^x$ along a line 100 m above the top of the topography. Top frame encapsulates the meridional variation of $\overline{u}^x$, whereas the bottom frame represent the two horizontal components of $\overline{\mathbf{u}}^x$ computed along a line situated in the center of the domain in the meridional (y) direction. These fields should encapsulate the mean flow and inertial oscillations.*

Conclusions and perspectives

Summary of the main results

In this thesis, we have investigated the energy transfers involved in the interaction between a deep reaching current and bottom topography. To this end, a combination of two-dimensional numerical simulations and theoretical calculation were used, guided by on-field practice. We now sum up the main results up in the light of the four main questions raised in the introduction.

How are estimates of turbulent kinetic energy dissipation obtained, and under which conditions can these estimates be inferred?

Estimate of turbulent kinetic energy dissipation is currently obtained in many different ways, depending on the vertical and horizontal scales considered, with many different assumptions. The bibliographic review we performed allows to understand the different parameterisations and the underlying hypotheses and sheds light on the missing physical processes.

At centimeter scales the turbulent kinetic energy dissipation rate is directly measured through micro-structure casts, without the use of parameterization or important hypothesis. Since this type of measurement is subject to the least theoretical error, it is often considered as the 'true' level of turbulent kinetic energy dissipation rate. TKE dissipation rate can also be estimated from the velocity and density profiles at scales from ten to hundred meters from fine-scale parameterizations, using a nonlinear internal wave interaction model. This interaction model, usually a ray tracing model, has many assumptions, an important one being the fact that any process that *short circuits* the energy cascade is omitted.

Over the scale of the water column, ocean recipes predict TKE dissipation rates through the evolution of the wave field, from its emission to its dissipation rate by associating fine-scale parameterizations with emission mechanisms. On top of the flaws of the fine-scale parameterizations, the recipes rely on an *idealized topography*, the assumption that the waves are in a *steady medium* (which are two unlikely hypotheses), and *overestimate* the bottom energy conversion flux. Finally, global coverage of the ocean TKE dissipation has been attempted by combining knowledge of the ocean bottom and numerical outputs of the ocean state (flow speeds and stratification), which gives a global knowledge of emitted energy at the bottom of the ocean. The main drawback of this approach is that the *vertical dependency of the energy dissipation rate is constant and horizontally uniform* (it is the same whatever the horizontal location and the state of the fluid). Moreover, the estimate of the energy of the internal lee wave field relies on *linear, two-dimensional computations* and is thought to be overestimated.

What processes and energy reservoirs should be taken into account for understanding AABW consumption?

In the deep Southern Ocean, the AABW transformation rate is primarily subject to the internal lee wave field, which constitutes a major energy reservoir available for mixing (Nikurashin and Ferrari 2011). We used a wide combination of two-dimensional numerical simulations based on the setting proposed by Nikurashin and Ferrari (2010), reproducing typical Southern Ocean conditions. A strong internal lee wave field was observed to emerge on scales of a kilometer or less. A state of statistically steady energy dissipation rate was observed for cases of strong bathymetric amplitude. In the statistically steady state, about 10 to 30% of the internal lee wave kinetic energy is dissipated in the water column for our range of parameters and most of the turbulent kinetic energy dissipation is confined to a bottom layer. The thickness of this layer is not yet straightforwardly related to external parameters. Using a standard mixing efficiency ($\gamma = 0.2$, Klymak and Nash 2009), we estimate that a typical scenario

of internal lee wave breaking in the deep Southern Ocean would be associated with diapycnal diffusivity $K_z \sim 4.10^{-3}$ m^2 s^{-1} over the bottom 1000 m.

A three-dimensional setting was developed to investigate the impact of meridional gradients on the mechanisms at play. Preliminary results show that the deep reaching geostrophic current becomes sheared and decreases near the topography, while meridional mass gradients are formed. In this simulation, the internal wave activity is negligible, probably because of the weakening of geostrophic motions close to topography.

What is the role of inertial oscillations in the energy pathways of the internal lee waves?

In most of the numerical simulations we performed, inertial oscillations emerged, as did linear combinations of these waves and internal lee waves. This suggested strong coupling between these wave motions. Two theoretical approaches were used in an attempt to investigate the underlying mechanisms of this interaction. Thus, we extended to the vertical plane the asymptotic theory developed by Nikurashin and Ferrari (2010). This theory predicts an exponential growth of the inertial oscillations within certain depths under the fundamental condition that the medium is dissipative. After comparison with the behavior of the numerical simulations, it was deemed to be inadequate for explaining the physics at play.

We also used the resonant interaction theory to investigate nonlinear interactions among triads of internal waves. This theory predicted that the inertial oscillation amplitude can have an exponential growth even in the absence of dissipation, and gave a prediction of their rate of growth. Although the resonant interaction theory did not provide any information on the vertical dependency of the mechanism, it was found to give much better results in predicting the growth rate of the inertial oscillations than the asymptotic theory.

What are the respective roles of dissipative and non-dissipative interactions in the energy pathways?

We developed two theories as an attempt to explain the emergence of IOs. The generation of inertial oscillations is fundamentally dependent on dissipative effects (as well as non-linear effects) in one theory, the second theory being non-dissipative. The latter theory appeared to be the most relevant. That being the case entails that the energy dissipation rates observed were not the direct consequence of wave-wave interactions. The theory and the numerical simulations point out that the impact of this non-dissipative interaction mechanism might indirectly affect the internal lee wave breaking by providing short circuits in the energy cascade. An important consequence of this statement is that such a mechanism is not taken into account by current parameterizations.

Perspectives for future studies

This study investigated but an aspect amongst others of the presence of inertial oscillations in the abyssal ocean and their role in bottom kinetic energy dissipation. It calls for several future developments and we present here perspectives that would deserve further investigation.

Towards a three-dimensional description of internal lee wave-mean flow interactions

As shown in chapter 5, our two-dimensional numerical experiments fall a bit short at describing internal lee wave-mean flow interactions. Further development and investigation are needed to understand and quantify the full impacts of a three-dimensional bottom reaching flow on a (potentially isolated) topography. A better understanding of the fully three-dimensional energy transfers from the mean flow to the internal lee wave field is required to better account for the decrease of the internal lee wave field amplitude as observed in our three-dimensional simulation. Jointly, the baroclinisation of the mean flow above the

topography also requires future studies. To carry out these experiments might require to investigate a diversity of non-dimensional parameters built upon topographic amplitude or current strength for instance. Finally, looking for a steady state might not be suitable for investigating wave-mean flow interactions, and the lead may be in transitory states or intermittency for instance.

Towards an estimate of the global distribution of diapycnal mixing

Since existing fine-scale parameterizations do not account for energy cascade short circuits such as those presented in this manuscript, a great field of work is here for the taking. In the long term, a non-linear propagation model that incorporates mechanisms with discrete energy exchanges might prove to be a great boon for the ocean community and provide more accurate mixing estimates over the whole surface of the Southern Ocean (from fine- to global-scales). This could consist, for instance, in modifying the Radiation Balance Equation (see Chapter 1) so as to incorporate energy short circuits and triad interactions. Such a parameterization model could be done in a purely theoretical fashion as have been the existing propagation models. In the short term, investigations could also be made by joining knowledge of the mechanisms depicted here with a numerical ray tracing model. This would associate the knowledge of the impact of internal lee waves on the large scale flow with the feedback of the large scale flow, leading to a possible completion of the loop between internal waves, inertial oscillations and mean flow, and the possibility to infer the resulting turbulent kinetic energy dissipation rate.

Comparing the numerical and theoretical work with field measurements

There is so far no evidence from observations that the triad mechanism we discuss actually takes place in the Southern Ocean. To our knowledge, there is as yet no discussion either of field measurements of inertial oscillations in the deep Southern Ocean in the literature. However, progress could be made on this aspect by taking time records of the velocity near the bottom in places hosting

strong deep reaching currents and bottom topography, over rough terrain near a jet of the Antarctic Circumpolar Current for instance. By observing the amplitude and evolution of the internal lee wave field, as well as the inertial oscillation content, attempts could be made to track the generation of inertial oscillations, under the light of the resonant interaction theory. The energy spectrum of the flow could give indications on the presence of harmonics and linear combinations of the frequencies of these two main waves. In the case micro-structure profilers were deployed, times of strong turbulent kinetic energy dissipation could be compared to times of strong inertial oscillations, for instance. Finally, vertical profiles of all these measurements could indicate the possible upwards propagation of these motions, as well as inform on their bottom confinement. Recent ship deployments have recorded these different fields in the Southern Ocean (Sheen et al. 2013), promising a leap in diapycnal mixing understanding.

Annexes

A

A.1 Resonant interaction theory

This annex is a step by step guide through the resonant interaction theory derivation.

A.1.1 Deriving the resonant interaction theory

From Koudella and Staquet (2006), the fluid motion equations are written as

$$\partial_t \Delta\psi + J(\omega,\psi) = f\partial_z v + \partial_x \tilde{\rho} + \nu\Delta^2\psi \tag{A.1a}$$

$$\partial_t v + J(v,\psi) = -f\partial_z \psi + \nu\Delta v \tag{A.1b}$$

$$\partial_t \tilde{\rho} + J(\tilde{\rho},\psi) = -N^2\partial_x\psi + \kappa\Delta\tilde{\rho} \tag{A.1c}$$

After scaling the equations:

$$\partial_t \Delta\psi + FrJ(\Delta\psi,\psi) = \frac{f}{N}\partial_z v + \partial_x\rho + \frac{Fr}{Re}\Delta^2\psi \tag{A.2a}$$

$$\partial_t v + FrJ(v,\psi) = -\frac{f}{N}\partial_z\psi + \frac{Fr}{Re}\nu\Delta v \tag{A.2b}$$

$$\partial_t \rho + FrJ(\rho,\psi) = -\partial_x\psi + \frac{Fr}{RePr}\Delta\rho \tag{A.2c}$$

Use t_0 as a fast time-scale, of order N^{-1} and t_1 as slow time-scale of order $\frac{t_0}{Fr} \sim \frac{L}{U}$.

$$\partial_t = \partial_{t_0} + Fr\partial_{t_1} \tag{A.3a}$$

$$\partial_t^2 = \partial_{t_0}^2 + 2Fr\partial_{t_0}\partial_{t_1} + Fr^2\partial_{t_1}^2 \tag{A.3b}$$

One then gets:

$$\begin{aligned}(\partial_{t_0}^2 + 2Fr\partial_{t_0}\partial_{t_1} + Fr^2\partial_{t_1}^2)\Delta\psi + \psi_{xx} + (\frac{f}{n})^2\psi_{zz} = \\ - Fr(\partial_{t_0}J(\Delta\psi,\psi) + Fr\partial_{t_1}J(\Delta\psi,\psi)) \\ - FrJ(\rho,\psi)_x - Fr\frac{f}{N}J(v,\psi)_z \\ + \frac{Fr}{PrRe}\Delta\rho_x + \frac{Fr}{Re}(\Delta^2\psi_{t_0} + Fr\Delta^2\psi_{t_1}) + \frac{f}{N}\frac{Fr}{Re}\Delta v_z\end{aligned} \tag{A.4a}$$

$$\partial_{t_0}\rho + Fr\partial_{t_1}\rho + \partial_x\psi = -FrJ(\rho,\psi) + \frac{Fr}{PrRe}\Delta\rho \tag{A.4b}$$

$$\partial_{t_0} v + \frac{f}{N}\partial_z\psi = Fr(-J(v,\psi) + \frac{1}{Re}\Delta v) - Fr\partial_{t_1} v \tag{A.4c}$$

We then expand around the small parameter Fr:

$$\psi(\boldsymbol{x}, t_0, t_1) = \psi^0(\boldsymbol{x}, t_0, t_1) + Fr\psi^1(\boldsymbol{x}, t_0, t_1) + \mathcal{O}(Fr^2) \tag{A.5a}$$

$$\rho(\boldsymbol{x}, t_0, t_1) = \rho^0(\boldsymbol{x}, t_0, t_1) + Fr\rho^1(\boldsymbol{x}, t_0, t_1) + \mathcal{O}(Fr^2) \tag{A.5b}$$

$$v(\boldsymbol{x}, t_0, t_1) = v^0(\boldsymbol{x}, t_0, t_1) + Frv^1(\boldsymbol{x}, t_0, t_1) + \mathcal{O}(Fr^2) \tag{A.5c}$$

We get at order 0:

$$\partial_{t_0}^2 \Delta\psi^0 + \psi_{xx}^0 + (\frac{f}{N})^2 \psi_{zz}^0 = 0 \tag{A.6a}$$

$$\partial_{t_0}\rho^0 + \psi_x^0 = 0 \tag{A.6b}$$

$$\partial_{t_0} v^0 + \frac{f}{N}\partial_z \psi^0 \tag{A.6c}$$

The solution at order 0 consists in a superposition of plane waves. The first instability to happen occurs for the superposition of three waves, and gives fields of the form:

$$\psi^0(\boldsymbol{x}, t_0, t_1) = \sum_{j=0}^{2} A_i(t_1) e^{i\phi_i} + c.c. \tag{A.7a}$$

$$\rho^0(\boldsymbol{x}, t_0, t_1) = \sum_{j=0}^{2} \frac{k_i}{\omega_i} A_i(t_1) e^{i\phi_i} + c.c. \tag{A.7b}$$

$$v^0(\boldsymbol{x}, t_0, t_1) = \sum_{j=0}^{2} \frac{f}{N}\frac{m_i}{\omega_i} A_i(t_1) e^{i\phi_i} + c.c. \tag{A.7c}$$

Where

$$\phi_j = \boldsymbol{k_j}.\boldsymbol{x} - \omega_j t_0$$

$$\boldsymbol{k_j} = k_j \boldsymbol{e}_x + m_j \boldsymbol{e}_z$$

The expression at order 1 becomes quite tedious:

$$\begin{aligned} 0 = {} & 2\frac{\partial^2}{\partial_{t_0}\partial_{t_1}}\Delta\psi^0 + \frac{\partial}{\partial t_0} J(\psi^0, \Delta\psi^0) + \frac{\partial}{\partial x} J(\psi^0, \rho^0) \\ & + \frac{1}{Re}(\frac{1}{Pr}\frac{\partial}{\partial x}\Delta\rho^0 + \frac{\partial}{\partial t_0}\Delta^2\psi^0) + \frac{f}{N}\frac{\partial J(\psi^0, v^0)}{\partial z} + \frac{f}{N}\frac{1}{Re}\frac{\partial \Delta v^0}{\partial z} \end{aligned} \tag{A.8}$$

Careful development leads to:

$$\sum_{\sigma_l=\pm1}\sum_{l=0}^{2}\mathcal{F}_l+\sum_{\sigma_n=\pm1}\sum_{\sigma_p=\pm1}\sum_{n=0}^{2}\sum_{p=0}^{2}\mathcal{G}_{n,p}=0 \tag{A.9}$$

Where $\mathcal{F}_l$ regroups the linear terms and $\mathcal{G}_{n,p}$ the non-linear terms:

$$\mathcal{F}_l=-i\sigma_l K_l^2\omega_l e^{i\sigma_l\phi_l}\Big(2\frac{\partial A_l^{(\sigma_l)}}{\partial t_1}+\frac{1}{RePr}\frac{k_l^2}{\omega_l^2}A_l^{(\sigma_l)}+\frac{1}{Re}K_l^2A_l^{(\sigma_l)}-(\frac{f}{N})^2\frac{1}{Re}\frac{m_l^2}{\omega_l^2}A_l^{(\sigma_l)}\Big) \tag{A.10}$$

$$\begin{aligned}\mathcal{G}_{n,p}=&\,i\sigma_n\sigma_p(m_nk_p-m_pk_n)A_n^{(\sigma_n)}A_p^{(\sigma_p)}e^{i(\sigma_n\phi_n+\sigma_p\phi_p)}\\&\Big(K_p^2(\sigma_n\omega_n+\sigma_p\omega_p)+\frac{k_p}{\omega_p}(\sigma_nk_n+\sigma_pk_p)+(\frac{f}{N})^2\frac{m_p}{\omega_p}(\sigma_nm_n+\sigma_pm_p)\Big)\end{aligned} \tag{A.11}$$

where $A_j^{(1)}=A_j$ and $A_j^{(-1)}=A_j^*$.

Taking into account that $K_j^2\omega_j-(\frac{f}{N})^2\frac{m_j^2}{\omega_j}=\frac{k_j^2}{\omega_j}$ from the dispersion relation, the equations write:

$$\begin{aligned}&\sum_{\sigma_l=\pm1}\sum_l e^{i\sigma_l\phi_l}\Big[\sigma_lK_l^2\omega_l\Big(2\frac{\partial A_l^{(\sigma_l)}}{\partial t_1}+\frac{1}{Re}\frac{k_l^2}{\omega_l^2}(1+\frac{1}{Pr})A_l^{(\sigma_l)}\Big)\Big]\\&=\sum_{\substack{\sigma_n=\pm1\\\sigma_p=\pm1}}\sum_{n,p}e^{i(\sigma_n\phi_n+\sigma_p\phi_p)}\Big[\sigma_n\sigma_p(m_nk_p-m_pk_n)A_n^{(\sigma_n)}A_p^{(\sigma_p)}\\&\Big(K_p^2(\sigma_n\omega_n+\sigma_p\omega_p)+\frac{k_p}{\omega_p}(\sigma_nk_n+\sigma_pk_p)+(\frac{f}{N})^2\frac{m_p}{\omega_p}(\sigma_nm_n+\sigma_pm_p)\Big)\Big]\end{aligned} \tag{A.12}$$

From this equation, it follows that for the resonant interaction to occur, the waves need to satisfy:

$$\forall\{l,n,p\}\in\{0,1,2\}^3\backslash l\neq n\neq p,\quad\exists(\sigma_l,\sigma_n,\sigma_p)\in\{-1,1\}^3\backslash\sigma_l\phi_l=\sigma_n\phi_n+\sigma_p\phi_p \tag{A.13}$$

We can here choose the convention $\omega_j>0$ without any loss of information. The resonant condition can be written as:

$$\forall\{l,n,p\}\in\{0,1,2\}^3\backslash l\neq n\neq p,\quad\exists(\sigma_l,\sigma_n,\sigma_p)\in\{-1,1\}^3\backslash$$

$$\sigma_l \omega_l = \sigma_n \omega_n + \sigma_p \omega_p \tag{A.14a}$$

$$\sigma_l \boldsymbol{k}_l = \sigma_n \boldsymbol{k}_n + \sigma_p \boldsymbol{k}_p \tag{A.14b}$$

Injecting the resonant condition into A.12 holds:

$$\begin{aligned} K_l^2 \omega_l \Big(2\frac{\partial A_l^{(\sigma_l)}}{\partial t_1} + \frac{1}{Re}\frac{k_l^2}{\omega_l^2}(1+\frac{1}{Pr})A_l^{(\sigma_l)} \Big) &= \sigma_l \sigma_n \sigma_p (m_n k_p - m_p k_n) A_n^{(\sigma_n)} A_p^{(\sigma_p)} \\ &\Big(K_p^2(\sigma_n \omega_n + \sigma_p \omega_p) + \frac{k_p}{\omega_p}(\sigma_n k_n + \sigma_p k_p) + (\frac{f}{N})^2 \frac{m_p}{\omega_p}(\sigma_n m_n + \sigma_p m_p) \Big) \\ &- \Big(K_n^2(\sigma_n \omega_n + \sigma_p \omega_p) + \frac{k_n}{\omega_n}(\sigma_n k_n + \sigma_p k_p) + (\frac{f}{N})^2 \frac{m_n}{\omega_n}(\sigma_n m_n + \sigma_p m_p) \Big) \end{aligned} \tag{A.15a}$$

$$\begin{aligned} K_l^2 \omega_l \Big(2\frac{\partial A_l^{(\sigma_l)}}{\partial t_1} + \frac{1}{Re}\frac{k_l^2}{\omega_l^2}(1+\frac{1}{Pr})A_l^{(\sigma_l)} \Big) &= \\ \sigma_l \sigma_n \sigma_p (m_n k_p - m_p k_n) A_n^{(\sigma_n)} A_p^{(\sigma_p)} & \\ \Big(K_p^2(\sigma_l \omega_l) + \frac{k_p}{\omega_p}(\sigma_l k_l) + (\frac{f}{N})^2 \frac{m_p}{\omega_p}(\sigma_l m_l) & \\ - K_n^2(\sigma_l \omega_l) - \frac{k_n}{\omega_n}(\sigma_l k_l) - (\frac{f}{N})^2 \frac{m_n}{\omega_n}(\sigma_l m_l) \Big) & \end{aligned} \tag{A.15b}$$

$$\begin{aligned} K_l^2 \omega_l \Big(2\frac{\partial A_l^{(\sigma_l)}}{\partial t_1} + \frac{1}{Re}\frac{k_l^2}{\omega_l^2}(1+\frac{1}{Pr})A_l^{(\sigma_l)} \Big) &= \\ \sigma_n \sigma_p (m_n k_p - m_p k_n) A_n^{(\sigma_n)} A_p^{(\sigma_p)} & \\ \Big((K_p^2 - K_n^2)\omega_l + (\frac{k_p}{\omega_p} - \frac{k_n}{\omega_n})k_l + (\frac{f}{N})^2 (\frac{m_p}{\omega_p} - \frac{m_n}{\omega_n}) m_l \Big) & \end{aligned} \tag{A.15c}$$

Finally, the evolution equation for the amplitude is:

$$\begin{aligned} \frac{\partial A_l^{(\sigma_l)}}{\partial t_1} + \frac{1}{Re}\frac{k_l^2}{2\omega_l^2}(1+\frac{1}{Pr})A_l^{(\sigma_l)} &= \sigma_n \sigma_p A_n^{(\sigma_n)} A_p^{(\sigma_p)} \frac{(m_n k_p - m_p k_n)}{2K_l^2 \omega_l} \\ &\Big((K_p^2 - K_n^2)\omega_l + (\frac{k_p}{\omega_p} - \frac{k_n}{\omega_n})k_l + (\frac{f}{N})^2 (\frac{m_p}{\omega_p} - \frac{m_n}{\omega_n}) m_l \Big) \end{aligned} \tag{A.16}$$

Let us rewrite the two mains results from this section in a more general way

(in equations A.14 $\sigma_l \to -\sigma_l$, without any loss of generality):

$$\sigma_l\omega_l + \sigma_n\omega_n + \sigma_p\omega_p = 0 \tag{A.17a}$$

$$\sigma_l\boldsymbol{k}_l + \sigma_n\boldsymbol{k}_n + \sigma_p\boldsymbol{k}_p = 0 \tag{A.17b}$$

The final amplitude evolution equation becomes:

$$\frac{\partial A_l^{(\sigma_l)}}{\partial t_1} + \frac{1}{Re}\frac{k_l^2}{2\omega_l^2}(1+\frac{1}{Pr})A_l^{(\sigma_l)} = \sigma_n\sigma_p A_n^{(-\sigma_n)}A_p^{(-\sigma_p)}\frac{(m_n k_p - m_p k_n)}{2K_l^2\omega_l} \left((K_p^2 - K_n^2)\omega_l + (\frac{k_p}{\omega_p} - \frac{k_n}{\omega_n})k_l + (\frac{f}{N})^2(\frac{m_p}{\omega_p} - \frac{m_n}{\omega_n})m_l\right) \tag{A.18}$$

A.1.2 Calculation of the growth rate

Let us assume that wave o is originally of large amplitude (the ILWs), and serves as thermostat to to system (it provides energy, and its amplitude is subject to only small relative variations on timescales of order t_1). Waves 1 and 2 are originally of small amplitude, and grow thanks to the energy provided by wave 0.

From equation A.18, the set of amplitude evolution equation becomes:

$$\partial_{t_1}A_1^{(\sigma_1)} + C_1A_1^{(\sigma_1)} = S_1A_0^{(-\sigma_0)}A_2^{(-\sigma_2)} \tag{A.19a}$$

$$\partial_{t_1}A_2^{(\sigma_2)} + C_2A_2^{(\sigma_2)} = S_2A_0^{(-\sigma_0)}A_1^{(-\sigma_1)} \tag{A.19b}$$

where

$$C_i = \frac{1}{Re}\frac{k_i^2}{2\omega_i^2}(1+\frac{1}{Pr}) \tag{A.20a}$$

$$S_1 = \sigma_0\sigma_2\frac{(m_2k_0 - m_0k_2)}{2K_1^2\omega_1} \left((K_0^2 - K_2^2)\omega_1 + (\frac{k_0}{\omega_0} - \frac{k_2}{\omega_2})k_1 + (\frac{f}{N})^2(\frac{m_0}{\omega_0} - \frac{m_2}{\omega_2})m_1\right) \tag{A.20b}$$

$$S_2 = \sigma_0\sigma_1\frac{(m_1k_0 - m_0k_1)}{2K_2^2\omega_2} \left((K_0^2 - K_1^2)\omega_2 + (\frac{k_0}{\omega_0} - \frac{k_1}{\omega_1})k_2 + (\frac{f}{N})^2(\frac{m_0}{\omega_0} - \frac{m_1}{\omega_1})m_2\right) \tag{A.20c}$$

(A.20d)

Since $(C_1, C_2, S_1, S_2) \in \mathcal{R}^4$, we can rewrite equation A.19 as:

$$(\partial_{t_1} + C_2)(\partial_{t_1} + C_1)A_1 = S_1 S_2 |A_0|^2 A_1 \tag{A.21a}$$

$$(\partial_{t_1} + C_2)(\partial_{t_1} + C_1)A_2 = S_1 S_2 |A_0|^2 A_2 \tag{A.21b}$$

We can already deduce from equations A.21 that waves 1 and 2 are expected to have the same time evolution.

Let us consider $A_1(t_1) = A_1(0)e^{\Gamma t_1}$ and $A_2(t_1) = A_2(0)e^{\Gamma t_1}$, where Γ is the growth rate of the secondary waves. This entails:

$$\Gamma^2 + (C_1 + C_2)\Gamma + C_1 C_2 - S_1 S_2 |A_0|^2 = 0 \tag{A.22}$$

The secondary waves shall grow if Γ is real and positive, which occurs if

$$\Delta_\Gamma = (C_1 + C_2)^2 - 4(C_1 C_2 - S_1 S_2 |A_0|^2) > 0 \tag{A.23}$$

If this is the case, the exponential growth rate of the waves is:

$$\Gamma = \frac{1}{2}\Big(- (C_1 + C_2) + \sqrt{(C_1 + C_2)^2 + 4 S_1 S_2 |A_0|^2}\Big) \tag{A.24}$$

Note that $|A_0|$ is the complex amplitude of the primary wave, which is double its real amplitude.

Let us neglect dissipation ($Re \to \infty$). Getting back to dimensional parameters, the growth rate of the secondary waves becomes:

$$\Gamma^2 = \alpha C_{01} C_{02} \tag{A.25}$$

where α would be a total growth rate prefactor, and C_{01} and C_{02} would be interaction coefficients between the primary and secondary waves:

$$\alpha = \sigma_1 \sigma_2 \frac{(m_2 k_0 - m_0 k_2)}{K_1^2 \omega_1} \frac{(m_1 k_0 - m_0 k_1)}{K_2^2 \omega_2} |A_0^{\mathcal{R}}|^2 \tag{A.26a}$$

$$C_{01} = \Big((K_0^2 - K_1^2)\omega_2 + N^2 (\frac{k_0}{\omega_0} - \frac{k_1}{\omega_1}) k_2 + f^2 (\frac{m_0}{\omega_0} - \frac{m_1}{\omega_1}) m_2 \Big) \tag{A.26b}$$

$$C_{02} = \Big((K_0^2 - K_2^2)\omega_1 + N^2 (\frac{k_0}{\omega_0} - \frac{k_2}{\omega_2}) k_1 + f^2 (\frac{m_0}{\omega_0} - \frac{m_2}{\omega_2}) m_1 \Big) \tag{A.26c}$$

Note that $A_0^{\mathcal{R}} = \frac{|A_0|}{2}$ is the real amplitude of the waves.

A.2 Asymptotic theory, from Nikurashin and Ferrari (2010) and more

This annex is a step by step guide through the asymptotic theory derivation, while keeping track of the vertical coordinate.

A.2.1 Summary of Nikurashin and Ferrari (2010)

Let $\boldsymbol{u} = (u, v)$ and w be, respectively, the horizontal and vertical velocities, p the pressure fluctuation with respect to hydrostatic balance, $b = -g(\rho - \rho_0)/\rho_0$ the buoyancy, and ρ_0 the reference density. We assume that fluid motions are governed by the Boussinesq equations:

$$\boldsymbol{u}_t + (\boldsymbol{u}.\boldsymbol{\nabla}_H) \cdot \boldsymbol{u} + w\boldsymbol{u}_z + f\hat{\boldsymbol{z}} \wedge \boldsymbol{u} = -\boldsymbol{\nabla}_H p + \mathcal{D}_m(\boldsymbol{u}) \tag{A.27a}$$

$$w_t + (\boldsymbol{u}.\boldsymbol{\nabla}_H)w + ww_z = -p_z + b + \mathcal{D}_m(w) \tag{A.27b}$$

$$b_t + (\boldsymbol{u}.\boldsymbol{\nabla}_H)b + wb_z + wN^2 = \mathcal{D}_b(b) \tag{A.27c}$$

$$\boldsymbol{\nabla}_H \cdot \boldsymbol{u} + w_z = 0 \tag{A.27d}$$

with boundary conditions:

$$w|_{z=h(x)} = \boldsymbol{u}\boldsymbol{\nabla}_H h(x) \text{ and } w|_{z\to\infty} = 0 \tag{A.28}$$

In these equations a subscript refers to a partial derivative and $\mathcal{D}_{m,b}$ are the viscous and diffusive operators.

Thorough dimensional analysis (Nikurashin and Ferrari 2010) allows to rewrite equations (A.27a) to (A.28) in terms of dimensionless variables and fields, the dimensionless equations depending upon the Rossby number associated with the geostrophic flow and upon the steepness of the waves

$$\epsilon = Nh_T/U_G. \tag{A.29}$$

Assuming that ϵ is a small parameter, the fields and variables are expanded in powers of ϵ. Assuming also that the zero order flow is a superposition of the

geostrophic flow $\boldsymbol{U}_G$ and the inertial oscillations $\boldsymbol{U}_{IO}$, these expansions are of the form:

$$\boldsymbol{u} = \boldsymbol{u}_G + \boldsymbol{u}_{IO} + \sum_{i=1}^{\infty} \epsilon^i \boldsymbol{u}^{(i)} \tag{A.30a}$$

$$(w, b, p) = w_G + w_{IO} + \sum_{i=1}^{\infty} \epsilon^i (w^{(i)}, b^{(i)}, p^{(i)}) \tag{A.30b}$$

$$\boldsymbol{x} = \sum_{i=0}^{\infty} \epsilon^{-i} \boldsymbol{X}^{(i)} \tag{A.30c}$$

$$t = \sum_{i=0}^{\infty} \epsilon^{-i} T^{(i)} \tag{A.30d}$$

where $[T^{(0)}, \boldsymbol{X}^{(0)}]$ are the scales of the waves and $[T^{(i)}, \boldsymbol{X}^{(i)}]$ are slower and larger scales of the problem. Physical arguments imply that $\boldsymbol{U}_G$ varies on scales $[T^{(4)}, \boldsymbol{X}^{(4)}]$ or larger. As well, the forcing of the IOs by the vertical divergence of the lee wave momentum flux, as shown below, implies that $\boldsymbol{U}_{IO}$ varies on scales $[T^{(3)}, X^{(4)}, Y^{(4)}, Z^{(1)}]$. The $\boldsymbol{u}^{(i)}$ are higher-order motions depending on all scales of the problem. Note that IOs are present at all orders, being dominant at zero order. At each order, the evolution equation of the IOs is obtained by averaging over the small spatial scale $X^{(0)}$.

The latter scaling also relies on the assumption that the Rossby number is of the order of ϵ^4, to have a clear separation between the different components of the motion. Collecting terms with the same power of ϵ, one gets equations at different orders in ϵ. Since the evolution of the IO field in the slow time scale $T^{(3)}$ is seeked for, one needs to write these equations up to third order.

Equations at order 0 averaged over the small spatial scales describe the geostrophic balance satisfied by $\boldsymbol{U}_G$ and the fast time scale evolution of the IOs (namely oscillations at inertial frequency).

Writing the equations at order 1 and 2 and performing the same spatial average does not exhibit information on the IOs. This is expected since there is no forcing in the equations and the IO field is zero at the initial time. Equation at order 1 is also solved before averaging to obtain the expressions of the internal wave field generated by the zero-order motions (geostrophic flow and IOs) in-

teracting with bottom topography. These expressions are required to compute the IO field, as shown below.

At third order, averaging again over the small spatial scales, the momentum equation is:

$$\overline{\boldsymbol{u}^{(3)}_{T^{(0)}}} + f\hat{\boldsymbol{z}} \wedge \overline{\boldsymbol{u}^{(3)}} = -\partial_{T^{(3)}}\boldsymbol{u}_{IO} - \partial_{Z^{(1)}}\overline{\boldsymbol{u}^{(1)}w^{(1)}} + \mathcal{D}^{(3)}_m\left[\overline{\boldsymbol{u}^{(3)}}\right] \tag{A.31}$$

As pointed out by Nikurashin and Ferrari (2010), this equation involves a fast-time evolution of the IOs at third order, $\overline{\boldsymbol{u}^{(3)}_{T^{(0)}}}$, as well as a slow time evolution of the IO at zero order, $\partial_{T^{(3)}}\boldsymbol{u}_{IO}$. The IOs are forced by the vertical convergence of the wave momentum flux (hereafter referred to as momentum deposition), whose expression is provided by the solving of equations at first order as discussed above.

For mathematical tractability, a linear damping is used for dissipation:

$$\mathcal{D}^{(i)}_m\left(\boldsymbol{u}^{(i)}\right) = -\lambda\boldsymbol{u}^{(i)} \text{ and } \mathcal{D}^{(i)}_b\left(b^{(i)}\right) = -\lambda b^{(i)} \tag{A.32}$$

where (i) refers to the order of the equation and λ is the damping rate.

Introducing the complex variables $\mathcal{V}^{(3)} = u^{(3)} + iv^{(3)}$ and $\mathcal{V}_{IO} = u_{IO} + iv_{IO}$, Eq. (A.31) becomes:

$$\overline{\mathcal{V}^{(3)}_{T^{(0)}}} + if\overline{\mathcal{V}^{(3)}} + \lambda\overline{\mathcal{V}^{(3)}} = -\partial_{T^{(3)}}\mathcal{V}_{IO} - \partial_{Z^{(1)}}\overline{\mathcal{V}^{(1)}w^{(1)}} \tag{A.33}$$

Up to this point, the derivation is similar to that of Nikurashin and Ferrari (2010). Writing the IO field at zero-order as $\mathcal{V}^{IO} = U^{IO}(Z^{(1)}, T^{(3)})e^{-if(T^{(0)}-t_1)}$ where we introduce the phase of the IOs, ft_1, one gets:

$$\overline{\mathcal{V}^{(3)}_{T^{(0)}}} + if\overline{\mathcal{V}^{(3)}} + \lambda\overline{\mathcal{V}^{(3)}} = -(\partial_{T^{(3)}}U_{IO} + ifU_{IO}\frac{\partial t_1}{\partial T^{(3)}})e^{-if(T^{(0)}-t_1)} - \partial_{Z^{(1)}}\overline{\mathcal{V}^{(1)}w^{(1)}}. \tag{A.34}$$

For the multi-scale development to remain valid, the terms oscillating at frequency $-f$ on the left hand side have to vanish, thus:

$$(\partial_{T^{(3)}}U_{IO} + ifU_{IO}\frac{\partial t_1}{\partial T^{(3)}})e^{-if(T^{(0)}-t_1)} + \partial_{Z^{(1)}}\overline{\mathcal{V}^{(1)}w^{(1)}}\big|_{\omega=-f} = 0 \tag{A.35}$$

As shown by Nikurashin and Ferrari (2010) for $z = 0$, the solving of the equations at order 1 yields, assuming $\beta = U_I k_T / f$ is a small parameter:

$$\partial_{Z^{(1)}} \overline{\mathcal{V}^{(1)} w^{(1)}} = A + \beta(Be^{-if(T^{(0)}-t_0)} + Ce^{if(T^{(0)}-t_0)}) + \mathcal{O}(\beta^2) \tag{A.36}$$

where ft_0 is the phase of the wave momentum deposit, and A, B and C are constant. Eq. (A.36) is also valid in the water column, A, B and C being then depth-dependent functions.

Taking the real part of Eq.(A.35) yields, using Eq.(A.36):

$$\partial_{T^{(3)}} U_{IO} = \Re(\aleph) U_{IO} \tag{A.37}$$

where

$$\aleph(\lambda, \beta, t_1 - t_0, z) = -\frac{k_T}{f} Be^{-if(t_1-t_0)} \tag{A.38}$$

depends both on z and on the IO amplitude through the function B. In Eq. (A.37), $\Re(\aleph)$ is therefore the growth rate of the IOs. In the following, this growth rate is referred to as Γ.

A.2.2 Moving on from Nikurashin and Ferrari (2010)

In this subsection, we continue to follow the line of thought of Nikurashin and Ferrari (2010) while keeping track of the vertical structure of the IOs. We also consider that the phase of the IOs, ft_1, is distinct from that of the momentum deposit, ft_0, in contrast with Nikurashin and Ferrari (2010).

The phase difference $f(t_1 - t_0)$ can be estimated from Fig. 3.1. Fig. 3.1 is indeed a depth-time diagram for the $H_{20}L_{2\_}f$ simulation displaying the longitudinal component of the IOs and the regions associated with positive wave momentum deposit ($-\partial_z \overline{u'w'}^x > 0$). One notices that the IO maxima are in phase with the momentum deposit at all times, implying that Nikurashin and Ferrari (2010) were not off the mark:

$$\boxed{f(t_1 - t_0) = 0} \tag{A.39}$$

This can be seen for all simulations, except for $h_T = 80$ m, where the signal gets rapidly very noisy with little vertical correlation.

Assuming $f/U_G k_T$ and $\lambda/U_G k_T$ are small parameters (as β), the computation of the vertical and parametric dependency of the growth rate of the IOs yields:

$$\Gamma = \Gamma_0.\big(\cos(\phi z) + \frac{4.\lambda^2 - f^2}{4\lambda f}\sin(\phi z)\big) + \mathcal{O}(\frac{f^2}{U_G^2 k_T^2}, \frac{\lambda^2}{U_G^2 k_T^2}, \beta) \tag{A.40}$$

where $\phi = -Nf/U_G^2 k_T$, and

$$\boxed{\Gamma_0 = \frac{f^2}{U_G^2 k_T^2}\epsilon^2\lambda\big(1 + 4\frac{f^2}{U_G^2 k_T^2} - 6\frac{\lambda^2}{U_G^2 k_T^2}\big)} \tag{A.41}$$

Γ_0 is defined as the value of Γ at $z = 0$. Expression (A.41) differs from that found by Nikurashin and Ferrari (2010) by a factor $2\big(\frac{f}{U_G k_T}\big)^2$, which in the parameter range of the simulations is similar to 0.2. This may explain the fit of $\lambda = 10^{-4}$ s^{-1} found from the simulations, and used in Fig. 3.3.

The vanishing of Γ at some level z implies that the IO amplitude cannot grow at that level, and therefore reach a constant amplitude at that level. In what follows situations with $\Gamma = 0$ are said to be saturated. Note that if $\Gamma_0 = 0$, then saturation is reached at all depth. Interestingly, the parametric function Γ indicates that for a given z certain combinations of λ (Rayleigh dissipation rate) and β (IO amplitude) can cause saturation of IOs.

Note that positive value of Γ_0 imply that the IOs will grow somewhere in the water column near the topography. One can conjecture that during the non linear evolution of the flow described in Fig. (2.2), the effective dissipation rate and IO amplitude can also reach states such that the IOs no longer grow.

A.2.3 Vertical structure and propagation of inertial oscillations

In order to predict the height over which IOs grow, we compute the location at which the growth rate changes sign, separating exponentially growing and decaying IOs. This height is denoted as h_c.

Writing that Γ vanishes yields, using Eq. (A.41) at first order:

$$\phi h_c = \tan^{-1}(\frac{4\lambda f}{f^2 - 4.\lambda^2}) + n\pi \text{ , for any n.} \tag{A.42}$$

Nikurashin and Ferrari (2010) found from linear regression that $\lambda \sim 510^{-5}$ $s^{-1} \sim f/2$. This expression then becomes $\phi h_c = n\pi/2$, hence one finds:

$$\boxed{h_c = \pi \frac{U_G^2 k_T}{2Nf}} \tag{A.43}$$

The scale h_c is the vertical scale of the IOs. The IO amplitude decreases above h_c as the growth rate becomes negative. In our computations, h_c is close to 500 m for the L_2 cases, and to 800 m for the $L_{1.2}$ cases.

Bibliography

Adcroft, A., C. Hill, and J. Marshall, 1997: Representation of topography by shaved cells in a height coordinate ocean model. *Monthly Weather Review*, **125 (9)**, 2293–2315. (Cité page 99.)

Aiki, H. and T. Yamagata, 2004: A numerical study on the successive formation of meddy-like lenses. *Journal of Geophysical Research: Oceans (1978–2012)*, **109 (C6)**. (Cité pages 99 and 101.)

Andrews, D. and M. McIntyre, 1978: Generalized eliassen-palm and charney-drazin theorems for waves in axismmetric mean flows in compressible atmospheres. *Journal of the Atmospheric Sciences*, **35 (2)**, 175–185. (Cité pages 85, 95, and 98.)

Auclair, F., C. Estournel, J. W. Floor, M. Herrmann, C. Nguyen, and P. Marsaleix, 2011: A non-hydrostatic algorithm for free-surface ocean modelling. *Ocean Modelling*, **36 (1–2)**, 49–70, doi:10.1016/j.ocemod.2010.09.006. (Cité page 34.)

Bell, T., 1975: Lee waves in stratified flows with simple harmonic time dependence. *J. Fluid Mech*, **67 (4)**, 705–722. (Cité pages 23, 38, and 58.)

Bergh, J., 2010: Nonhydrostatic pressure in ocean models with focus on wind driven internal waves. Ph.D. thesis, Ph. D. thesis, University of Bergen. Available at: https://bora. uib. no/bitstream/1956/3960/2/Dr. thesis_Jonpdf. (Cité page 36.)

Booker, J. R. and F. P. Bretherton, 1967: The critical layer for internal gravity waves in a shear flow. *Journal of Fluid Mechanics*, **27 (03)**, 513–539. (Cité page 11.)

Brearley, J. A., K. L. Sheen, A. C. Naveira Garabato, D. A. Smeed, and S. N. Waterman, 2013: Eddy-induced modulation of turbulent dissipation over rough topography in the southern ocean. *Journal of Physical Oceanography*. (Cité pages 42 and 45.)

Bühler, O., 2014: A gentle stroll through ep flux theory. *European Journal of Mechanics-B/Fluids*. (Cité page 95.)

Carter, G. and J. Imberger, 1986: Vertically rising microstructure profiler. *Journal of Atmospheric and Oceanic Technology*, **3 (3)**, 462–471. (Cité page 18.)

Chen, X. and K.-K. Tung, 2014: Varying planetary heat sink led to global-warming slowdown and acceleration. *Science*, **345 (6199)**, 897–903. (Cité page 3.)

Chow, C. C., D. Henderson, and H. Segur, 1996: A generalized stability criterion for resonant triad interactions. *Journal of Fluid Mechanics*, **319**, 67–76. (Cité page 79.)

Ferrari, R. and C. Wunsch, 2009: Ocean circulation kinetic energy: Reservoirs, sources, and sinks. *Annual Review of Fluid Mechanics*, **41 (1)**, 253–282, doi:10.1146/annurev.fluid.40.111406.102139. (Cité pages 6, 11, and 20.)

Garcia, R. R. and B. A. Boville, 1994: "downward control" of the mean meridional circulation and temperature distribution of the polar winter stratosphere. *Journal of the atmospheric sciences*, **51 (15)**, 2238–2245. (Cité page 96.)

Goff, J. A. and T. H. Jordan, 1988: Stochastic modeling of seafloor morphology: Inversion of sea beam data for second-order statistics. *Journal of Geophysical Research: Solid Earth (1978–2012)*, **93 (B11)**, 13 589–13 608. (Cité page 24.)

Goldstein, H., 1980: *Classical mechanics*. Addison-Wesley Pub. Co. (Cité page 56.)

Hasselmann, K., 1967: A criterion for nonlinear wave stability. *Journal of Fluid Mechanics*, **30 (04)**, 737–739. (Cité page 83.)

Haynes, P., M. McIntyre, T. Shepherd, C. Marks, and K. P. Shine, 1991: On the "downward control" of extratropical diabatic circulations by eddy-induced mean zonal forces. *Journal of the Atmospheric Sciences*, **48 (4)**, 651–678. (Cité page 96.)

IPCC, 2014: *Climate Change 2013: the Physical Science Basis: Working Group I Contribution to the IPCC Fifth Assessment Report*. Cambridge University Press. (Cité page 3.)

Ito, T. and J. Marshall, 2008: Control of lower-limb overturning circulation in the southern ocean by diapycnal mixing and mesoscale eddy transfer. *Journal of Physical Oceanography*, **38 (12)**, 2832–2845, doi:10.1175/2008JPO3878.1. (Cité page 26.)

Jayne, S. R., 2009: The impact of abyssal mixing parameterizations in an ocean general circulation model. *Journal of Physical Oceanography*, **39 (7)**, 1756–1775. (Cité pages 26 and 27.)

Klymak, J. M. and J. D. Nash, 2009: Estimates of mixing. *Encyclopedia of Ocean Sciences*, J. H. Steele, K. K. Turekian, and S. A. Thorpe, Eds., Academic Press, chap. Estimates of Mixing, 3696–3706. (Cité page 118.)

Koudella, C. and C. Staquet, 2006: Instability mechanisms of a two-dimensional progressive internal gravity wave. *Journal of Fluid Mechanics*, **548**, 165–196. (Cité pages 40, 74, and 127.)

Kuo, A., R. A. Plumb, and J. Marshall, 2005: Transformed eulerian-mean theory. part ii: Potential vorticity homogenization and the equilibrium of a wind-and buoyancy-driven zonal flow. *Journal of physical oceanography*, **35 (2)**, 175–187. (Cité page 107.)

Lavergne, C. D., G. Madec, J. Le Sommer, G. Nurser, and A. Naveira-Garabatto, submitted: On the consumption of antarctic bottom water in the abyssal ocean. *Journal of Physical Oceanography*. (Cité pages 10 and 27.)

Lesieur, M., 1990: Turbulence in fluids, 412 pp. Kluwer Acad., Norwell, Mass. (Cité page 40.)

Lott, F., 2003: Large-scale flow response to short gravity waves breaking in a rotating shear flow. *Journal of the atmospheric sciences*, **60 (14)**, 1691–1704. (Cité page 96.)

Marsaleix, P., F. Auclair, C. Estournel, C. Nguyen, and C. Ulses, 2011: An accurate implementation of the compressibility terms in the equation of state in a low order pressure gradient scheme for sigma coordinate ocean models. *Ocean Modelling*, **40 (1)**, 1–13. (Cité page 99.)

Marshall, D. P. and A. C. Naveira Garabato, 2008: A conjecture on the role of bottom-enhanced diapycnal mixing in the parameterization of geostrophic eddies. *Journal of Physical Oceanography*, **38 (7)**, 1607–1613, doi:10.1175/2007JPO3619.1. (Cité page 26.)

Melet, A., R. Hallberg, S. Legg, and M. Nikurashin, 2014: Sensitivity of the ocean state to lee wave driven mixing. *Journal of Physical Oceanography*, **submitted**. (Cité page 26.)

Melet, A., R. Hallberg, S. Legg, and K. Polzin, 2013: Sensitivity of the ocean state to the vertical distribution of internal-tide-driven mixing. *Journal of Physical Oceanography*, **43 (3)**, 602–615. (Cité pages 26 and 27.)

Monvoisin, R., 2007: Pour une didactique de l'esprit critique-zététique et utilisation des interstices pseudoscientifiques dans les médias. Ph.D. thesis, Université Joseph-Fourier-Grenoble I. (Cité page 84.)

Muench, J. E. and E. Kunze, 1999: Internal wave interactions with equatorial deep jets. part i: Momentum-flux divergences. *Journal of physical oceanography*, **29 (7)**, 1453–1467. (Cité page 95.)

Munk, W. and C. Wunsch, 1998: Abyssal recipes ii: energetics of tidal and wind mixing. *Deep-Sea Research Part I*, **45 (12)**, 1977–2010. (Cité page 7.)

Munk, W. H., 1966: Abyssal recipes. *Deep Sea Research and Oceanographic Abstracts*, Elsevier, Vol. 13, 707–730. (Cité pages 4 and 6.)

Naveira Garabato, A., 2009: Rrs james cook cruise 29, 01 nov-22 dec 2008. sofine cruise report: Southern ocean finestructure. Tech. rep., British Antarctic Survey, Cambride, United Kingdom. (Cité page 25.)

Naveira Garabato, A. C., A. G. Nurser, R. B. Scott, and J. A. Goff, 2013: The impact of small-scale topography on the dynamical balance of the ocean. *Journal of Physical Oceanography*, **43 (3)**, 647–668. (Cité page 95.)

Newton, I., 1726: Naturalis philosophiae principia mathematica. *London (1687)*. (Cité page 84.)

Nikurashin, M., 2009: Radiation and dissipation of internal waves generated by geostrophic motions impinging on small-scale topography. Ph.D. thesis, MIT/Woods Hole. (Cité pages 93, 100, 101, 103, and 110.)

Nikurashin, M. and R. Ferrari, 2010: Radiation and dissipation of internal waves generated by geostrophic motions impinging on small-scale topography: Theory. *Journal of Physical Oceanography*, **40 (5)**, 1055–1074, doi: 10.1175/2009JPO4199.1. (Cité pages 11, 12, 14, 33, 39, 42, 43, 45, 55, 56, 57, 60, 85, 107, 118, 119, 133, 135, 136, 137, and 138.)

Nikurashin, M. and R. Ferrari, 2011: Global energy conversion rate from geostrophic flows into internal lee waves in the deep ocean. *Geophysical Research Letters*, **38 (8)**, L08 610. (Cité pages 6, 11, and 118.)

Nikurashin, M., R. Ferrari, N. Grisouard, and K. Polzin, 2014: The impact of finite-amplitude bottom topography on internal wave generation in the southern ocean. *Journal of Physical Oceanography*. (Cité pages 24, 44, 94, and 109.)

Nikurashin, M., G. Vallis, and A. Adcroft, 2012: Routes to energy dissipation for geostrophic flows in the southern ocean. *Nature Geoscience*, **6 (1)**, 48–51. (Cité page 28.)

Oka, A. and Y. Niwa, 2013: Pacific deep circulation and ventilation controlled by tidal mixing away from the sea bottom. *Nature communications*, **4**. (Cité page 28.)

Olbers, D. and C. Eden, 2013: A global model for the diapycnal diffusivity induced by internal gravity waves. *Journal of Physical Oceanography*. (Cité pages 20 and 24.)

Osborn, T. R., 1980: Estimates of the local rate of vertical diffusion from dissipation measurements. *Journal of Physical Oceanography*, **10 (1)**, 83–89, doi:10.1175/1520-0485(1980)010⟨0083:EOTLRO⟩2.0.CO;2. (Cité pages 5, 17, and 28.)

Phillips, O., 1967: Theoretical and experimental studies of gravity wave interactions. *Proceedings of the Royal Society of London. Series A. Mathematical and Physical Sciences*, **299 (1456)**, 104–119. (Cité pages 73 and 74.)

Plumb, R. A. and R. Ferrari, 2005: Transformed eulerian-mean theory. part i: Nonquasigeostrophic theory for eddies on a zonal-mean flow. *Journal of physical oceanography*, **35 (2)**, 165–174. (Cité page 107.)

Polzin, K., 2004: Idealized solutions for the energy balance of the finescale internal wave field*. *Journal of Physical Oceanography*, **34 (1)**, 231–246. (Cité pages 20, 24, and 27.)

Polzin, K., A. C. Naveira H-Garabato, T. H. Huussen, B. Sloyan, and S. Waterman, 2014: Finescale parameterizations of turbulent dissipation. *Journal of Geophysical Research: Oceans*, **119**. (Cité pages 19 and 21.)

Polzin, K., J. Toole, J. Ledwell, and R. Schmitt, 1997: Spatial variability of turbulent mixing in the abyssal ocean. *Science*, **276 (5309)**, 93–96. (Cité pages 6 and 11.)

Polzin, K. L., 2009: An abyssal recipe. *Ocean Modelling*, **30 (4)**, 298–309, doi: 10.1016/j.ocemod.2009.07.006. (Cité pages 22, 23, 24, and 25.)

Reinecke, P. A. and D. R. Durran, 2008: Estimating topographic blocking using a froude number when the static stability is nonuniform. *Journal of the Atmospheric Sciences*, **65 (3)**, 1035–1048. (Cité page 94.)

Saenko, O. and W. Merryfield, 2005: On the effect of topographically enhanced mixing on the global ocean circulation. *Journal of Physical Oceanography*, **35 (5)**, 826–834. (Cité page 27.)

Saenko, O. A., X. Zhai, W. J. Merryfield, and W. G. Lee, 2012: The combined effect of tidally and eddy-driven diapycnal mixing on the large-scale ocean circulation. *Journal of Physical Oceanography*, **42 (4)**, 526–538. (Cité page 26.)

Scott, R. B., J. A. Goff, A. C. Naveira Garabato, and A. J. G. Nurser, 2011: Global rate and spectral characteristics of internal gravity wave generation by geostrophic flow over topography. *Journal of Geophysical Research: Oceans*, **116 (C9)**, doi:10.1029/2011JC007005. (Cité page 11.)

Sheen, K., et al., 2013: Rates and mechanisms of turbulent dissipation and mixing in the southern ocean: Results from the diapycnal and isopycnal mixing experiment in the southern ocean (dimes). *Journal of Geophysical Research: Oceans*. (Cité pages 25, 42, 45, and 122.)

Simmons, H. L., S. R. Jayne, L. C. S. Laurent, and A. J. Weaver, 2004: Tidally driven mixing in a numerical model of the ocean general circulation. *Ocean Modelling*, **6 (3)**, 245–263. (Cité page 27.)

St. Laurent, L. C., H. L. Simmons, and S. R. Jayne, 2002: Estimating tidally driven mixing in the deep ocean. *Geophysical Research Letters*, **29 (23)**, doi:10.1029/2002GL015633. (Cité pages 26 and 27.)

Talley, L. D., G. L. Pickard, W. J. Emery, and J. H. Swift, 2011: *Descriptive physical oceanography: an introduction*. Academic Press. (Cité pages 3, 5, 8, and 10.)

Waterhouse, A. F., et al., 2014: Global patterns of diapycnal mixing from measurements of the turbulent dissipation rate. *Journal of Physical Oceanography*, **44**, 1854–1872. (Cité page 26.)

Waterman, S., A. C. N. Garabato, and K. L. Polzin, 2012: Internal waves and turbulence in the antarctic circumpolar current. *Journal of Physical Oceanography*, 120927134059000, doi:10.1175/JPO-D-11-0194.1. (Cité page 22.)

Waterman, S., K. L. Polzin, A. C. Naveira Garabato, K. L. Sheen, and A. Forryan, 2014: Suppression of internal wave breaking in the antarctic circumpolar current near topography. *Journal of Physical Oceanography*, **44 (5)**, 1466–1492. (Cité pages 12 and 41.)

Webb, D. and N. Suginohara, 2001: Oceanography: Vertical mixing in the ocean. *Nature*, **409 (6816)**, 37–37. (Cité page 7.)

Wright, C. J., R. B. Scott, P. Ailliot, and D. Furnival, 2014: Lee wave generation rates in the deep ocean. *Geophysical Research Letters*, **41 (7)**, 2434–2440. (Cité pages 11, 12, and 24.)

A.3 Submitted paper

An article was submitted to *Journal of Physical Oceanography* to transfer the major findings of this work to the scientific community. Here is its submitted form.

Main body
Click here to download LaTeX File (.tex, .sty, .cls, .bst, .bib): Labreuche_2014.tex
Generated using version 3.0 of the official AMS LaTeX template

Energy pathways of internal waves generated by geostrophic motions over small scale topography

Pierre Labreuche[1,2,3] *, Julien Le Sommer[2,3], Chantal Staquet[1]

[1] *Univ. Grenoble Alpes / CNRS / INPG, Laboratoire des Écoulements Géophysiques et Industriels, F-38041 Grenoble*

[2] *CNRS, Laboratoire de Glaciologie et Géophysique de l'Environnement, F-38041 Grenoble*

[3] *Univ. Grenoble Alpes, Laboratoire de Glaciologie et Géophysique de l'Environnement, F-38041 Grenoble*

* *Corresponding author address:* Pierre Labreuche, LEGI, Domaine Universitaire, BP 53, 38041 Grenoble Cedex 9, France.

E-mail: pierre.labreuche@legi.grenoble-inp.fr

ABSTRACT

Recent studies suggest that internal lee waves generated by flows impinging on rough topography enhance turbulent kinetic energy dissipation in the abyssal ocean. Nikurashin and Ferrari (2010b) proposed from two-dimensional numerical simulations that the bottom intensification of turbulent kinetic energy dissipation may result from the dissipative interaction between internal lee waves and inertial oscillations. Here, we investigate energy pathways of internal lee waves in a similar setting in order to provide information for representing the impact of internal lee waves in ocean models. To this purpose, we perform a series of two-dimensional non-hydrostatic numerical simulations of a geostrophic flow over an idealized topography. We find that 10 to 30% of the radiated internal lee wave energy is dissipated in the water column, and that the dissipation is confined in a bottom layer of variable thickness, of at most 1000 m. Over the range of parameters studied, the vertically integrated turbulent kinetic energy dissipation rate typically reaches ~ 20 mW m^{-2}. We further show that the emergence of inertial oscillations results from nonlinear resonant interactions involving internal lee waves and therefore does not require dissipative processes. A prediction of the growth rate of the inertial oscillations is obtained from the theory of resonant interactions, with values of a few inertial periods, which compares well with the numerically computed values. Our results suggest that existing finescale parameterizations may miss a key feature of the fate of internal lee waves by not taking inertial oscillations into account.

1. Introduction

The Southern Ocean plays a key role in shaping global ocean circulation and stratification. Diapycnal mixing and wind driven upwelling bring deep waters to the surface where they are further transformed by mixed layer processes and air-sea exchanges (Sloyan and Rintoul 2001). In the ocean, a large fraction of the diapycnal mixing required to sustain the large scale overturning circulation is believed to be associated with internal wave breaking (Ferrari and Wunsch 2009). The internal wave field generally results from the radiation of baroclinic motions by winds and by barotropic tides but it has been suggested that the interaction of deep reaching geostrophic flows with rough topography could also provide an effective mechanism for generating internal waves (Polzin and Firing 1997). The generation mechanism is by essence similar to the emission of mountain waves in the troposphere, referred to as internal lee waves. To a good approximation, this emission process is well described by the linear theory of Bell (1975). Recent estimates of the energy flux radiated by internal lee waves in the ocean indicate that about 50% of the bottom conversion of internal lee waves occurs in the Southern Ocean (Nikurashin and Ferrari 2011) because of the strong deep flows associated with the Antarctic Circumpolar Current and of rough bathymetry. The numerical simulations performed by Nikurashin et al. (2012) suggest that a large fraction of the wave energy could be dissipated in the abyss and therefore contribute to diapycnal mixing.

For ocean climate models to reproduce ocean circulation adequately, a close attention should be paid to the parameterization of the divergence of buoyancy fluxes due to turbulent diapycnal mixing. In practice, turbulent diapycnal mixing in ocean models involves

a diapycnal diffusivity coefficient K_ρ that varies in time and space. The overturning circulation simulated by ocean climate models is largely dependent on the prescribed spatial distribution of K_ρ (Bryan 1987). As an example, diapycnal diffusivity in the deep Southern Ocean controls the lower-limb of the Southern Ocean overturning circulation (Ito and Marshall 2008). Arguably, predicting the fate of ocean circulation under changing climate conditions requires that the distribution of K_ρ depends prognostically on the simulated circulation. Current practice for parameterizing turbulent diapycnal mixing due to internal waves is to compute K_ρ from the *turbulent kinetic energy* (TKE) dissipation rate per unit mass ε following Osborn (1980). This is expressed as

$$K_\rho = \gamma \frac{\varepsilon}{N^2} \tag{1}$$

where N refers to the local buoyancy frequency and γ refers to the mixing efficiency, generally assumed to be constant.

The distribution of TKE dissipation rate associated with internal waves is generally computed with a formula equivalent to the empirical parameterization proposed by St. Laurent et al. (2002) for internal waves emitted by tidal motions, namely

$$\varepsilon = \frac{q\, E(x,y) F(z)}{\rho} \tag{2}$$

where $E(x,y)$ is the energy flux radiated from the bottom topography, q is the fraction of this energy flux that is assumed to be dissipated in the water column and $F(z)$ describes the vertical structure of TKE dissipation. Eq. (2) can equally be applied to internal waves emitted by subinertial flows, provided $E(x,y)$ is appropriately estimated (Melet et al. 2013; Saenko et al. 2012).

Whilst estimates of $E(x, y)$ can be obtained on the basis of the linear theory of internal lee wave (Scott et al. 2011; Nikurashin and Ferrari 2011), large uncertainties remain in the specification of q and $F(z)$ in ocean models. Reducing these uncertainties is an important issue for ocean climate models as their response is generally very dependent on $F(z)$ (Melet et al. 2013, 2014). For internal tides, a promising approach has recently been proposed by Polzin (2009) on the basis of the Radiation Balance Equation. In this framework, q and $F(z)$ can be predicted assuming that the turbulent cascade of kinetic energy toward small scale is driven by nonlinear interactions among internal waves with no effect of rotation.

The question of the fate of the internal wave energy radiated by geostrophic flows impinging on bottom topography in the Southern Ocean is largely open. As mentioned above, a key question is to know what fraction of this energy is eventually dissipated and where this dissipation occurs in the Southern Ocean. The approach proposed by Polzin (2009) for internal tides does not seem to be directly applicable to internal lee waves. Indeed, in its present form, this theory neglects rotation effects on wave-wave interactions and therefore cannot account for interactions involving inertial oscillations or quasi-inertial waves. However, in a series of recent papers, Nikurashin and Ferrari (2010a,b) showed from numerical simulations that internal lee waves can interact strongly with bottom intensified inertial oscillations. These inertial oscillations result from momentum flux from the lee waves and, once of finite amplitude, provide in turn favorable conditions for internal lee wave breaking, leading to an intensification of TKE dissipation. The underlying mechanisms involved in such interactions still have to be addressed.

The present study focuses on how inertial oscillations affect the energy pathways during the evolution of internal lee waves: we propose a mechanism leading to the growth of these

oscillations and, once these motions have reached a finite amplitude, we analyse the possible link between the vertical structure of the inertial oscillations and the TKE dissipation rate. We combine theory and numerical simulations in a vertical plane for this purpose, for the configuration proposed by Nikurashin and Ferrari (2010b). Practically, we aim at providing guidance for specifying appropriate q and $F(z)$ for internal lee waves in the deep Southern Ocean.

The outline of the paper is as follows. Section 2 describes the physical set-up and numerical parameters and discusses the overall behavior of the flow. Section 3 provides evidence that inertial oscillations are generated through resonant triad interactions involving the lee wave field. The growth rate of the inertial oscillations is predicted in section 4 using a resonant interaction theory and compared to the values computed from the numerical simulations. Section 5 investigates systematically the relation between inertial oscillations and TKE dissipation over a range of physical parameters typical of Southern Ocean conditions. The implications and limitations of our results are discussed in section 6.

2. Physical configuration and numerical set-up

a. Physical configuration

We consider the simple flow configuration of Nikurashin and Ferrari (2010b) sketched in Fig. 1. It consists of a uniform flow of amplitude $U_G = 0.1$ m s^{-1} flowing over a sinusoidal topography of form $h(x) = h_T \cos(2\pi x/l_T)$, where h_T takes the values 20 m, 40 m and 80 m and l_T is equal to either 1200 m or 2000 m.

The wavelength l_T is also the horizontal extent of the numerical domain, denoted L. The configuration is two-dimensional, in the $x - z$ plane. The buoyancy frequency N is uniform with value 10^{-3} s^{-1}. The Coriolis frequency f is equal to 10^{-4} s^{-1}, except in two runs discussed in sections 4 and 5 in which f is doubled.

b. Numerical set-up

In order to study the interaction between Internal Lee Waves (ILWs) and Inertial Oscillations (IOs), we use Symphonie NH, a non hydrostatic regional ocean model which solves the non-hydrostatic Boussinesq equations (Auclair et al. 2011). Periodic boundary conditions are used along the x-direction. The bottom boundary conditions are set either to free slip or to partial slip with a bottom roughness of 1 mm. The flow is initiated from a state of rest. The horizontal velocity component is then forced through a body force fU_G in the meridional momentum equation. During the first 24 h, the flow field is relaxed towards the desired value of U_G with a time-scale of 3 h, to avoid spurious oscillations during model spin-up (Nikurashin and Ferrari 2010b). After 24 h, the integration is carried out for 15 days, so as to reach a statistically steady state.

The numerical grid has a fixed spacing in the horizontal ($\Delta x = 12.5$ m) and uses a topography-following (σ-) coordinate along the vertical direction. To avoid wave reflection from the upper boundary, we apply a damping layer of thickness 5000 m starting at 2000 m above the bottom. Hence the height of the physical domain, denoted H, is 2000 m. In the damping layer, grid spacing is stretched from about 5 m to about 300 m in equivalent Δz, and the viscosity and diffusivity are increased in proportion with the vertical grid spacing.

The viscosity and diffusivity are respectively set to 10^{-2} and 10^{-3} m^2 s^{-1} below the damping layer. The numerical and physical parameters of the numerical simulations are summarized in Table 1.

c. *Overall flow behavior*

Basic features of the flow behavior are illustrated in Fig. 2, at two successive times. After one inertial period (Fig. 2 top panel), quasi-linear internal lee waves have been radiated and propagate upwards. Over the range of parameters studied, the topography is subcritical, namely the slope of wave propagation exceeds the slope of the topography. After seven inertial periods (Fig. 2 bottom panel), wave breaking occurs at the bottom of the domain, below 1000 m. As we shall see in section 3, IOs amplify through nonlinear wave-wave interactions.

In the following, we decompose the flow into three components, namely the geostrophic flow, the IOs and the ILWs. The geostrophic flow is set to the constant value of $U_G = 0.1$ m s^{-1}, along the x-direction. In the horizontally periodic case we are considering in this paper, IOs are internal waves of frequency f; their horizontal scale is therefore infinite, but their vertical scale is finite and arbitrary. Hence the IO velocity field may be considered as depending upon height and time only. This motion is defined as: $\boldsymbol{U}_{IO}(t,z) = \overline{\boldsymbol{u}(x,z,t) - U_G}^{x}$, where $\overline{(.)}^{x}$ denotes a horizontal average. Finally, the internal waves are defined as $\boldsymbol{U}_{ILW}(x,z,t) = \boldsymbol{u}(x,z,t) - \boldsymbol{U}_G - \boldsymbol{U}_{IO}(t,z)$, hence the internal lee wave field has a zero horizontal average by definition, which is consistent with the periodic boundary conditions.

Figure 3 displays the vertical profile of the IO amplitude (Fig. 3 top panel) and of the

TKE dissipation rate (Fig. 3 bottom panel) at the end of the simulations for the L_{2}_fs cases. Both quantities are clearly enhanced near the topography for $h_t \geq 40$ m. Using Eq. (1), $N = 10^{-3}$ s^{-1} and assuming $\gamma = 0.2$, the TKE dissipation rate averaged over the lower 500 m in simulation $H_{80}L_{2}\_fs$ yields a vertical diffusivity of about $\sim 4.10^{-3}$ m^2 s^{-1}. This value is consistent with the findings of Nikurashin et al. (2012) and is only slightly above the range of TKE dissipation rate in the deep Southern Ocean inferred from vertical microstructure profilers (Waterman et al. 2014; Garabato et al. 2004). Such a level of diapycnal mixing could have a notable impact on the lower limb of the Southern Ocean overturning (Ito and Marshall 2008).

Figure 3 also suggests possible correlation between the IO and TKE dissipation rate profiles. This led Nikurashin and Ferrari (2010b) to propose that TKE dissipation takes place at locations of strong IO amplitude. The next two sections aim at identifying the mechanisms at the origin of the IO growth and to quantify the growth rate.

3. A mechanism of resonant triad interaction

In the previous section, we have seen that inertial oscillations emerge during the evolution of the flow. In this section, we provide evidence that the growth of inertial oscillations results from resonant triad interactions among internal waves. This can be rationalized within the frame of the resonant interaction theory (RIT) (Phillips 1967). It can be shown from this theory that significant energy exchanges among a wave triad can only occur if the wavevectors and frequencies satisfy specific relations. Under such conditions, the wave triad is said to be resonant. In what follows, we predict all possible resonant triads that involve the inertial

oscillations and the internal lee waves.

Since intrinsic wave frequencies are involved in the RIT, the theory is applied here in a frame of reference attached to the geostrophic current U_G. We recall that lee waves are steady in the frame of reference attached to the topography, namely their absolute frequency vanishes. In the following, the word *frequency* refers to the intrinsic frequency.

a. Resonant interactions involving inertial oscillations and internal lee waves

Three internal waves are involved in a resonant triad if the algebraic sum of their frequencies and the sum of their wave vectors amounts to zero. Assuming two of these waves are the ILW and the IO and denoting the third wave with a $*$ subscript, these conditions are expressed as:

$$\sigma_{ILW}\boldsymbol{k}_{ILW} + \sigma_*\boldsymbol{k}_* + \sigma_{IO}\boldsymbol{k}_{IO} = 0 \tag{3a}$$

$$\sigma_{ILW}\omega_{ILW} + \sigma_*\omega_* + \sigma_{IO}\omega_{IO} = 0 \tag{3b}$$

where the subscripts refer to the different waves, $\sigma = \pm 1$, $\boldsymbol{k} = (k, m)$ is the wave vector (in the present two-dimensional case) and ω the intrinsic frequency. We assume that ω is positive implying that the σ coefficients cannot be of the same sign. Along with the three dispersion relations, one gets 6 equations for 9 variables. Depending on the choice of $(\sigma_{ILW}, \sigma_*, \sigma_{IO})$, several triads, involving different waves, can arise. We assume that the wave of largest amplitude is the internal lee wave. Since this wave has the same spectral properties throughout the different triads, the triads can be considered as independent (Chow et al. 1996).

Let us first consider that $-\sigma_{ILW} = \sigma_{IO} = \sigma_* = 1$. The problem is closed by expressing

189 that the ILW parameters verify:

$$k_{ILW} = k_T \tag{4a}$$

$$\omega_{ILW} = U_G k_T \tag{4b}$$

190 and by writing that the IOs are homogeneous in the horizontal plane:

$$k_{IO} = 0. \tag{5}$$

191 Since we also know that $\omega_{IO} = f$, the problem boils down to 5 equations and 5 unknown

192 variables (m_{ILW}, m_{IO}, k_*, m_*, ω_*):

$$-k_{ILW} + k_* + k_{IO} = 0 \tag{6a}$$

$$-m_{ILW} + m_* + m_{IO} = 0 \tag{6b}$$

$$-\omega_{ILW} + \omega_* + \omega_{IO} = 0 \tag{6c}$$

$$\omega_*^2 = \frac{N^2 k_*^2 + f^2 m_*^2}{k_*^2 + m_*^2} \tag{6d}$$

$$\omega_{ILW}^2 = \frac{N^2 k_{ILW}^2 + f^2 m_{ILW}^2}{k_{ILW}^2 + m_{ILW}^2}. \tag{6e}$$

193 Solving these equations leads to the following solution. For the ILW field, we get:

$$k_{ILW} = k_T \tag{7a}$$

$$\omega_{ILW} = U_G k_T \tag{7b}$$

$$m_{ILW} = -k_T \sqrt{\frac{N^2 - (U_G k_T)^2}{(U_G k_T)^2 - f^2}} \tag{7c}$$

194 where we chose $m_{ILW} < 0$ to ensure that the ILWs radiate energy away from topography.

For the third wave of the triad, we get:

$$k_* = k_T \tag{8a}$$

$$\omega_* = U_G k_T - |f| \tag{8b}$$

$$m_* = \pm k_T \sqrt{\frac{N^2 - (U_G k_T - |f|)^2}{(U_G k_T - |f|)^2 - f^2}}. \tag{8c}$$

It is important to recall that this internal wave can only exist provided $|f| < U_G k_T - |f| < N$. We notice from Eq. (8c) that the sign of m_* is not determined implying that the $*$ wave can radiate in both vertical directions. The vertical wavenumber of the IOs is inferred from the relation $m_{IO} = m_{ILW} - m_*$, implying that the spectral parameters of the IOs are:

$$k_{IO} = 0 \tag{9a}$$

$$\omega_{IO} = |f| \tag{9b}$$

$$m_{IO} = -k_T \Big(\sqrt{\frac{N^2 - (U_G k_T)^2}{(U_G k_T)^2 - f^2}} \pm \sqrt{\frac{N^2 - (U_G k_T - |f|)^2}{(U_G k_T - |f|)^2 - f^2}} \Big). \tag{9c}$$

The case $\sigma_{ILW} = \sigma_* = -\sigma_{IO} = 1$ is equivalent to the case described above.

201 Finally, the case $\sigma_{ILW} = -\sigma_* = \sigma_{IO} = 1$ yields:

$$k_{ILW} = k_T \tag{10a}$$

$$\omega_{ILW} = U_G k_T \tag{10b}$$

$$m_{ILW} = -\sqrt{\frac{N^2 - (U_G k_T)^2}{(U_G k_T)^2 - f^2}}\, k_T \tag{10c}$$

$$k_* = k_T \tag{10d}$$

$$\omega_* = U_G k_T + |f| \tag{10e}$$

$$m_* = \pm\sqrt{\frac{N^2 - (U_G k_T + |f|)^2}{(U_G k_T + |f|)^2 - f^2}}\, k_T \tag{10f}$$

$$k_{IO} = 0 \tag{10g}$$

$$\omega_{IO} = |f| \tag{10h}$$

$$m_{IO} = -k_T\Big(\sqrt{\frac{N^2 - (U_G k_T)^2}{(U_G k_T)^2 - f^2}} \pm \sqrt{\frac{N^2 - (U_G k_T + |f|)^2}{(U_G k_T + |f|)^2 - f^2}}\Big). \tag{10i}$$

202 In short, two possibilities arise for the frequency of the third wave ($\omega_* = U_G k_T \pm |f|$),
203 and for each case two possibilities arise for the sign of the vertical wavenumber of the third
204 wave (m_*), and hence for the value of m_{IO}. Therefore, four possibilities arise for the vertical
205 wavenumber of the IO.

206 These triads can in turn be involved in higher order interactions. For instance, the
207 interaction between an IO and a $*$ wave of frequency $U_G k_T - |f|$ may give rise to a new wave
208 of frequency $U_G k_T - 2|f|$. More generally, energy transfers occur along a discrete spectrum
209 of frequencies $U_G k_T + nf$, where n is an integer (positive or negative) which must satisfy

$$1 - \frac{U_G k_T}{|f|} < n < \frac{N}{|f|} - \frac{U_G k_T}{|f|}. \tag{11}$$

210 expressing that these frequencies lie in the range of internal wave frequencies.

b. Evidence of resonant triads from spectral analysis

Figure 4 is a frequency spectrum of the vertical velocity w for simulation $H_{20}L_2$. This spectrum is computed in a frame of reference moving at speed U_G since intrinsic frequencies are to be detected. The straight line is the confidence level at 99%, implying that the spectrum significantly departs from red noise when it exceeds this line.

Several peaks clearly emerge from the power spectrum, which are comprised between $|f|$ and N. Two of them are associated with the ILW frequency ($\omega = U_G k_T$) and with the IOs ($\omega = |f|$). One would expect the sum and difference of these two peaks ($\omega = U_G k_T \pm |f|$) to be dominant as well but only the difference of these frequencies appears, for a reason explained in the next section. A peak at frequency $U_G k_T + 2|f|$ also emerges. No general conclusion about the presence of this peak can be drawn however since, depending upon the computation we analyzed, peaks at frequency $U_G k_T + 3|f|$ or $U_G k_T + 4|f|$ may instead (or also) be visible. But this clearly attests of the presence of higher order triads. Note that the frequency $U_G k_T - 2|f|$ is not present, very likely because its value for this computation is very close to the lower bound of the ILW frequency, equal to $|f|$.

4. Growth rate of inertial oscillations

a. Expression of the growth rate of inertial oscillations

Evolution equations can be inferred from the RIT for the amplitude of the waves involved in a resonant triad (see Koudella and Staquet 2006 for instance). This evolution occurs on a slow time scale, $t_1 = s\,t$ say, where $s \ll 1$ is a normalized amplitude of the waves at the

initial time (such as the initial wave steepness). When one wave in the triad is of much larger amplitude than the other two (all waves being of very small amplitude, a basic assumption of the RIT), this large amplitude wave can be assumed to be steady over the time scale t_1. This permits the linearization of the evolution equations, from which the solution for the two smaller amplitude waves can be inferred. The latter waves either exchange energy within the triad over a periodic cycle, implying that their amplitude remains bounded, or their amplitude can grow exponentially, the largest amplitude wave feeding them. We consider the resonant triad made of the ILW, assumed to have the largest amplitude, the IOs and the * wave introduced in the previous section. In an inviscid fluid, the oscillatory or exponential behavior depends upon the sign of the parameter Γ^2 defined by:

$$\Gamma^2 = \left(\frac{A_{ILW}}{2}\right)^2 S_* S_{IO} \tag{12}$$

where A_{ILW} is the amplitude of the internal lee wave, and S_* and S_{IO} are interaction coefficients of the $*$ and IO waves, respectively, with the ILW. The expression of these coefficients is:

$$S_* = \frac{\sigma_{ILW}\sigma_{IO}}{2K_*^2\omega_*}\Big[\omega_*(K_{ILW}^2 - K_{IO}^2) + N^2 k_*(\frac{k_{ILW]}}{\omega_{ILW}} - \frac{k_{IO}}{\omega_{IO}}) + f^2 m_*(\frac{m_{ILW}}{\omega_{ILW}} - \frac{m_{IO}}{\omega_{IO}})\Big]$$
$$(m_{IO}k_{ILW} - m_{ILW}k_{IO}) \tag{13a}$$

$$S_{IO} = \frac{\sigma_{ILW}\sigma_*}{2K_{IO}^2\omega_{IO}}\Big[\omega_{IO}(K_{ILW}^2 - K_*^2) + N^2 k_{IO}(\frac{k_{ILW}}{\omega_{ILW}} - \frac{k_*}{\omega_*}) + f^2 m_{IO}(\frac{m_{ILW}}{\omega_{ILW}} - \frac{m_*}{\omega_*})\Big]$$
$$(m_* k_{ILW} - m_{ILW}k_*) \tag{13b}$$

with $K_i = |\mathbf{k_i}|$. When $\Gamma^2 > 0$, namely $S_* S_{IO} > 0$, the IO and the * waves grow exponentially at rate Γ, implying that the ILW is unstable in the inviscid limit. When $\Gamma^2 < 0$ ($S_* S_{IO} < 0$), the ILW is stable.

b. Validation with numerical simulations

For the range of parameters we use, $\Gamma^2 > 0$ only for the two triads involving the $*$ wave of frequency $U_G k_T - |f|$ (these triads differ by the value of m_{IO}). This is valid for all simulations except for those with $f = 2.10^{-4}$ s^{-1}, since $U_G k_T - |f| < |f|$ in this case.

The finding of these triads is consistent with Hasselman's criterion (Hasselmann 1967), which states that a primary wave is unstable if it has the highest frequency in the triad. Hence, the internal lee wave, of frequency $U_G k_T$, is unstable for a triad involving the IO and the $*$ wave at $U_G k_T - |f|$, but stable for a triad involving the IO and the $*$ wave at $U_G k_T + |f|$. (Hasselman's criterion can actually be shown to be equivalent to $S_* S_{IO} > 0$.) In the former triad energy is continuously transferred from the ILW to the IO and the $*$ wave, whereas in the latter triad periodic energy exchange takes place between the three waves. This entails that although both types of triads are expected to have a signature in the frequency spectrum displayed in Fig. 4, only the triad involving the $*$ wave with frequency $U_G k_T - |f|$ is dominant.

For initial times, one can compare the predicted growth rate Γ with the growth rate of the IOs in the simulations. Note that theoretical values for the inviscid growth rate, defined by Eq. (12), will be used. The damping effect due to dissipative processes adds indeed a term of the form $\nu\,(1+1/Pr)\,k_T^2\,(N/(U_G k_T - |f|))^2$ in the expression of Γ (see Koudella and Staquet (2006)), which can quite be neglected in the present case. Figure 5 displays the temporal evolution of the IOs at 100 m above the topography, in log-lin coordinates for the simulations of Table 1 at frequency f. The spin-up of the simulations, during the first 24 hours, is kept on the figure for clarity. Since the RIT predicts an exponential growth of the

IOs, a log-lin representation of their temporal evolution should exhibit a straight line at early times. The theoretical prediction for each case is shown, permitting comparison between the simulations and the RIT. Since the theory predicts growth rates of similar values when the sign of m_* is changed, only the values associated with negative m_* are shown for clarity.

Figure 5 shows that the IO amplitude does display an initial growth, before a quasi-steady state is reached when the topography amplitude is equal to 40 m or 80 m. This quasi-steady state will be further discussed in section 5. For $h_T = 20$ m, the IOs keep growing over the whole duration of the simulation. For $h_T \geq 40$ m, some simulations exhibit a slope change during the IO growth, which might be due to the presence of several triads at work before being dominated by the triads we identified. The theoretical growth rate is therefore indicated with a straight line for each case during the final growth regime, before the quasi-state is reached. Note that the position of these straight lines for the $h_T = 20$ m simulations is somewhat arbitrary since the quasi-steady state has not been reached yet. Overall, the theoretical values of the growth rates appear to agree well with the numerical values.

c. Vertical propagation of inertial oscillations

From the discussion at the beginning of the previous section, we only consider the two triads involving the ILW, the IO and the $*$ wave with frequency $U_G k_T - |f|$. These triads differ by the expression of the IO vertical wavenumber:

$$m_{IO} = -k_T\Big(\sqrt{\frac{N^2 - (U_G k_T)^2}{(U_G k_T)^2 - f^2}} \pm \sqrt{\frac{N^2 - (U_G k_T - |f|)^2}{(U_G k_T - |f|)^2 - f^2}}\Big), \tag{14}$$

from where the expression of the vertical phase speed of the IO can be computed ($c_\phi^z|_{IO} = f/m_{IO}$). For our range of parameters, $m_* m_{IO}$ is negative, meaning that a $*$ wave that propagates energy upwards ($m_* < 0$) is associated with an IO that propagates phase upwards ($m_{IO} > 0$), and conversely.

Figure 6 displays a time-height diagram of the horizontal velocity of the IO component for simulation $H_{20}L_2$. The IOs propagate upwards, the vertical phase speed of the upward propagating IO predicted by RIT is indicated with a black line for comparison. A very good agreement is observed below 1000 m or so, where the IO amplitude is the largest. As discussed above, downward propagating IOs ($m_{IO} < 0$) are also predicted by the theory, which do not appear in the numerical solution. One possible explanation is that the latter wave is of smaller scale than the upward propagating wave and therefore more prone to dissipation ($2\pi/|m_1|$ is equal to 240 m for the downward wave and to 1015 m for the upward wave). Indeed, the viscous time scale associated with the downward wave is close to 2 inertial periods, against 40 inertial periods for the upward wave, which may account for its absence (or insignificance).

d. On the role of dissipation in the growth of inertial oscillations

Nikurashin and Ferrari (2010b) also predicted that inertial oscillations should grow due to nonlinear interactions with internal lee waves. Yet dissipation is essential in their asymptotic theory, whereas the resonant interaction framework does not require any dissipation.

The work of Nikurashin and Ferrari (2010b) relies on the theoretical assumption that the geostrophic and IO velocity fields are present at zero order in an expansion of the total

velocity field in terms of the steepness of the ILW, assumed to be small. This means that the IO amplitude is large compared to that of the wave field (but may be small compared to the parameter f/k_T). Consistently, the IOs contribute to the ILW generation at the topography, along with the geostrophic flow. These assumptions are quite valid at later times in the flow development, when dissipative effects have had time to influence the ILW dynamics. Damping is indeed required to have a non vanishing momentum flux divergence of the ILWs, which forces the IOs.

By contrast, in the resonant interaction framework considered in the present paper, the amplitude of the internal lee waves is assumed to be much larger than that of the other waves involved in the triads, which include the IOs. Consequently, the IOs do not have any impact on the emission of ILWs at topography. Also, inherent to the resonant interaction theory, dissipative effects do not play any role in the IO growth.

It follows that the two approaches do not contradict each other but apply at different times. The resonant interaction theory accounts for the growth of inertial oscillations from background noise with no role of dissipative effects, while the theory by Nikurashin and Ferrari (2010b) describe later times when the IO amplitude has become of leading order relative to the ILW amplitude, with the latter amplitude being damped by dissipative effects.

5. Relationship between inertial oscillations and turbulent kinetic energy dissipation

As found by Nikurashin and Ferrari (2010b) and shown in Fig. 5, the IO growth for $h_T \geq 40$ m is followed by a state where the IO amplitude is quasi-steady. This state will be referred to as saturated. The purpose of this section is to investigate whether some link can be found between the IOs and the TKE dissipation rate during the saturated state: is the IO amplitude large when and where TKE dissipation is large as well ? Of course, the adjective *large* has to be specified. Our ultimate objective is to know whether knowledge on the TKE dissipation rate can be inferred from that on the IO field if measurements of the latter field could be made in the deep ocean.

a. Temporal evolution of the inertial oscillations and of the TKE dissipation rate in the numerical simulations

Figure 7 displays for comparison the temporal evolution of the IO field at 100 m above topography (top) and of the TKE dissipation rate integrated over 2000 m (bottom) for all $f-$simulations. Simulations where f is doubled are not present since the IOs hardly grow in these simulations.

The top frame displays the same data as in Fig. 5, in which the IO growth regime was analysed. We now focus on the saturated state. The IO amplitude during this state is all the larger the higher the topography. The boundary condition at the topography (free-slip or partial-slip) does not appear to have any influence on the value of the saturated IO amplitude.

By contrast, the wavelength of the topography has a major impact on this value, a smaller wavelength, associated with higher frequency waves, promoting higher amplitude IOs. As a result, the saturated value of the IO amplitude appears to be sensitive to the parameters in the simulations, reaching values ranging from 0.08 m s^{-1} to 0.18 m s^{-1}, namely from half to twice the value of the geostrophic current.

As for the TKE dissipation rate (bottom frame), it increases slowly with time when $h_T = 20$ m and, like the IO amplitude, does not reach saturation within the time of the simulations. By contrast, for $h_T \geq 40$ m, a quasi-steady state is reached after a few inertial periods, the TKE dissipation rate slightly decreasing with time during this regime. Like the IO saturated amplitude, the TKE dissipation rate does not depend upon the boundary condition at the topography and is all the stronger the higher the topography, as expected. As opposed to the IOs however, the saturated value of the TKE dissipation rate does not depend upon the wavelength of the topography.

b. Amplitude of the inertial oscillations and of the TKE dissipation rate

The purpose of this section is to evaluate whether some correlation can be detected between the IO amplitude and the TKE dissipation rate during the saturated state. To make these quantities comparable, we scale the TKE dissipation rate with the bottom energy conversion rate (averaged over one ILW period) P_{up}. As for the IO field, we convert this field into energy per unit mass, $E = \frac{1}{2}U_I^2$, which we scale with the energy radiated by the ILW during one period $P_{up}/(2\pi/|f|)$.

Figure 8 shows a scatter plot of these two non dimensional quantities integrated over

the physical domain and averaged from 12 to 15 inertial periods. Simulations leading to the prediction of a growth rate corresponding to a time smaller than 3 inertial periods are indicated with a filled marker (grey or black). For simulations with empty markers, this time is larger than 10 inertial periods. Simulations with $\Gamma^2 < 0$ are displayed with + and $\times$ signs.

As expected from the top frame of Figure 7, the amount of ILW energy transferred to the IO field is weak over one inertial period for $h_T = 20$ m, less than 20 %. For h_T larger than 40 m by contrast, 30 to 70% of the energy radiated by the ILW over an inertial period is converted to IO energy. As for the volume-averaged TKE dissipation rate, when $h_T \geq 40$ m, its value during the saturated state is comprised between 10 to 30% of the bottom energy conversion. It is noteworthy that similar ratios of dissipated to emitted energy have been observed in the ocean (Sheen et al. 2013; Brearley et al. 2013).

We finally note that, for a given wavelength of the topography, the IO amplitude grows with the TKE dissipation rate, suggesting some relation between these two quantities.

c. Vertical structure of the inertial oscillations and of the TKE dissipation rate

Figures 9 top and bottom panels display the vertical profiles of the IO amplitude and of TKE dissipation rate, respectively. These profiles show that the fields are clearly enhanced near topography, systematically under 1000 m. To estimate more precisely whether the height below which the IOs are enhanced is correlated with the height below which the TKE dissipation rate is enhanced for a given simulation, we carry out the following quantitative analysis. We compare each IO and TKE dissipation rate profile, averaged from 12

388 to 15 inertial periods, with an analytical profile $g(z_c, z_w, g_0, z)$ designed so as to optimize its
389 correlation with the numerical profile. The analytical profile consists of a piecewise linear
390 function:

$$g(z) = \begin{cases} g_0 & \text{if } z = 0 \\ 1 & \text{if } z = z_c - z_w \\ 0 & \text{if } z \geq z_c \end{cases}$$

391 where z_c is the *effective height* above topography under which the field is confined, z_w and
392 g_0 are adjustment parameters.

393 As an example, Fig. 10 shows both the IO and TKE dissipation rate profiles averaged
394 from 12 to 15 inertial periods for simulation $H_{40}L_2$, and the corresponding analytical profiles.
395 From this comparison one gets the parameters z_c, z_w and g_0 for the IO field and the TKE
396 dissipation rate for each simulation. Our goal is to compare the effective heights z_c obtained
397 for the IOs and for the TKE dissipation rate, for each simulation.

398 Figure 11 is a scatter plot of the effective height of the IOs versus that of the TKE
399 dissipation rate for all the simulations. The same symbols as in Fig. 8 are used. Little
400 can be said for the empty markers and for + and x markers, that have such low amplitudes
401 in one or both fields that the uncertainty of the effective height can be over 500 m. By
402 contrast, the filled markers are well defined, and show that whereas the IO field effective
403 height seems to be rather independent of the parameter range (as z_c is around 1000 m for
404 all simulations), no clear conclusion can be inferred for the TKE dissipation rate effective
405 height. It does appear, however, that the TKE dissipation systematically occurs within the
406 depth with strong inertial oscillations.

In conclusion, we have shown that, after several inertial periods, the IOs and TKE dissipation rate reach a quasi-steady state. Once this quasi-steady state is reached, the saturated IO amplitude shows a significant dependence on the parameter set and about 10 to 30% of the internal lee wave energy is dissipated in the water column. Our sensitivity study shows that simulations with strong IOs are systematically associated with strong TKE dissipation. However, the vertical profile of TKE dissipation appears not to be systematically correlated with the vertical profile of inertial oscillations.

6. Conclusion and discussion

This paper investigates the mechanisms involved in the energy pathways of internal lee waves generated by geostrophic flows over small scale topography in the setting first proposed by Nikurashin and Ferrari (2010b) with a combination of numerical simulation and analytical theory. We have confirmed that, in this two-dimensional setting, the evolution of internal lee waves involves significant energy exchanges with bottom intensified inertial oscillations. We have shown that these energy exchanges are due to nonlinear resonant interactions driven by the lee wave field. The parameter regime for which such interactions can occur is specified in section 3. We used the resonant interaction theory to describe the growth rate of the inertial oscillations produced through this interaction. The theoretical prediction of the growth rate compares well with the numerically computed values. Furthermore, the numerical simulations show that after this initial growth, a saturated (or equilibrium) state can be reached. Once saturation is reached, most of the TKE dissipation is confined to a bottom layer. Over the range of parameter studied, the thickness of this layer is at

most 1000 m, but no straightforward relation to external parameters has been found. Our results also indicate that once saturation is reached, about 10 to 30% of the internal lee wave kinetic energy is dissipated locally in the water column for our range of parameters. These results provide information for estimating the fraction of local TKE dissipation q and the vertical structure function $F(z)$ of diapycnal mixing due to internal lee waves in model parameterizations based on Eq. (2) (St. Laurent et al. 2002).

There is a significant body of literature aiming at predicting TKE dissipation from the physical properties of flows at large scales. In particular, *finescale parameterizations* aim to infer TKE dissipation at microscale (< 1m) from measurements at finescale ($\sim 10 - 100$ m) on the basis of spectral properties of wave-wave interactions. But existing finescale parameterizations (as described by Polzin et al. 2013) do not account for the interaction of internal lee waves with inertial oscillations. Indeed, in such parameterizations it is usually assumed that the turbulent cascade is driven by wave-wave interactions not subject to rotation. As we have seen here in a rotating frame, the non-linear interaction of internal lee waves with inertial oscillations is critical to setting the energy spectrum. Our work suggests that finescale parameterizations should describe wave-wave interactions without assuming zero rotation. We conclude that existing finescale parameterizations might not capture the physics governing TKE dissipation in the particular setting discussed in this paper. This limitation should be counted among the possible explanations for the mismatch between estimates of TKE dissipation based on finescale parameterizations and direct measurements at microscale observed during SOFINE field campaign and discussed in Waterman et al. (2014).

It should be clearly stated that there are so far no evidence from observations that

the emission of inertial oscillations we discuss in this paper is actually taking place in the Southern Ocean. To our knowledge, there is as yet no discussion of the presence of inertial oscillations in the abyssal Southern Ocean in the literature. Direct measurements of the amplitude of inertial oscillations in the deep Southern Ocean could help at evaluating the relevance of the mechanism discussed herein.

Acknowledgments.

The authors thank Matthieu Leclair and Francis Auclair for technical assistance with the model configuration. We also thank Stephanie Waterman and Alberto Naveira-Garabato for several discussions about SOFINE and DIMES field campaigns. We are grateful to Jacques Vanneste for fruitful discussions. Symbolic calculations were performed with Sage-Math (Stein et al. 2012). For this study, the authors received funding from the Laboratoire d'Excellence OSUG@2020 and from CNRS through LEFE-INSU program.

REFERENCES

Auclair, F., C. Estournel, J. W. Floor, M. Herrmann, C. Nguyen, and P. Marsaleix, 2011: A non-hydrostatic algorithm for free-surface ocean modelling. *Ocean Modelling*, **36 (12)**, 49–70, doi:10.1016/j.ocemod.2010.09.006.

Bell, T., 1975: Lee waves in stratified flows with simple harmonic time dependence. *J. Fluid Mech*, **67 (4)**, 705–722.

Brearley, J. A., K. L. Sheen, A. C. Naveira Garabato, D. A. Smeed, and S. N. Waterman, 2013: Eddy-induced modulation of turbulent dissipation over rough topography in the southern ocean. *Journal of Physical Oceanography*.

Bryan, F., 1987: Parameter sensitivity of primitive equation ocean general circulation models. *Journal of Physical Oceanography*, **17 (7)**, 970–985.

Chow, C. C., D. Henderson, and H. Segur, 1996: A generalized stability criterion for resonant triad interactions. *Journal of Fluid Mechanics*, **319**, 67–76.

Ferrari, R. and C. Wunsch, 2009: Ocean circulation kinetic energy: Reservoirs, sources, and sinks. *Annual Review of Fluid Mechanics*, **41 (1)**, 253–282, doi:10.1146/annurev.fluid.40.111406.102139.

Garabato, A. C. N., K. L. Polzin, B. A. King, K. J. Heywood, and M. Visbeck, 2004: Widespread intense turbulent mixing in the southern ocean. *Science*, **303 (5655)**, 210–213.

Hasselmann, K., 1967: A criterion for nonlinear wave stability. *Journal of Fluid Mechanics*, **30 (04)**, 737–739.

Ito, T. and J. Marshall, 2008: Control of lower-limb overturning circulation in the southern ocean by diapycnal mixing and mesoscale eddy transfer. *Journal of Physical Oceanography*, **38 (12)**, 2832–2845, doi:10.1175/2008JPO3878.1.

Koudella, C. and C. Staquet, 2006: Instability mechanisms of a two-dimensional progressive internal gravity wave. *Journal of Fluid Mechanics*, **548**, 165–196.

Melet, A., R. Hallberg, S. Legg, and M. Nikurashin, 2014: Sensitivity of the ocean state to lee wave driven mixing. *Journal of Physical Oceanography*, **submitted**.

Melet, A., R. Hallberg, S. Legg, and K. Polzin, 2013: Sensitivity of the ocean state to the vertical distribution of internal-tide-driven mixing. *Journal of Physical Oceanography*, **43 (3)**, 602–615.

Nikurashin, M. and R. Ferrari, 2010a: Radiation and dissipation of internal waves generated by geostrophic motions impinging on small-scale topography: Application to the southern ocean. *Journal of Physical Oceanography*, **40 (9)**, 2025–2042, doi:10.1175/2010JPO4315.1.

Nikurashin, M. and R. Ferrari, 2010b: Radiation and dissipation of internal waves generated by geostrophic motions impinging on small-scale topography: Theory. *Journal of Physical Oceanography*, **40 (5)**, 1055–1074, doi:10.1175/2009JPO4199.1.

Nikurashin, M. and R. Ferrari, 2011: Global energy conversion rate from geostrophic flows into internal lee waves in the deep ocean. *Geophysical Research Letters*, **38 (8)**, L08 610.

503 Nikurashin, M., G. Vallis, and A. Adcroft, 2012: Routes to energy dissipation for geostrophic
504 flows in the southern ocean. *Nature Geoscience*, **6 (1)**, 48–51.

505 Osborn, T. R., 1980: Estimates of the local rate of vertical diffusion from dissipation mea-
506 surements. *Journal of Physical Oceanography*, **10 (1)**, 83–89, doi:10.1175/1520-0485(1980)
507 010⟨0083:EOTLRO⟩2.0.CO;2.

508 Phillips, O., 1967: Theoretical and experimental studies of gravity wave interactions. *Pro-*
509 *ceedings of the Royal Society of London. Series A. Mathematical and Physical Sciences*,
510 **299 (1456)**, 104–119.

511 Polzin, K. and E. Firing, 1997: Estimates of diapycnal mixing using LADCP and CTD data
512 from I8S. *Int. WOCE Newslett.*, **29**, 3942.

513 Polzin, K., A. C. Naveira H-Garabato, T. H. Huussen, and B. Sloyan, 2013: Finescale
514 parameterizations of turbulent dissipation. *Reviews of Geophysics*, **submitted**.

515 Polzin, K. L., 2009: An abyssal recipe. *Ocean Modelling*, **30 (4)**, 298–309, doi:10.1016/j.
516 ocemod.2009.07.006.

517 Saenko, O. A., X. Zhai, W. J. Merryfield, and W. G. Lee, 2012: The combined effect of
518 tidally and eddy-driven diapycnal mixing on the large-scale ocean circulation. *Journal of*
519 *Physical Oceanography*, **42 (4)**, 526–538.

520 Scott, R. B., J. A. Goff, A. C. Naveira Garabato, and A. J. G. Nurser, 2011: Global rate and
521 spectral characteristics of internal gravity wave generation by geostrophic flow over topog-
522 raphy. *Journal of Geophysical Research: Oceans*, **116 (C9)**, doi:10.1029/2011JC007005.

Sheen, K., et al., 2013: Rates and mechanisms of turbulent dissipation and mixing in the southern ocean: Results from the diapycnal and isopycnal mixing experiment in the southern ocean (dimes). *Journal of Geophysical Research: Oceans*.

Sloyan, B. M. and S. R. Rintoul, 2001: The southern ocean limb of the global deep overturning circulation. *Journal of Physical Oceanography*, **31 (1)**, 143–173, doi:10.1175/1520-0485(2001)031⟨0143:TSOLOT⟩2.0.CO;2.

St. Laurent, L. C., H. L. Simmons, and S. R. Jayne, 2002: Estimating tidally driven mixing in the deep ocean. *Geophysical Research Letters*, **29 (23)**, doi:10.1029/2002GL015633.

Stein, W. et al., 2012: *Sage Mathematics Software (Version 4.7.1)*. The Sage Development Team, `http://www.sagemath.org`.

Waterman, S., K. L. Polzin, A. C. Naveira Garabato, K. L. Sheen, and A. Forryan, 2014: Suppression of internal wave breaking in the antarctic circumpolar current near topography. *Journal of Physical Oceanography*, **44 (5)**, 1466–1492.

List of Tables

1 Summary of the simulations. L is the horizontal length of the numerical domain, h_T is the height of the topography and f is the Coriolis parameter. Either partial-slip or free-slip boundary conditions are used at the topography for the velocity field. The other physical and numerical parameters are the same for all simulations and described in Section 2. 30

TABLE 1. Summary of the simulations. L is the horizontal length of the numerical domain, h_T is the height of the topography and f is the Coriolis parameter. Either partial-slip or free-slip boundary conditions are used at the topography for the velocity field. The other physical and numerical parameters are the same for all simulations and described in Section 2.

$Name$	L	h_T	f	Bottom condition
$H_{20}L_2$	$2km$	20 m	1.10^{-4} s^{-1}	Partial-slip
$H_{40}L_2$	$2km$	40 m	1.10^{-4} s^{-1}	Partial-slip
$H_{80}L_2$	$2km$	80 m	1.10^{-4} s^{-1}	Partial-slip
$H_{20}L_2\_fs$	$2km$	20 m	1.10^{-4} s^{-1}	Free-slip
$H_{40}L_2\_fs$	$2km$	40 m	1.10^{-4} s^{-1}	Free-slip
$H_{80}L_2\_fs$	$2km$	80 m	1.10^{-4} s^{-1}	Free-slip
$H_{20}L_{1.2}$	$1.2km$	20 m	1.10^{-4} s^{-1}	Partial-slip
$H_{40}L_{1.2}$	$1.2km$	40 m	1.10^{-4} s^{-1}	Partial-slip
$H_{80}L_{1.2}$	$1.2km$	80 m	1.10^{-4} s^{-1}	Partial-slip
$H_{40}L_2\_2f$	$2km$	40 m	2.10^{-4} s^{-1}	Partial-slip
$H_{80}L_2\_2f$	$2km$	80 m	2.10^{-4} s^{-1}	Partial-slip

List of Figures

1 Numerical setting. A uniform geostrophic current U_G flows over a sinusoidal topography (k_T,h_T) in a two-dimensional domain with horizontal periodic boundary conditions. Internal lee waves are emitted, as sketched by dashed phase lines, which are damped in a sponge layer of thickness 5000 m starting at 2000 m above topography. 34

2 Snapshots of the vertical velocity for experiment $H_{40}L_2$ after one inertial period (top) and after 7 inertial periods (bottom). The same colorbar is used for the two panels, but the maximum value is about three times higher in the bottom than in the top panel. Note the quasi-linear regime in the top panel and the strongly nonlinear regime in the bottom one. 35

3 Vertical structure of (top) the IO amplitude and (bottom) the TKE dissipation rate, averaged from 12 to 15 inertial periods. The latter quantity is computed by interpolating the $\sigma-$coordinate velocity field to $z-$coordinates before performing a horizontal average. For clarity, only the $L_{2\_}fs$ simulations are shown. Note the logarithmic scale on the x-axis. 36

558 4 Variance preserving power spectrum of w for experiment $H_{20}L_2$, near 600
559 m above the topography, computed in a frame of reference moving with the
560 geostrophic velocity U_G. The straight line is the confidence level at 99% im-
561 plying that the spectrum significantly departs from red noise when it exceeds
562 this line. The inertial and buoyancy frequencies and the frequencies predicted
563 by the resonant interaction theory are indicated with a vertical dashed-dotted
564 line. 37

565 5 Temporal evolution of the IOs at 100 m above topography in log-lin coordi-
566 nates for simulations described in Table 1. For clarity, the $H_{20}L_2$, $H_{40}L_2$ and
567 $H_{80}L_2$ curves are shifted down by one decade along the vertical whereas the
568 $H_{20}L_{1.2}$, $H_{40}L_{1.2}$ and $H_{80}L_{1.2}$ curves are shifted down by two decades. This
569 permits to display the value of the growth rate predicted by the resonant
570 interaction theory (Eq. (12)) for each simulation (continuous line). The IO
571 signal was processed through a Lanczos low-pass filter at cutoff frequency f. 38

572 6 Time-height diagram of the horizontal velocity of the inertial oscillations for
573 $H_{20}L_{2\_}fs$. The slope of the black line has the value of the vertical phase speed
574 of the IOs, f/m_{IO}, with m_{IO} derived from the resonant interaction theory for
575 the triad involving a $*$ wave of frequency $U_G k_t - |f|$ (and $m_{IO} > 0$). 39

7 (top) Temporal evolution of (top) the IO amplitude at 100 m above topography and (bottom) of the TKE dissipation rate integrated over the bottom 2000 m. The spin-up of the simulations, during which the mean flow grows from 0 to U_G and IOs are explicitely damped, is not shown in the top panel. Note that the data displayed in the top frame are the same as those displayed in Fig. 5. 40

8 Scatter plot of the IO kinetic energy versus the TKE dissipation integrated over the domain and from 12 to 15 inertial periods. TKE dissipation is non dimensionalized by the bottom energy conversion rate. IO kinetic energy is non dimensionalized by the bottom conversion rate divided by an inertial period. Simulations leading to the prediction of a growth rate corresponding to a time smaller than 3 inertial periods are indicated with a filled marker (black or grey). For simulations with empty markers, this time is larger than 10 inertial periods. The + and × signs refer to simulations with $\Gamma^2 < 0$. 41

9 Vertical structure of (top) the IO amplitude and (bottom) the horizontally-averaged TKE dissipation rate. For all the simulations, the fields are averaged from 12 to 15 inertial periods. 42

10 Example of the analytical (dotted line) to simulated (full line) profile comparison for simulation $H_{40}L_2$ for (top) the IOs and (bottom) the TKE dissipation rate. The simulated profiles are averaged from 12 to 15 inertial periods. 43

11 Scatter diagram of the typical height of the IOs versus the typical height of the TKE dissipation. The meaning of the markers and signs is as in Fig. 8. 44

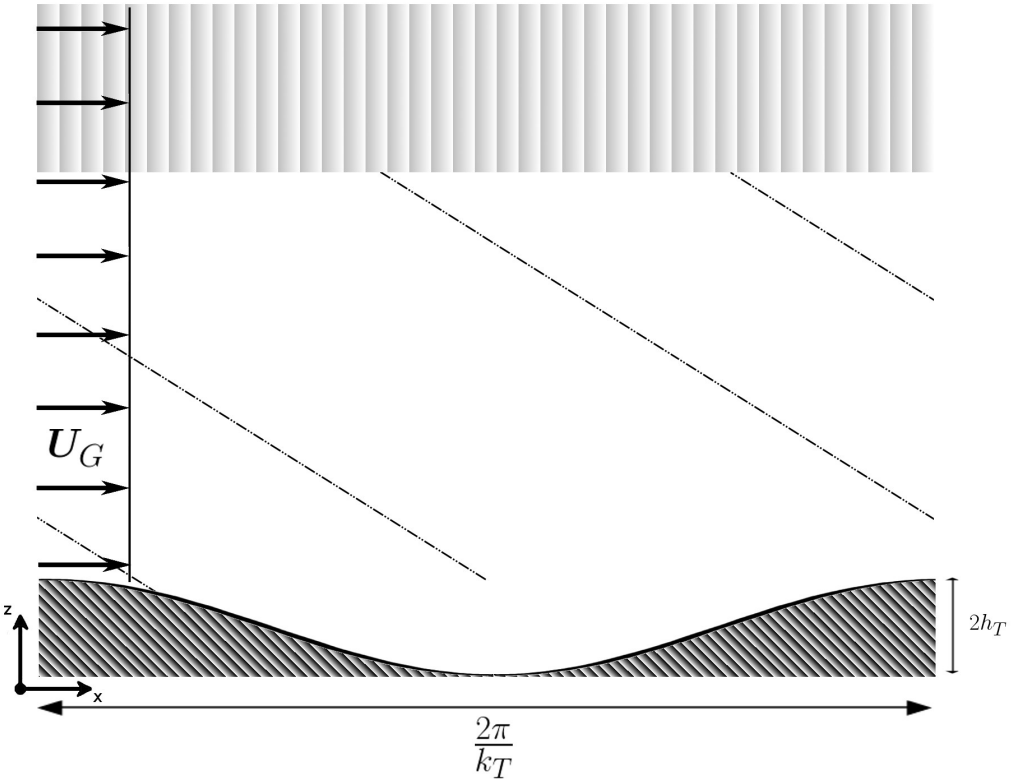

FIG. 1. Numerical setting. A uniform geostrophic current U_G flows over a sinusoidal topography (k_T,h_T) in a two-dimensional domain with horizontal periodic boundary conditions. Internal lee waves are emitted, as sketched by dashed phase lines, which are damped in a sponge layer of thickness 5000 m starting at 2000 m above topography.

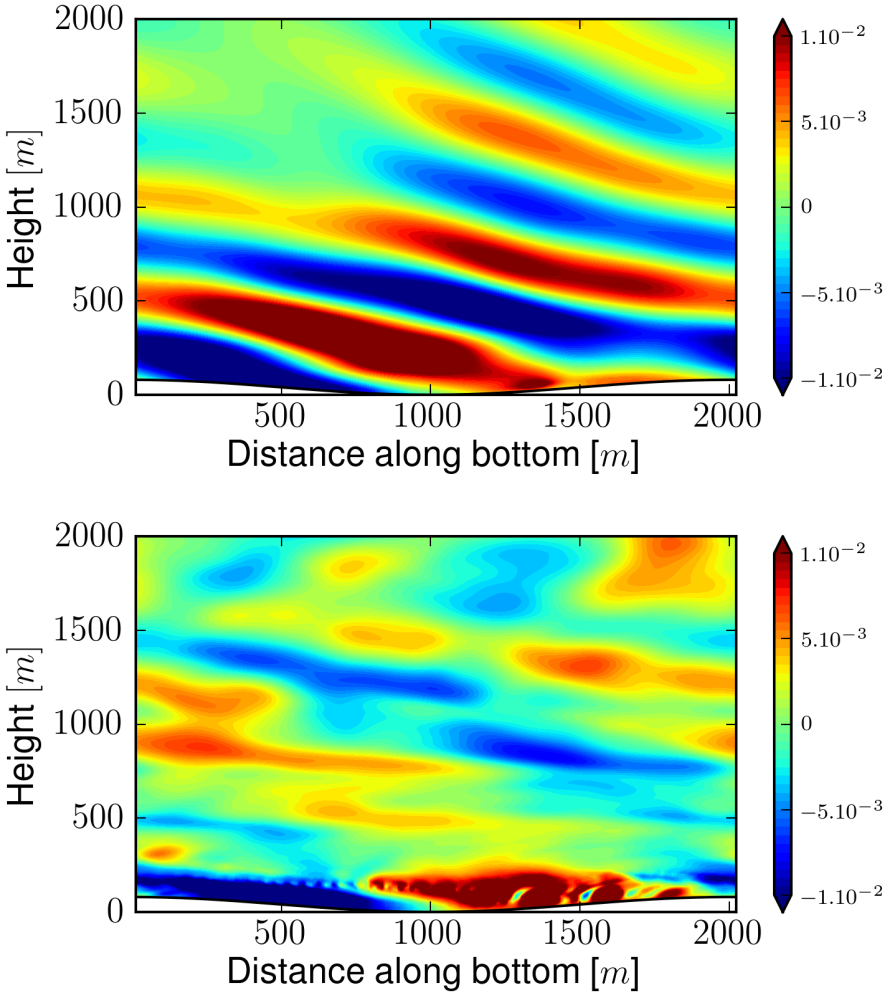

FIG. 2. Snapshots of the vertical velocity for experiment $H_{40}L_2$ after one inertial period (top) and after 7 inertial periods (bottom). The same colorbar is used for the two panels, but the maximum value is about three times higher in the bottom than in the top panel. Note the quasi-linear regime in the top panel and the strongly nonlinear regime in the bottom one.

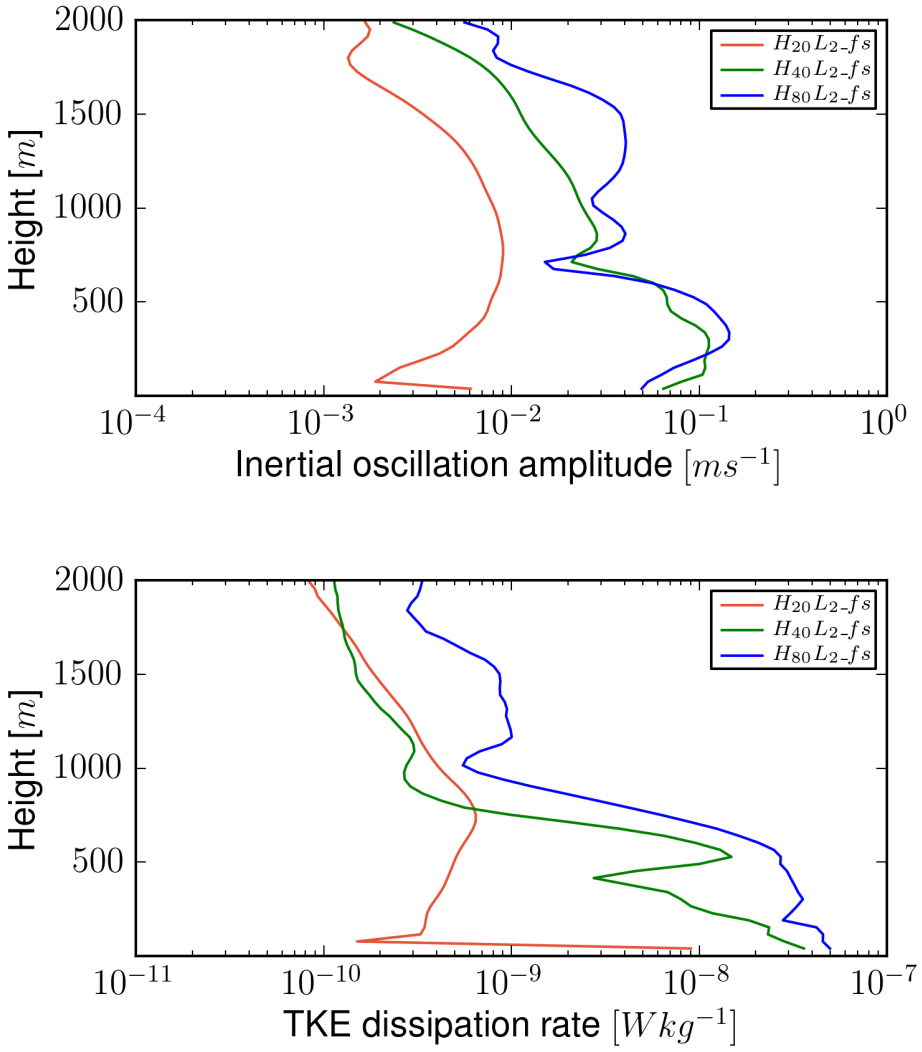

FIG. 3. Vertical structure of (top) the IO amplitude and (bottom) the TKE dissipation rate, averaged from 12 to 15 inertial periods. The latter quantity is computed by interpolating the $\sigma-$coordinate velocity field to $z-$coordinates before performing a horizontal average. For clarity, only the L_2_fs simulations are shown. Note the logarithmic scale on the x-axis.

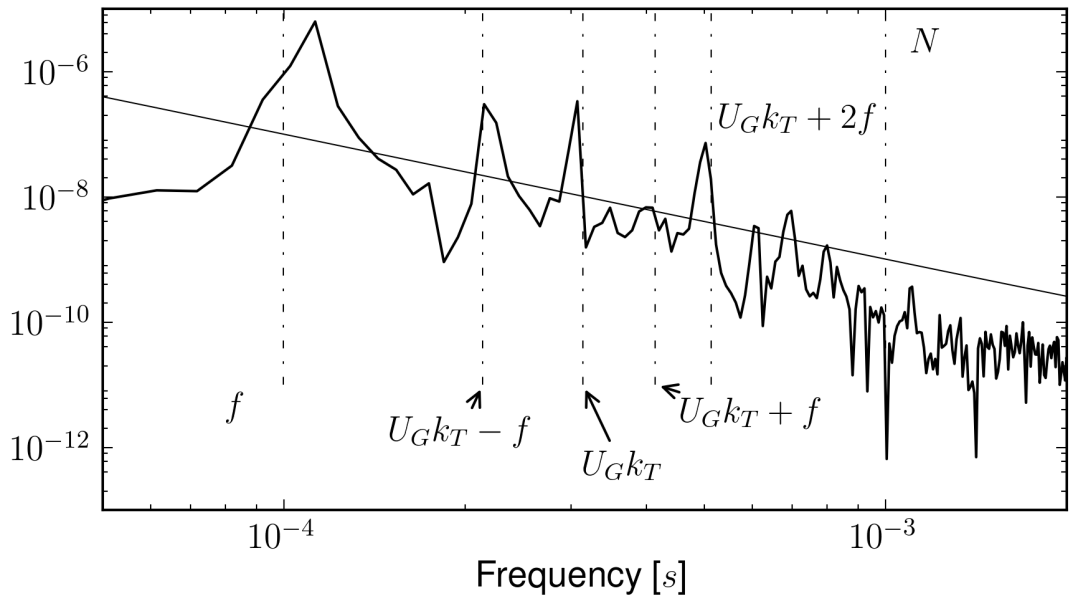

FIG. 4. Variance preserving power spectrum of w for experiment $H_{20}L_2$, near 600 m above the topography, computed in a frame of reference moving with the geostrophic velocity U_G. The straight line is the confidence level at 99% implying that the spectrum significantly departs from red noise when it exceeds this line. The inertial and buoyancy frequencies and the frequencies predicted by the resonant interaction theory are indicated with a vertical dashed-dotted line.

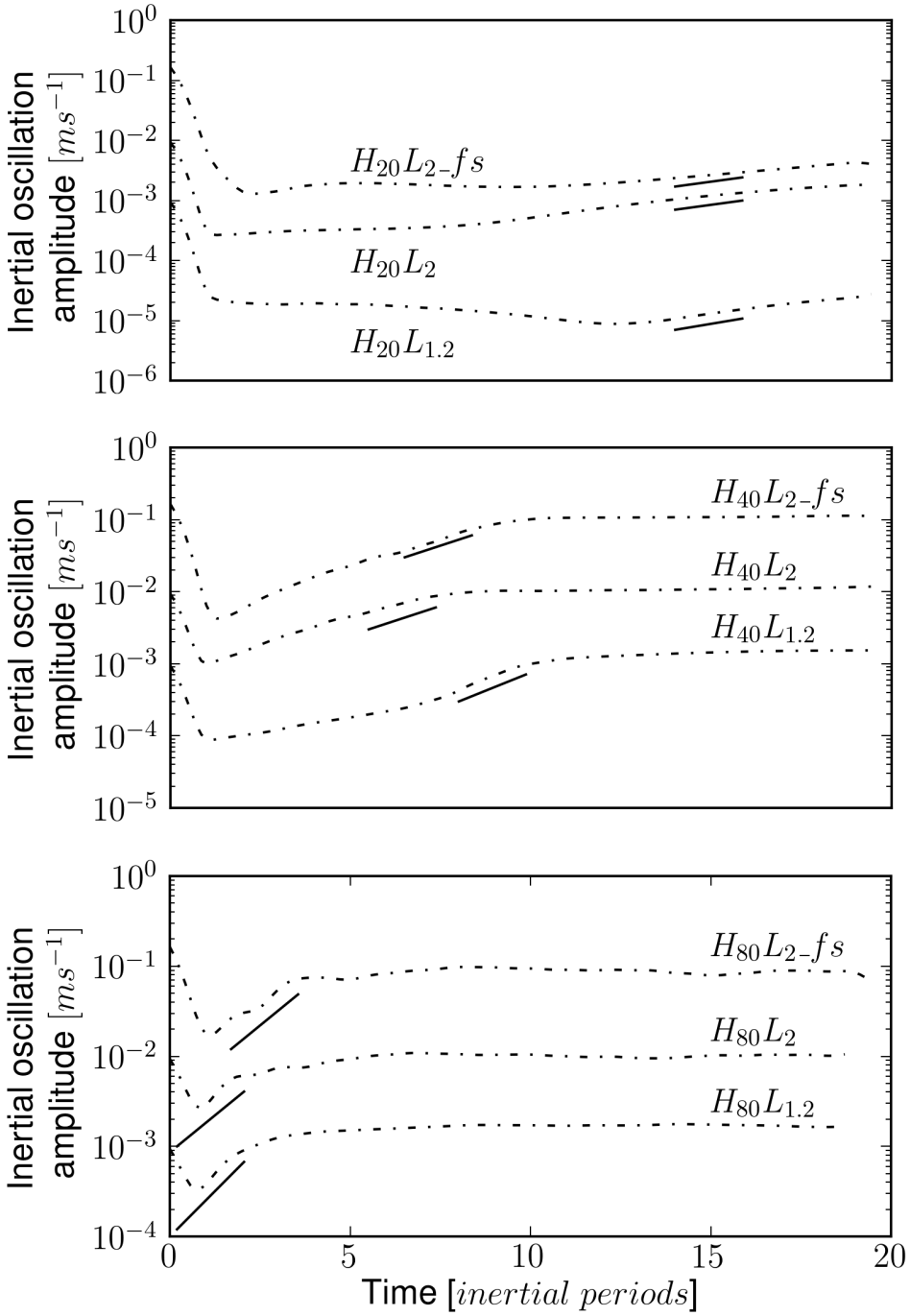

FIG. 5. Temporal evolution of the IOs at 100 m above topography in log-lin coordinates for simulations described in Table 1. For clarity, the $H_{20}L_2$, $H_{40}L_2$ and $H_{80}L_2$ curves are shifted down by one decade along the vertical whereas the $H_{20}L_{1.2}$, $H_{40}L_{1.2}$ and $H_{80}L_{1.2}$ curves are shifted down by two decades. This permits to display the value of the growth rate predicted by the resonant interaction theory (Eq. (12)) for each simulation (continuous line). The IO signal was processed through a Lanczos low-pass filter at cutoff frequency f.

Ondes de relief dans l'océan profond:
mélange diapycnal et interactions avec les oscillations inertielles.

L'Océan Austral est une zone clef pour la circulation océanique tant à cause de l'intensité du courant circumpolaire antarctique qu'en tant que région de formation des masses d'eaux abyssales de l'océan global. Pour modéliser l'océan et prévoir les changements climatiques futurs, il est important de comprendre les processus de mélange diapycnal qui lient ces eaux abyssales aux couches supérieures.
Dans l'Océan Austral, des courants profonds et intenses s'écoulent sur une topographie accidentée, ce qui génère des ondes internes de relief très énergétiques. Actuellement, la dissipation de l'énergie induite par ces ondes de relief est la candidate principale pour expliquer les forts taux de mélange observés à ces latitudes. L'objet du présent travail de thèse est de comprendre comment les ondes internes de relief sont dissipées et affectent la circulation et le mélange diapycnal dans l'océan abyssal.
Nous examinons l'impact de ces ondes sur le mélange profond au moyen d'une combinaison d'expertise de terrain, de simulations non hydrostatiques bi-dimensionnelles et de calculs théoriques. Sur la gamme de paramètres étudiés, nous montrons, en présence des ondes de relief, une intensification du taux de dissipation d'énergie cinétique turbulente sur une profondeur de 1000 m au-dessus de la topographie, atteignant typiquement $\sim$ 20 mW.m^{-2}.
Nous montrons également comment les ondes participent à des intéractions triadiques impliquant des oscillations inertielles qui sont amplifiées par interactions résonantes contrôlées par les ondes de relief. Finalement, nous préparons de futures études tri-dimensionnelles en concevant un cadre numérique et en décrivant des outils théoriques adaptés à ce problème. Nos résultats préliminaires en trois dimensions montrent qui le confinement méridien de la topographie réduit significativement l'émission d'ondes internes de relief.

Mots-clefs *Océanographie, ondes internes de relief, mélange diapycnal, dissipation d'énergie cinétique turbulente, interactions onde-onde, interactions onde-courant moyen*

Internal lee waves in the abyssal ocean:
diapycnal mixing and interactions with inertial oscillations.

The Southern Ocean plays a key role in global ocean circulation by connecting the major ocean basins with the intense Antarctic Circumpolar Current and as a formation region for abyssal water masses of the global ocean. Understanding the diapycnal mixing processes that link these abyssal waters to the overlying layers is essential both for ocean modelling and for predicting future climate change.
In the Southern Ocean, deep reaching currents impinge on rough topography and create highly energetic internal lee waves. The dissipation of the energy of these internal lee waves is the main candidate for explaining the high mixing rates between waters of different densities observed at these latitudes. The purpose of this study is to understand the fate of the internal lee wave energy and how it affects the circulation and diapycnal mixing in the abyssal ocean.
We first study the impact of internal lee waves on deep mixing with the combination of field expertise, two-dimensional non hydrostatic numerical simulations and theoretical developments. Over the range of parameters studied, an enhanced bottom turbulent kinetic energy dissipation is observed in the bottom 1000 m, typically reaching $\sim$ 20 mW.m^{-2}. We further show that internal lee waves undergo non-dissipative wave-wave interactions that can be rationalized as resonant triad interactions between the bottom emitted internal lee waves, inertial oscillations and linear combinations of these two waves.
We then build a three-dimensional model configuration and specific diagnostic methods that pave the way for future investigations in three dimensions. Preliminary results with the three-dimensional numerical configuration show that the meridional confinement of the topography notably reduces the emission of internal lee waves.

Keywords *Oceanography, internal lee waves, diapycnal mixing, dissipation of turbulent kinetic energy, wave-wave interactions, wave-mean flow interactions*